

University of New Mexico

UNM Digital Repository

Physics & Astronomy ETDs

Electronic Theses and Dissertations


Spring 5-10-2019

Topics in Three-Dimensional Imaging, Source Localization and Super-resolution

Zhixian Yu

University of New Mexico

Follow this and additional works at: https://digitalrepository.unm.edu/phyc_etds

 Part of the [Atomic, Molecular and Optical Physics Commons](#), [Biological and Chemical Physics Commons](#), [Optics Commons](#), and the [Quantum Physics Commons](#)

Recommended Citation

Yu, Zhixian. "Topics in Three-Dimensional Imaging, Source Localization and Super-resolution." (2019). https://digitalrepository.unm.edu/phyc_etds/217

This Dissertation is brought to you for free and open access by the Electronic Theses and Dissertations at UNM Digital Repository. It has been accepted for inclusion in Physics & Astronomy ETDs by an authorized administrator of UNM Digital Repository. For more information, please contact amywinter@unm.edu.

Topics in Three-Dimensional Imaging, Source Localization and Super-resolution

by

Zhixian Yu

B.S., Physics, Qingdao University, 2007

M.S., Physics, Qingdao University, 2010

DISSERTATION

Submitted in Partial Fulfillment of the
Requirements for the Degree of

Doctor of Philosophy
Physics

The University of New Mexico

Albuquerque, New Mexico

July, 2019

©2019, Zhixian Yu

Dedication

To my parents, Xiaohe Yu and Binhua Wu, grandparents, Prof. Liang Yu and Aima Yu, and aunts Xiaoyi Yu and Dr. Xiaolin Yu

Acknowledgments

I would like to thank my advisor, Prof. Sudhakar Prasad, a brilliant physicist and gifted mentor, for his guidance, inspiration and support.

Many thanks also to the other members of my dissertation committee, Prof. Keith Lidke, Prof. Arash Mafi and Prof. John Grey for their insightful comments and encouragements.

Topics in Three-Dimensional Imaging, Source Localization and Super-resolution

by

Zhixian Yu

B.S., Physics, Qingdao University, 2007

M.S., Physics, Qingdao University, 2010

Ph.D., Physics, University of New Mexico, 2019

Abstract

The realization that twisted light beams with helical phasefronts could carry orbital angular momentum (OAM) that is in excess of the photon's spin angular momentum (SAM) has spawned various important applications. One example is the design of novel imaging systems that achieve three-dimensional (3D) imaging in a single snapshot via the rotation of point spread function (PSF).

Based on a scalar-field analysis, a particular simple version of rotating PSF imagery, which was proposed by my advisor Dr. Prasad, furnishes a practical approach to perform 3D source localization using a spiral phase mask that generates a combination of Bessel vortex beams. For a special annular design of the mask, with the spiral-phase winding number in successive annuli changing by a fixed quantum number, this Bessel-beam combination can yield a shape and size invariant PSF that rotates as a function of the axial position of the source, and possesses a superior depth of field (DOF) when compared to other rotating PSFs.

In the first part of this dissertation, we present a vector-field analysis of an improved rotating PSF design that encodes both the 3D location and polarization state of a monochromatic point dipole emitter for high numerical aperture (NA) microscopy, in which non-paraxial propagation of the imaging beam and the associated vector character of light fields are properly accounted for. By examining the angle of rotation and the spatial form of the PSF, one can simultaneously localize point sources and determine the polarization state of light emitted by them over a 3D field in a single snapshot. We also propose a more advanced approach for doing joint polarimetry and 3D localization using a SAM-OAM conversion device without the need for high NA is also proposed.

A recent paradigm-shifting research proposal has focused on employing the toolbox of quantum parameter estimation for the problem of super-resolution of two incoherent point sources. Surprisingly, the quantum Fisher information (QFI) and associated quantum Cramér-Rao bound (QCRB) for estimating the one-dimensional transverse separation of the source pair are both finite constants that are achievable with purely classical measurements that utilize coherent projections of the optical wavefront.

A second important contribution of this dissertation is the generalization of the previous quantum limited transverse super-resolution work to full 3D imaging with more general PSF. Under the assumption of known centroid, we first derive the general expression of 3×3 QFI matrix with respect to (w.r.t.) the 3D pair separation vector, in terms of the correlation of the wavefront phase gradients in the imaging aperture. For a clear circular aperture, the QFI matrix turns out to be a separation-independent diagonal matrix. Coherent-projection bases that can attain the corresponding QCRB in special cases and small separation limits are also proposed with confirmation by numerical simulations.

We next extend our 3D analysis to treat the more general 6-parameter problem

of jointly estimating the 3D pair-centroid location and pair-separation vectors. We also present the results of computer simulation of an experimental protocol based on the use of Zernike-mode projections to attain these quantum estimation-limited bounds of performance.

Contents

List of Figures	xiii
Glossary	xviii
1 Introduction	1
1.1 Twisted Light and Its Applications	1
1.2 Quantum Limited Super-resolution	2
1.3 Dissertation Overview	4
References	6
2 3D Polarimetric Imaging with High Numerical Aperture Rotating PSF	11
2.1 Introduction	11
2.2 Rotating PSFs with Gauss-Laguerre Modes	12
2.2.1 Double-Helix PSF	12
2.2.2 Corkscrew PSF	15

Contents

2.3	Prasad's Original Rotating PSF	15
2.4	High NA Rotating PSF	20
2.4.1	Introduction	20
2.4.2	Radiation Field from a Point Dipole Emitter	21
2.4.3	Action of the Focusing, Polarizing, and Spiral Phase Elements	21
2.4.4	Propagation to the Image Plane	26
2.4.5	Generalized Spiral Phase Profile	28
2.4.6	Polarization Dependent Rotating PSF	29
2.4.7	Simultaneous Reconstruction of Dipole Orientation and Position from Rotating PSF	40
2.5	Conclusions	42
	References	47
3	3D Polarimetric Imaging via SAM-OAM Conversion	51
3.1	Introduction	51
3.2	The Basic Concept of q-plate Technology	52
3.3	Improved 3D Polarimetric Imaging via SAM-OAM Conversion	54
3.4	Conclusions	60
	References	62
4	Achieving Quantum Limited 3D Super-resolution	64

Contents

4.1	Introduction	64
4.2	QFI Matrix for 3D Pair Separation	67
4.3	Achieving QFI in Two Special Cases	74
4.4	Achieving QFI in the Limit of Small Separations	77
4.5	Maximum-Likelihood Estimation of Pair Separation	80
4.6	Conclusions	84
	References	85
5	Quantum Limited 3D pair Super-localization and Super-resolution	90
5.1	Introduction	90
5.2	QFI for Jointly Estimating the Centroid and the Separation of a Pair of Incoherent Point Sources with Equal Brightness	91
5.2.1	Vanishing of the Off-diagonal QFI Block, $\mathbf{H}^{(sl)}$	95
5.2.2	Pair-centroid-localization QFI	97
5.3	Numerical Evaluation of Pair-Centroid QCRB	100
5.4	Maximum-Likelihood Estimation of Pair Separation in the Presence of Centroid-Localization Error	104
5.5	Conclusions	106
	References	108
6	Work in Progress, Conclusions and Future Directions	110

Contents

6.1	Work in Progress	110
6.1.1	Towards More Realistic Quantum Limited 3D Super-localization and Super-resolution: the Unequal Brightness Problem	110
6.2	Conclusions and Future Directions	114
	References	115
	A Vector Diffraction Formula for Large Apertures and Propagation Distances	116
	References	119
	B Flux Conservation	120
	References	124
	C Detailed Expression for $\hat{z} \times \vec{E}_I(\vec{r}_I)$	125
	References	127
	D Derivation of QFI	128
	References	131
	E Some Properties of Sine and Cosine States	132
E.0.1	Orthonormality and Completeness	132
E.0.2	The Overlap Integrals $\langle A_{mn} K_{\pm} \rangle$, $A = CC, CS, SC, SS$	133

Contents

References	135
F Likelihood Function for Photon Division into N Channels	136
References	139
G Photon wavefunction in the pupil plane	140
References	143
H CFI for Multinomial Distribution	144
References	146

List of Figures

2.1	Examples of GL modes: (a) intensity, (b) phase. Image taken from Ref. [2].	13
2.2	The Gauss-Laguerre modal plane. Image taken from Ref. [2].	14
2.3	GL modal composition (m, n) of the corkscrew PSF in normalized units. Inset shows the corkscrew PSF phase mask in radians. Image taken from Ref. [5].	16
2.4	Schematic diagram of a specific Fresnel zone with its spiral phase retardation	16
2.5	Incoherent PPE-PSF with $L = 7$ (top row) and $L = 9$ (middle row). The IDL-PSF, is shown for comparison in the bottom row. The plots from left to right are for increasing values of defocus, from -24 radians to +24 radians of defocus in steps of 8 radians, at the edge of the pupil.	19
2.6	Transformation of an incident wavefront Σ_O into the outgoing (imaging) wavefront Σ_I , with the pupil shown by a dashed vertical line. The two linear s and p polarizations for a typical ray crossing the two wavefronts are also shown. A polarization analyzer, denoted by J , is inserted in the beam path following the focusing lens.	23

List of Figures

2.7	Ratio of $P(0, 0, 1)$ to $P(1, 0, 0)$ vs NA.	32
2.8	The PSF signal, for low NA of value 0.2, for XP (top left); YP (top right); LCP (bottom left) ; and ZP (bottom right) state of emission for the point dipole emitter located in the plane of Gaussian focus, for a seven-zone phase mask, $L = 7$, with $a = 1$, $b = 0$. The full array size in each panel is 16×16 in units of squared Airy disk radius (see text). The color coding in each PSF, with yellow representing its brightest pixel and blue its faintest, is only for the ease of visualization of its spatial structure. The brightest pixel of the PSF in the bottom right plot is, in fact, over 100 times fainter than those for the other three plots, which agrees well with Fig. 2.7. Image taken from Ref. [29]. . .	33
2.9	Same as Fig. 2.8, except for high NA of value 0.9. The XP, YP, and LCP emission states have PSFs with comparable brightest pixels, within 10% of one another, but which are a factor of 2 brighter than for the ZP emission state. This phenomenon also agrees well with the growing ratio plotted in Fig. 2.7. Image taken from Ref. [29]. . .	35
2.10	The rotating PSF signals on the sensor array for the XP (1st row); YP (2nd row); and ZP (3rd row) states of emission for the point dipole for the low-NA case, namely for NA=0.2. The figures in each row from left to right display the PSFs corresponding to the values -162π , 0, and $+162\pi$ radians for the defocus parameter, $k\delta z_O$, or equivalently δz_O being -3.25, 0, and +3.25 units of the wave depth of field, λ/NA^2 , of the microscope. Image taken from Ref. [29]. . . .	36
2.11	Same as Fig. 2.10, except NA is chosen to be higher at 0.9, but δz_O taking the same three values in units of λ/NA^2 as in Fig. 2.10. Image taken from Ref. [29].	37

List of Figures

2.12	The MTF signals corresponding to the PSFs in Fig. 2.10. For the chosen parameter values, the array in each panel is the minimal square circumscribing the disk of diffraction limited bandwidth of the imager. Image taken from Ref. [29].	38
2.13	Same as Fig. 2.12, except for high NA of value 0.9. Image taken from Ref. [29].	39
2.14	Standard deviation of the estimated n_x and n_y vs average total photon number for XZP state of the dipole source fixed at the center of the object plane and δz_O changed from -4λ (1st column) to 0 (2nd column) to 4λ (3rd column). The value of NA was chosen to be 0.9 here corresponding to $R/z_O = 2.06$ with $n_O = 1$	43
2.15	Standard deviation of the estimated δx_O , δy_O and δz_O (top to bottom) vs average total photon number for (left to right) $\delta z_O = -4\lambda$, 0, and $+4\lambda$ for the x polarized state of emission, with $\lambda = 550\text{ nm}$ and NA=0.9.	44
2.16	Same as Fig. 2.15 except for the y polarized state of dipole emission.	45
2.17	Same as Fig. 2.15 except for the z polarized state of dipole emission.	46
3.1	Examples of q-plates. The tangent to the lines shown indicate the local direction of the optical axis. (a) $q = 1/2$, $\alpha_0 = 0$; (b) $q = 1$, $\alpha_0 = 0$; (c) $q = 1$, $\alpha_0 = \pi/2$. Image taken from Ref. [8].	54
3.2	The total PSF signal (1st column), PSF signal in x polarization channel (2nd column) and y polarization channel (3rd column) for the point dipole emitter located in the plane of Gaussian focus in XLP, YLP, 45LP, 135LP, LCP and RCP states (from top to bottom). . . .	57

List of Figures

3.3	The total rotating PSF signals for emission of the point dipole with $s_3 = 0$ (1st row); $s_3 = 1$ (2nd row); and $s_3 = -1$ (3rd row). s_0 is fixed to be 1. The figures in each row from left to right display the PSFs corresponding to the values $-4m$, 0 , and $4m$ for δz_O . We choose $\lambda = 1\mu m$, $R=0.5$ m, $z_O = 1000m$	58
3.4	The square root of the average variance of the reconstructed Stokes parameters vs average total photon number for dipole at $\delta z_O = 0$ emitting in XLP, YLP, 45LP, 135LP, LCP, RCP, UP and PP (1, 0.5, 0.4, 0.3) states.	59
3.5	Standard deviation of the estimated δx_O , δy_O and δz_O (top to bottom) vs average total photon number for (left to right) $\delta z_O = -4m$, 0 , and $+4m$ for the x polarized state of emission, with $\lambda = 1\mu m$, $R = 0.5m$, $z_O = 1000m$	61
4.1	Plots of QFI (dashed line) and CFI w.r.t. $l_{x(y)}$ for $l_{y(x)} = 0.025$ (lower curve) and $l_{y(x)} = 0.25$ (upper curve) and for $l_z = 0.025$ (left panels) and $l_z = 0.25$ (right panels).	78
4.2	Plots of QFI (dash line) and CFI w.r.t. l_z , for four different values of l_\perp , namely 0.025, 0.05, 0.125, and 0.25.	79
4.3	Plots of CRBs w.r.t. $l_{x(y)}$ for $l_{y(x)} = 0.025$ (lower curve) and $l_{y(x)} = 0.25$ (upper curve) and for $l_z = 0.025$ (left panels) and $l_z = 0.25$ (right panels). Variances obtained from ML estimation are shown by different marker symbols. Image taken from Ref. [48].	82
4.4	Plots of CRB w.r.t. l_z , for four different values of l_\perp , namely 0.025, 0.05, 0.125, and 0.25. Variances obtained from ML estimation are shown by different marker symbols. Image taken from Ref. [48]. . .	83

List of Figures

5.1	Plots of QCRB for s_x vs. l_x for various values of l_y and for two different values of l_z , namely 0.025 (left panel) and 0.25 (right panel). Image taken from Ref. [4].	101
5.2	Plots of QCRB for s_x vs. l_y for two different values of l_z , namely 0.025 (left panel) and 0.25 (right panel). Image taken from Ref. [4].	102
5.3	Plots of QCRB for s_z vs. l_z for five different values of l_\perp . Image taken from Ref. [4].	103
5.4	(a) Plot of variance of estimation of l_x with changing values of l_x (shown by marker symbols), with the other two l coordinates being equal to 0.025, for $\sigma_{s_x} = \sigma_{s_y} = 0.005$; $\sigma_{s_z} = 0.01$; (b) Same as (a) except $l_x \rightarrow l_z$. Plots of CRBs w.r.t. $l_{x(z)}$ are also shown for comparison. Image taken from Ref. [4].	105

Glossary

SAM	spin angular momentum
OAM	orbital angular momentum
3D	three-dimensional
PSF	point spread function
DOF	depth of field
NA	numerical aperture
FI	Fisher information
CFI	classical Fisher information
QFI	quantum Fisher information
CRB	Cramér-Rao bound
CCRB	classical Cramér-Rao bound
QCRB	quantum Cramér-Rao bound
PPE	pupil-phase-engineered
MTF	modulation transfer function

Glossary

GL	Gauss-Laguerre
DH	Double-Helix
SLD	Symmetric Logarithmic Derivative
ML	maximum-likelihood

Chapter 1

Introduction

1.1 Twisted Light and Its Applications

In 1909, by drawing an analogy between light and mechanical systems, Poynting [1] deduced that circularly polarized light carries an angular momentum. We now see his deduction as being compatible with our understanding of the $\pm\hbar$ spin angular momentum (SAM) states of the photon. A SAM of $\pm\hbar$ per photon is consistent with the description of the absorption and emission of light from dipole transitions within atomic systems, where the angular momentum is conserved between the electronic state and the interacting optical field [2].

In 1932, Darwin [3] recognized that more complicated transitions required an angular momentum exchange between light and atom corresponding to integer multiples of \hbar . This additional angular momentum can be thought to arise from the effect of light's linear momentum acting off-axis with respect to the center of the optical beam or center of mass of the interacting object. For many decades this orbital angular momentum had been associated only with higher-order atomic or molecular transitions and hence considered to be a rare occurrence.

Chapter 1. Introduction

In 1992 Allen, Beijersbergen, Spreeuw, and Woerdman [4] realized that light beams with helical wavefronts carry orbital angular momentum (OAM) in addition to the SAM, the latter being responsible for the vector character of the associated electromagnetic fields. They showed that beams with a transverse phase structure of $\exp(-il\phi)$ carry an OAM of $l\hbar$ per photon, an angular momentum that can be arbitrarily many times greater than the spin of the photon. An important feature of beams with helical phase structure is that the beam axis marks a singularity in the optical phase. This phase singularity is manifested as a perfect zero in the optical intensity, meaning that OAM-carrying beams typically have annular intensity cross-sections.

The discovery of OAM in excess of SAM has led both to new understandings of optical effects and a number of exciting applications. These applications range from optical manipulation [5], optical communication [6]-[9], astronomy [10, 11], quantum optics [12]-[17] and nano optics [18]-[22], to the design of novel 3D imaging system [23]-[27]. It is the last application that is our main concern in the first part of this dissertation.

1.2 Quantum Limited Super-resolution

Light is an electromagnetic wave with both an amplitude and a phase. Standard imaging systems use lenses to refocus this wave and project an image of the source onto a screen, where the intensity is recorded at each position, but information about the wavefront is typically discarded. When light passes through finite-sized optical elements, diffraction smears out the spatial distribution of light with an accompanying decrease of local intensities, so that point-sources map onto finite-sized spots at the image-plane. Rayleigh's criterion [28] for resolving two incoherent point sources, which asserts that a minimum separation between the sources equal to the diffraction-

Chapter 1. Introduction

limited spot size is necessary for them to be resolvable, has been the most influential resolution criterion in the history of optics [29]. Based on the limited technology in Lord Rayleigh's era, his criterion, largely a visually-based one, neglects the possibility of better resolution using light of greater intensity or using a longer observation period. One typical workaround to diffraction limits has been to reduce the wavelength or to build higher numerical aperture optics, thereby making the PSF sharper while also capturing more of the source emission. In recent years, techniques have been developed in specific cases that address these limits in more novel ways. Despite their success, these techniques require careful control of the source of illumination [30]-[35], which is not always possible, especially in astronomical applications.

A more useful and experimentally more meaningful approach to optical resolution can be formulated in terms of the Fisher information (FI) and the associated Cramér-Rao bound (CRB) [36], which sets a limit on the precision with which the source-pair separation can be estimated. For direct imaging, as we shall review, FI drops off to 0 quadratically with decreasing pair separation. As a consequence, the variance of any biased estimator based on these intensity measurements diverges in this limit, which has been colloquially called Rayleigh's curse. Recently the problem of resolving two incoherent point sources was approached from the perspective of quantum metrology [37] and quantum estimation theory using quantum Fisher information (QFI) and the associated quantum Cramér-Rao bound (QCRB) [38, 39]. This bound provides a ultimate limit to the accuracy of estimating the source separation optimized over all possible measurement techniques allowed by quantum mechanics. Surprisingly, the QCRB for estimating the separation of two incoherent point sources is independent of that separation [40]. Even more surprisingly, the quantum limit has been shown to be achievable with classical phase-sensitive measurements [40]-[44].

1.3 Dissertation Overview

The first main topic of this dissertation is 3D polarimetric imaging with rotating PSF. In Chapter 2, we first review the theory of the rotating PSF concept invented by my advisor Dr. Prasad [23], then generalize the theoretical model of the rotating PSF imaging based 3D localization of point sources to high numerical aperture (NA) microscopy for which the non-paraxial propagation of the imaging beam and the associated vector character of light fields must be properly accounted for. Our analysis supports the prospects of simultaneous acquisition of the state of polarization and 3D location of a point source with high NA objectives. The main results of chapter 2 are based on our publication [45] in the Journal of the Optical Society of America A. In Chapter 3, we discuss a SAM-OAM conversion [46] device named the q-plate [47], then propose an advanced approach for doing joint polarimetry and 3D localization of a point source using such a q-plate.

The second main topic of this dissertation concerns an application of the tools of quantum parameter estimation to 3D super-resolution and centroid super-localization of an incoherent pair of equally bright point sources. In Chapter 4 we calculate the QFI matrix for estimating the full 3D pair separation vector, extending previous work on pair separation in one and two transverse dimensions. We next show that the pair-separation QFI is, in fact, identical to the source localization QFI. We also propose general coherent-projection bases that can attain the QFI in two special cases and small separation limits. The achievability of the QFI bounds is confirmed by numerical simulations of an approximate experimental realization of such quantum limited pair super-resolution using a special basis of Zernike modes. The main results of Chapter 4 are based on our publication [48] in Physical Review Letters. In Chapter 5 we extend our analysis of Chapter 4 to the joint estimation of the 3D location of the centroid and the 3D separation of the source pair, which we may regard as being equivalent to the problem of localizing both sources simultaneously.

Chapter 1. Introduction

We will first calculate the 6×6 QFI matrix for simultaneous pair centroid-separation estimation and then discuss the fundamental, estimation-theoretic trade-offs between the two tasks, which we confirm using simulations. The main results of Chapter 5 are based on our most recent publication [49] in Physical Review A.

In Chapter 6 we describe our current work in progress on extending the analyses of Chapters 4 and 5 to an unequally bright point source pair. We also review the significant contributions of this dissertation and discuss potential future work.

References

- [1] J. H. Poynting, “The wave motion of a revolving shaft, and a suggestion as to the angular momentum in a beam of circularly polarised light,” *Proc. R. Soc. Lond. A* **82**, 560-567 (1909).
- [2] M. Padgett, “Light’s twist,” *Proc. R. Soc. A* **136**, 20140633 (2014).
- [3] C. G. Darwin, “Notes on the theory of radiation,” *Proc. R. Soc. Lond. A* **136**, 36-52 (1932).
- [4] L. Allen, M. W. Beijersbergen, R. J. C. Spreeuw, and J. P. Woerdman, “Orbital angular momentum of light and the transformation of Laguerre-Gaussian laser modes,” *Phys. Rev. A* **45**, 8185-8189 (1992).
- [5] H. He, M. E. J. Friese, N. R. Heckenberg, and H. Rubinsztein-Dunlop, “Direct observation of transfer of angular momentum to absorptive particles from a laser beam with a phase singularity,” *Phys. Rev. Lett.* **75**, 826-829 (1995).
- [6] G. Gibson, J. Courtial, M. Padgett, M. Vasnetsov, V. Pas’ko, S. Barnett, and S. Franke-Arnold, “Free-space information transfer using light beams carrying orbital angular momentum,” *Opt. Express* **12**, 5448-5456 (2004).
- [7] F. Tamburini, E. Mari, A. Sponselli, B. Thide, A. Bianchini, and F. Romanato, “Encoding many channels on the same frequency through radio vorticity: first experimental test,” *New J. Phys.* **14**, 033001 (2012).
- [8] J. Wang, J.-Y. Yang, I. M. Fazal, N. Ahmed, Y. Yan, H. Huang, Y. Ren, Y. Yue, S. Dolinar, M. Tur, and A. E. Willner, “Terabit free-space data transmission employing orbital angular momentum multiplexing,” *Nat. Photonics* **6**, 488-496 (2012).
- [9] A. E. Willner, H. Huang, Y. Yan, Y. Ren, N. Ahmed, G. Xie, C. Bao, L. Li, Y. Cao, Z. Zhao, J. Wang, M. P. J. Lavery, M. Tur, S. Ramachandran, A.

References

- F. Molisch, N. Ashrafi, and S. Ashrafi, "Optical communications using orbital angular momentum beams," *Adv. Opt. Photonics* **7**, 66 (2015).
- [10] G. A. Swartzlander, "Peering into darkness with a vortex spatial filter," *Opt. Lett.* **26**, 497-499 (2001).
- [11] G. A. Swartzlander, Jr., E. L. Ford, R. S. Abdul-Malik, L. M. Close, M. A. Peters, D. M. Palacios, and D. W. Wilson, "Astronomical demonstration of an optical vortex coronagraph," *Opt. Express* **16**, 10200-10207 (2008).
- [12] A. Mair, A. Vaziri, G. Weihs, and A. Zeilinger, "Entanglement of the orbital angular momentum states of photons," *Nature* **412**, 313-316 (2001).
- [13] J. Leach, B. Jack, J. Romero, M. Ritsch-Martel, R. W. Boyd, A. K. Jha, S. M. Barnett, S. Franke-Arnold, and M. J. Padgett, "Violation of a Bell inequality in two-dimensional orbital angular momentum state-spaces," *Opt. Express* **17**, 8287-8293 (2009).
- [14] J. Leach, B. Jack, J. Romero, A. K. Jha, A. M. Yao, S. Franke-Arnold, D. G. Ireland, R. W. Boyd, S. M. Barnett, and M. J. Padgett, "Quantum correlations in optical angle-orbital angular momentum variables," *Science* **329**, 662-665 (2010).
- [15] R. Fickler, R. Lapkiewicz, W. N. Plick, M. Krenn, C. Schaeff, S. Ramelow, and A. Zeilinger, "Quantum entanglement of high angular momenta," *Science* **338**, 640-643 (2012).
- [16] X. -L. Wang, X. -D. Cai, Z. -E. Su, M. -C. Chen, D. Wu, L. Li, N. L. Liu, C. Y. Lu, and J. W. Pan, "Quantum teleportation of multiple degrees of freedom of a single photon," *Nature* **518**, 516-519 (2015).
- [17] M. Malik, M. Erhard, M. Huber, M. Krenn, R. Fickler, and A. Zeilinger, "Multi-photon entanglement in high dimensions," *Nat. Photonics* **10**, 248-252 (2016).
- [18] M. Babiker, W. L. Power, and L. Allen, "Light-induced torque on moving atoms," *Phys. Rev. Lett.* **73**(9), 1239-1242 (1994).
- [19] N. Yu, P. Genevet, M. A. Kats, F. Aieta, J. -P. Tetienne, F. Capasso, and Z. Gaburro, "Light propagation with phase discontinuities: generalized laws of reflection and refraction," *Science* **334**, 333-337 (2011).
- [20] P. Genevet, J. Lin, M. A. Kats, and F. Capasso, "Holographic detection of the orbital angular momentum of light with plasmonic photodiodes," *Nat. Commun.* **3**, 1278 (2012).

References

- [21] Z. Yan and N. F. Scherer, “Optical vortex induced rotation of silver nanowires,” *J. Phys. Chem. Lett.* **4**, 2937-2942 (2013).
- [22] N. M. Litchinitser, “Applied physics. Structured light meets structured matter,” *Science* **337**, 1054-1055 (2012).
- [23] S. Prasad, “Rotating point spread function via pupil-phase engineering,” *Opt. Lett.* **38**, 585-587 (2013).
- [24] S. Pavani and R. Piestun, “High-efficiency rotating point spread functions,” *Opt. Express* **16**, 3484-3489 (2008).
- [25] M. Lew, S. Lee, M. Badieirostami, and W. E. Moerner, “Corkscrew point spread function for far-field three-dimensional nanoscale localization of point objects,” *Opt. Lett.* **36**, 202-204 (2011).
- [26] G. Grover, K. DeLuca, S. Quirin, J. DeLuca, and R. Piestun, “Super-resolution photon-efficient imaging by nanometric double-helix point spread function localization of emitters (SPINDLE),” *Opt. Express* **20**, 26681-26695 (2012).
- [27] A. Jesacher, M. Ritsch-Martel, and R. Piestun, “Three-dimensional information from two-dimensional scans: a scanning microscope with post acquisition refocusing capability,” *Optica* **2**, 210-214 (2015).
- [28] L. Rayleigh, “XXXI. Investigations in Optics, with Special Reference to the Spectroscope,” *Philos. Mag.* **8**, 261 (1879).
- [29] M. Born and E. Wolf, *Principles of Optics: Electromagnetic Theory of Propagation, Interference and Diffraction of Light* (Cambridge University Press, Cambridge, England, 1999).
- [30] W. E. Moerner and L. Kador, “Optical detection and spectroscopy of single molecules in a solid,” *Phys. Rev. Lett.* **62**, 2535 (1989).
- [31] S. W. Hell and J. Wichmann, “Breaking the diffraction resolution limit by stimulated emission: stimulated-emission-depletion fluorescence microscopy,” *Opt. Lett.* **19**, 780 (1994).
- [32] E. Betzig, “Proposed method for molecular optical imaging,” *Opt. Lett.* **20**, 237 (1995).
- [33] W. E. Moerner, “New Directions in Single-Molecule Imaging and Analysis,” *Proc. Natl. Acad. Sci. U.S.A.* **104**, 12596 (2007).
- [34] S. W. Hell, “Far-Field Optical Nanoscopy,” *Science* **316**, 1153 (2007).

References

- [35] E. Betzig, G.H. Patterson, R. Sougrat, O. W. Lindwasser, S. Olenych, J. S. Bonifacino, M. W. Davidson, J. Lippincott-Schwartz, and H. F. Hess, “Imaging Intracellular Fluorescent Proteins at Nanometer Resolution,” *Science* **313**, 1642 (2006).
- [36] H. Van Trees, *Detection, Estimation, and Modulation Theory, Part I* (Wiley, 1968), Chap.2.
- [37] V. Giovannetti, S. Lloyd, and L. Maccone, “Advances in Quantum Metrology,” *Nat. Photonics* **5**, 222 (2011).
- [38] C. Helstrom, *Quantum Detection and Estimation Theory* (Academic Press, 1976), vol. 123.
- [39] M. Paris, “Quantum estimation for quantum technology,” *Int. J. Quant. Inform.* **7**, 125-137 (2009).
- [40] M. Tsang, R. Nair, and X.-M. Lu, “Quantum Theory of Superresolution for Two Incoherent Optical Point Sources,” *Phys. Rev. X* **6**, 031033 (2016).
- [41] M. Paur, B. Stoklasa, Z. Hradil, L. Sanchez-Soto, and J. Rehacek, “Achieving the ultimate optical resolution,” *Optica* **10**, 1144-1147 (2016).
- [42] Z.S. Tang, K. Durak, and A. Ling, “Fault-tolerant and finite-error localization for point emitters within the diffraction limit,” *Opt. Express* **24**, 22004-22012 (2016).
- [43] F. Yang, A. Taschilina, E. S. Moiseev, C. Simon, and A. I. Lvovsky, “Far-field linear optical superresolution via heterodyne detection in a higher-order local oscillator mode,” *Optica* **3**, 1148-1152 (2016).
- [44] W. K. Tham, H. Ferretti, and A. M. Steinberg, “Beating Rayleigh’s Curse by Imaging Using Phase Information,” *Phys. Rev. Lett.* **118**, 070801 (2017).
- [45] Z. Yu and S. Prasad, “High-numerical-aperture microscopy with a rotating point spread function,” *J. Opt. Soc. Am. A* **33**, B58-B69 (2016).
- [46] K. Y. Bliokh, F. J. Rodriguez-Fortuno, F. Nori, and A. V. Zayats, “Spin-orbit interactions of light,” *Nat. Photonics* **9**, 796 (2015).
- [47] L. Marrucci, C. Manzo, and D. Paparo, “Optical Spin-to-Orbital Angular Momentum Conversion in Inhomogeneous Anisotropic Media,” *Phys. Rev. Lett.* **96**, 163905 (2006).

References

- [48] Z. Yu and S. Prasad, “Quantum Limited Superresolution of an Incoherent Source Pair in Three Dimensions,” *Phys. Rev. Lett.* **121**, 180504 (2018).
- [49] S. Prasad and Z. Yu, “Quantum-limited superlocalization and superresolution of a source pair in three dimensions,” *Phys. Rev. A* **99**, 022116 (2019).

Chapter 2

3D Polarimetric Imaging with High Numerical Aperture Rotating PSF

2.1 Introduction

By exploiting the notion of orbital angular momentum of light beams, Prasad invented in 2013 a novel pupil-phase-engineered (PPE) point spread function (PSF) design in which as a function of defocus the PSF merely rotates without changing its shape and size [1]. This rotating PSF design permits the acquisition of the three-dimensional (3D) positional information of point sources in a snapshot mode with a larger depth of field when compared to previous rotating PSFs using a selected subset of Gauss-Laguerre (GL) modes and complicated optimization algorithms.

We organize this chapter as follows: In sections 2.2 and 2.3 we will briefly review the GL modes based rotating PSF and Prasad's original rotating PSF with scalar-field analysis. In section 2.4 we will propose a modified version of Prasad's

original rotating PSF based on the considerations of wave polarization and its evolution in propagation through an arbitrary numerical aperture (NA) imaging system which admits non-paraxial propagation and significant longitudinal components of the radiation fields. For a polarized monochromatic point dipole emitter in high NA microscopy, we will show that our modified rotating PSF is capable of performing 3D polarimetric imaging with its polarization-sensitive spatial structure and largely rigid rotation as a function of source axial displacement. Using maximum-likelihood estimation, we will show that the point dipole's 3D positional and orientational parameters can be simultaneously reconstructed from Poisson shot-noise corrupted image data in a robust fashion.

2.2 Rotating PSFs with Gauss-Laguerre Modes

2.2.1 Double-Helix PSF

The Gauss-Laguerre (GL) basis is a family of functions that form an orthogonal basis for two-dimensional complex functions [2]. Each element of the basis is indexed by two integers, m and n , which are parameters of the generalized Laguerre polynomial. m and n satisfy the relation

$$m = \pm(n - 2k), \tag{2.1}$$

where n can be any positive integer, k is an integer between $[0, n/2]$. Fig. 2.1 displays the intensity and phase of some lower order GL modes [2]. As m grows, the intensity distribution expands out, it also controls the number of times the phase vortex wraps. As n grows, the intensity and phase distributions have more concentric rings.

The GL basis is of interest to 3D imaging community because the superpositions of certain combinations of GL modes exhibit the phenomenon of continuous rotation

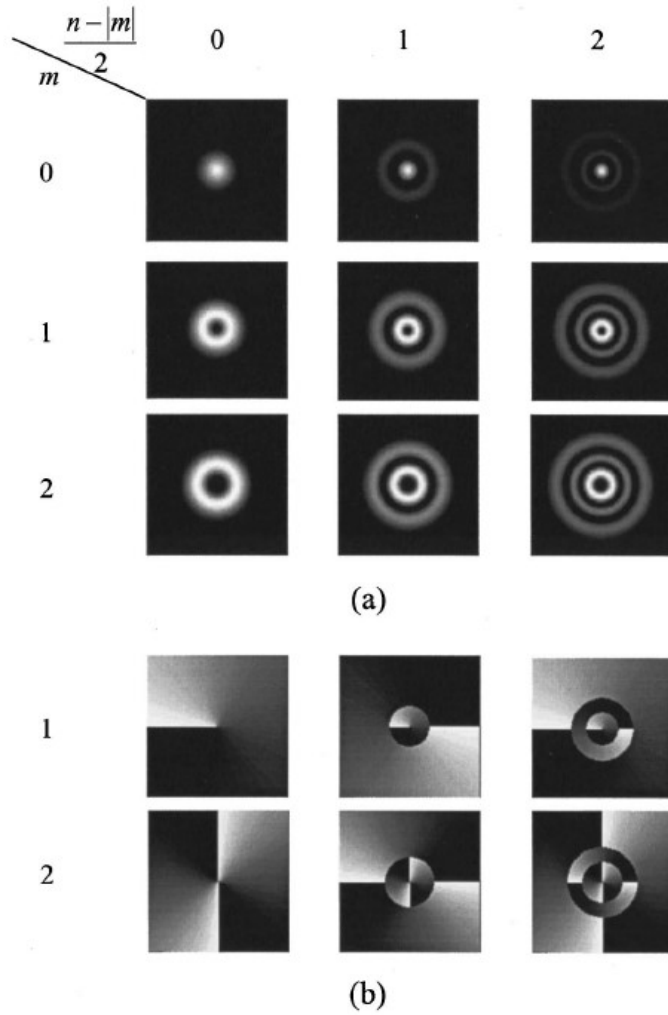


Figure 2.1: Examples of GL modes: (a) intensity, (b) phase. Image taken from Ref. [2].

as they propagate [3]. Piestun *et al.* showed that a rotating Double-Helix (DH) PSF could be formed by a superposition of Gauss-Laguerre (GL) modes that lie along a straight line in the GL modal plane [2] represented in Fig. 2.2. The rotating DH PSF system can be implemented by introducing a mask that encodes the rotating PSF transfer function in the Fourier plane of a standard imaging system. For example, the superposition of modes with indices (1,1), (3,5), (5,9), (7,13), (9,17) forms a useful

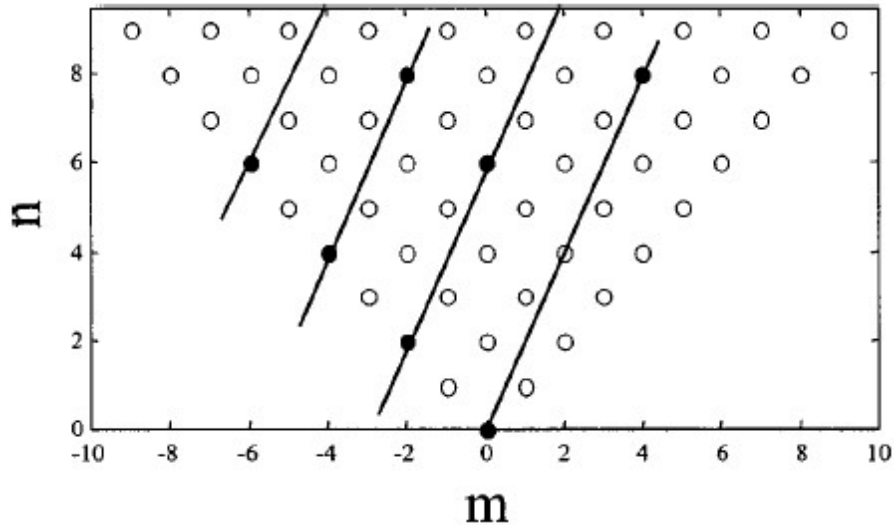


Figure 2.2: The Gauss-Laguerre modal plane. Image taken from Ref. [2].

rotating PSF transfer function. When such a GL superposition is implemented as the transfer function of an imaging system, the PSF of the system has two lobes and rotates with changing defocus.

The main disadvantage of above-mentioned rotating DH PSF is its very low transfer function efficiency, which makes it inappropriate for photon limited situations. Using an iterative optimization procedure, Pavani and Piestun [4] proposed in 2008 a new type of rotating DH PSF which solved this low efficiency problem. Their high-efficiency rotating DH PSFs are optimized to have the following attributes: (1) the rotation of the main lobes appears only within a limited volume instead of the whole 3D space, (2) maximum energy is directed towards the main lobes, and (3) the transfer function modulates only the phase.

2.2.2 Corkscrew PSF

The corkscrew PSF proposed by Lew *et al.* in W. E. Moerner's group at Stanford University [5] is also based on a superposition of GL modes (m, n) [2] equal to (1,1), (2,4), (3,7), and (4,10). Since these modes have both amplitude and phase components, directly using these modes is also highly photon inefficient.

Consequently, Lew *et al.* [5] designed an efficient phase-only mask to emulate the behavior of these modes. They optimized the corkscrew PSFs phase mask design by running an iterative optimization algorithm, using these modes as a starting point. Their algorithm used three constraints: (1) a phase-only mask in the Fourier plane of a 4f system; (2) a GL modal composition that is concentrated near the original superposition of modes described above; and (3) a Gaussian-like rotating spot in the image plane of the 4f system. The resulting phase mask and GL modal composition of the corkscrew PSF are shown in Fig. 2.3. Note that the cloud of GL modes surrounding the original superposition has the effect of limiting the rotation of the corkscrew PSF to a finite depth of field.

2.3 Prasad's Original Rotating PSF

In this section, we review the theory of Prasad's original rotating PSF [1] with scalar-field analysis.

For a phase-engineered pupil, the coherent PSF K , as a function of image-plane radial distance s_I and azimuthal angle ϕ_I , is given by the pupil integral

$$K(s_I, \phi_I; \zeta) = \frac{1}{\sqrt{\pi}} \int_{\phi=0}^{2\pi} \int_{u=0}^1 u \, du \, d\phi \exp[i2\pi\vec{u} \cdot \vec{s}_I + i\zeta u^2 - i\psi(\vec{u})], \quad (2.2)$$

where \vec{u} is the pupil-plane position vector $\vec{\rho}$ normalized by the pupil radius R , $\vec{u} = (u, \phi) = \vec{\rho}/R$, and $\vec{s}_I = (s_I, \phi_I)$ is the image-plane position vector $\vec{\rho}_I$ normalized by

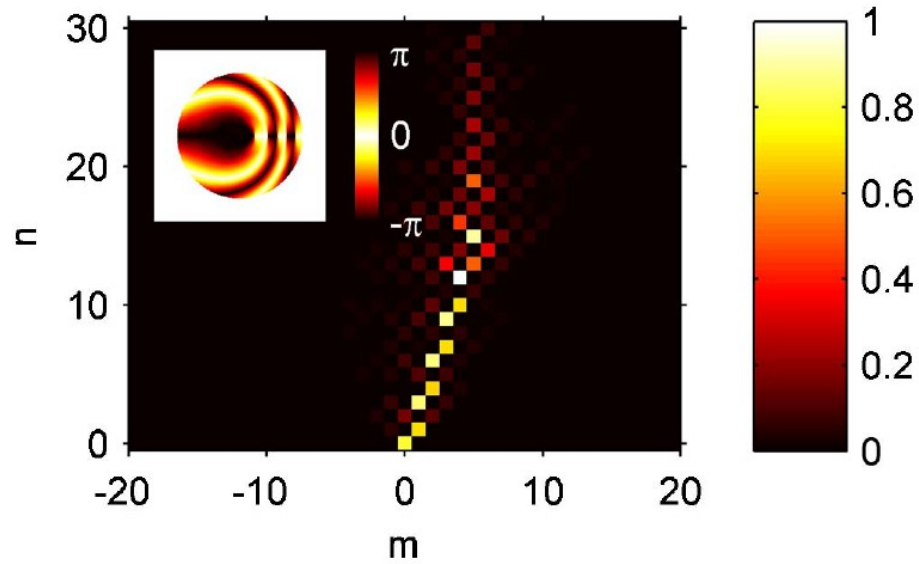
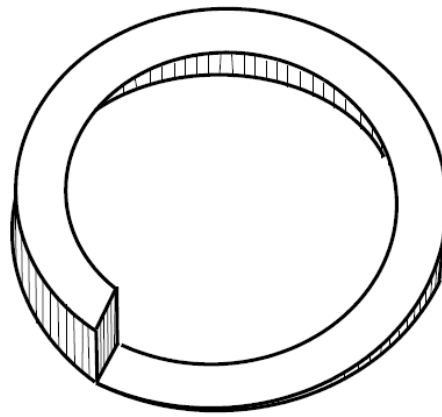


Figure 2.3: GL modal composition (m, n) of the corkscrew PSF in normalized units. Inset shows the corkscrew PSF phase mask in radians. Image taken from Ref. [5].



n-turn spiral phase in the nth zone

Figure 2.4: Schematic diagram of a specific Fresnel zone with its spiral phase retardation

the in-focus diffraction spot-radius parameter at the imaging wavelength λ for the

image plane a distance z_I from the pupil,

$$\vec{s}_I = \frac{\vec{\rho}_I}{\rho_0}, \quad \rho_0 = \frac{\lambda z_I}{R}. \quad (2.3)$$

The defocus parameter ζ at the pupil edge is related to the object-plane distance δz_O from the in-focus object plane, according to the relation

$$\zeta = -\frac{\pi \delta z_O R^2}{\lambda z_O (z_O + \delta z_O)} \simeq -\frac{\pi \delta z_O R^2}{\lambda z_O^2}, \quad \text{for } \delta z_O \ll z_O, \quad (2.4)$$

where z_O is the distance between the lens and the plane of Gaussian focus. For a pupil phase mask with L annular Fresnel zones, the spiral phase structure $\psi(\vec{u})$ consists of spiral phases of integer winding number in the various zones, with the winding number changing from one zone to the next by a fixed integer step and all phase dislocation lines oriented along the same radial direction. For a low-NA imager the outer radii of the zones are chosen to scale as the square root of the zone index, which amounts to the following spiral phase structure in the pupil:

$$\psi(\vec{u}) = \psi(u, \phi) = \left\{ (al + b)\phi \left| \sqrt{\frac{l-1}{L}} \leq u < \sqrt{\frac{l}{L}}, \quad l = 1, \dots, L \right. \right\}, \quad (2.5)$$

where a and b are any two integers. The magnitude of a which is the step size of the phase winding number change from one zone to the next, controls the number of primary lobes in the PSF. The sign of a , on the other hand, determines the sense of rotation of the PSF with changing δz_O . The simplest form for the spiral phase structure is $a = \pm 1$ and $b = 0$, for which we have a single-lobe PSF. Fig. 2.4 shows a schematic of one of the Fresnel zones.

For the spiral phase structure with $a = 1$ and $b = 0$, the coherent PSF K may be expressed as

$$K(s_I, \phi_I; \zeta) = \frac{2\pi}{\sqrt{\pi}} \sum_{l=1}^L i^l \exp(-il\phi_I) \int_{\sqrt{(l-1)/L}}^{\sqrt{l/L}} du u J_l(2\pi u s_I) \exp(i\zeta u^2), \quad (2.6)$$

where we used the identity

$$\int_0^{2\pi} d\phi \exp[ix \cos(\phi - \phi_I) - il(\phi - \phi_I)] = 2\pi i^l J_l(x). \quad (2.7)$$

For sufficiently small s_I the radial integrals over u may be performed approximately by treating the slowly varying Bessel function J_l as a constant over the l th zone. The remaining exponential integral then can be evaluated exactly as

$$\int_{\sqrt{(l-1)/L}}^{\sqrt{l/L}} du u \exp(i\zeta u^2) = \exp[i\zeta(l - 1/2)/L] \frac{\sin[\zeta/(2L)]}{\zeta}, \quad (2.8)$$

the coherent PSF in (2.6) may thus be approximated by the sum

$$K(s_I, \phi_I; \zeta) \approx 2\sqrt{\pi} \exp[-i\zeta/(2L)] \frac{\sin[\zeta/(2L)]}{\zeta} \times \sum_{l=1}^L i^l \exp[-il(\phi_I - \zeta/L)] J_l(2\pi\sqrt{l/L}s_I). \quad (2.9)$$

We see that each term in the sum in Eq. (2.9) depends on ϕ_I and ζ only via $\phi_I - \zeta/L$. Since the overall prefactor in Eq. (2.9) is essentially independent of ζ for $\zeta \ll L$, the PSF should rotate uniformly with changing defocus at the rate $1/L$ with excellent shape and size invariance. Since this invariance holds approximately out to $\zeta \sim L$, increasing the number of Fresnel zones will extend the shape invariance of the PSF to a larger range of defocus values. The PSF performs a complete rotation with ζ over the range $[-2L\pi, 2L\pi]$, but when $|\zeta| = 2L\pi$, the prefactor in Eq. (2.9) vanishes, indicating that the PSF must break apart as $|\zeta|$ approaches $2L\pi$ from below.

We can numerically evaluate Eq. (2.5) by using the two-dimensional fast Fourier transform (*fft2* code in MATLAB). In Fig. 2.5 we display the rotation of the incoherent rotating PSF $|K|^2$ for two different values of L , namely 7 and 9, for defocus phase at the pupil edge changing from -24 to 24 rad. For comparison, we also display the ideal diffraction-limited PSF (IDL-PSF) without any phase mask over the same range of defocus values in the bottom row. The main lobe of the PPE-PSF maintains its compact elliptical core and rotates with changing defocus in a nearly shape- and size-invariant manner out to the largest defocus value, the rate of rotation with changing defocus is indeed larger for $L = 7$ than for $L = 9$. The IDL-PSF has a

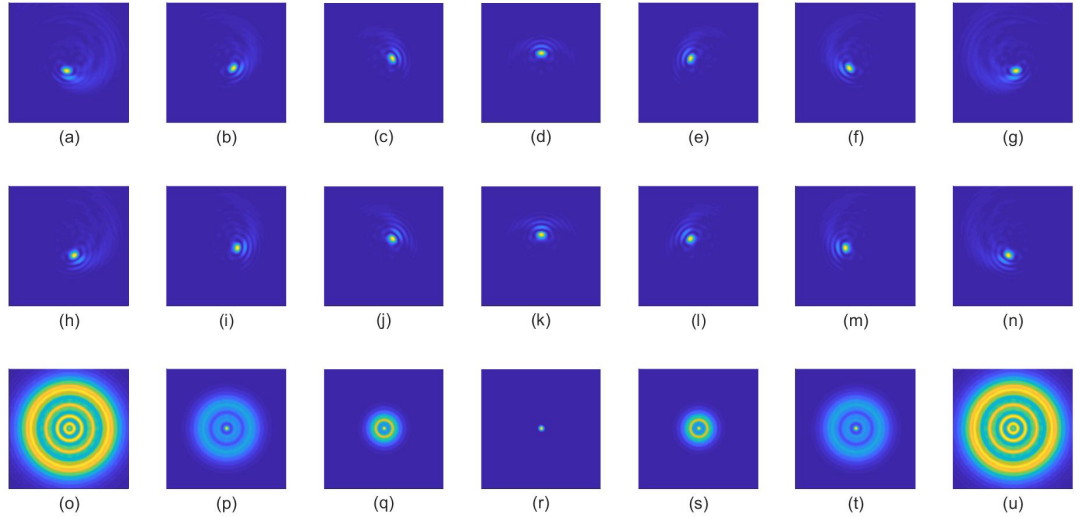


Figure 2.5: Incoherent PPE-PSF with $L = 7$ (top row) and $L = 9$ (middle row). The IDL-PSF, is shown for comparison in the bottom row. The plots from left to right are for increasing values of defocus, from -24 radians to $+24$ radians of defocus in steps of 8 radians, at the edge of the pupil.

very tight Airy form when the source is in focus, but spreads rapidly with increasing defocus, resulting in poor 3D resolution and sensitivity.

Being based on nondiffracting Bessel modes [6, 7, 8], Prasad’s rotating PSF has a superior depth of field (DOF) when compared to previous rotating PSFs [4, 5, 9], all of which combine diffracting GL vortex modes that spread more readily with propagation. A clear performance comparison between different rotating PSFs was nicely made in the dissertation work of Dr. Rakesh Kumar [10], a former Ph.D. student in Dr. Prasad’s research group. Prasad’s novel rotating PSF design is also highly versatile and analytically quite tractable, since by changing just the parameters a and b in the phase mask, one can obtain rotating PSFs with different geometrical structures, all capable of achieving 3D imaging [10, 11].

2.4 High NA Rotating PSF

2.4.1 Introduction

In this section we consider the modification of Prasad’s original rotating PSF that results from the evolution of wave polarization, as the image-forming wave non-paraxially propagates through a high NA imaging system with significant longitudinal components. The vector-field treatment of image formation we present here is based on the pioneering work of Richards and Wolf [12, 13], which has been extensively used in various settings for optical fields passing through high NA focusing elements [14]-[17].

Except for positional information, the polarization state of emission has been probed over the years [18]-[27] in the single-molecular imaging community. Polarimetric information, including the orientation of the emitting dipole, is important for reducing systematic errors in localizing the polarized emitters and assessing their local molecular environment [28]. Since the rotational symmetry of the optical system is broken by the anisotropic spiral phase structure, different emitter polarizations correspond to different shapes of the point spread function, with these differences accentuated by the large NA of the imager. From the 2D position of the center of rotation, the angle of rotation about that center, and the shape of the image, our rotating PSF imager can thus simultaneously localize a point source in full 3D and capture its polarization state of emission without any need for polarization sensors. The main work in this section was published in Ref. [29].

2.4.2 Radiation Field from a Point Dipole Emitter

Consider a point electric dipole source located at position \vec{r}_O , with dipole moment $\vec{p} \exp(-i\omega t)$ oscillating at angular frequency ω . The electric field radiated by the dipole at point \vec{r} in the radiation zone may be described by the matrix relation [30]

$$\underline{E}(\vec{r}, \vec{r}_O) = \frac{k_O^2 \exp(ik_O |\vec{r} - \vec{r}_O|)}{4\pi\epsilon_0 |\vec{r} - \vec{r}_O|} (\mathbf{I} - \hat{n} \hat{n}^T) \underline{p}, \quad (2.10)$$

where $k_O = n_O \omega / c$, n_O is refractive index of the medium in which the radiating dipole is embedded, and each underlined vector is to be regarded as a 3×1 column vector with elements that are the Cartesian components of the corresponding spatial vector, indicated by an overhead arrow or caret sign (for unit vectors). Here \mathbf{I} is the identity matrix, $\hat{n} = (\vec{r} - \vec{r}_O) / |\vec{r} - \vec{r}_O|$ is the unit observation vector, and the superscript T denotes matrix transpose. For brevity, we omit a pure time-dependent exponential, $\exp(-i\omega t)$, from (2.10) and all subsequent expressions for the complex field. For sources close to the origin, for which $r_O \ll r$ that we assume to be true, we may replace in (2.10) \hat{n} by $\hat{r} = \vec{r}/r$, and $|\vec{r} - \vec{r}_O|$ in the denominator by r but in the exponential by the more accurate approximation, $r - \hat{r} \cdot \vec{r}_O$, which would accommodate location-dependent phase changes that can be large if kr_0 is large. Within these approximations, the electric-field vector (2.10) takes the form

$$\underline{E}(\vec{r}, \vec{r}_O) = \frac{k_O^2 \exp(ik_O r - ik_O \hat{r} \cdot \vec{r}_O)}{4\pi\epsilon_0 r} \mathbf{M}_O(\hat{r}) \underline{p}, \quad (2.11)$$

in which the matrix \mathbf{M}_O is defined as

$$\mathbf{M}_O(\hat{r}) = \mathbf{I} - \hat{r} \hat{r}^T. \quad (2.12)$$

2.4.3 Action of the Focusing, Polarizing, and Spiral Phase Elements

We assume in this section a perfect primary image-capture optical element, typically the objective in a microscope, that images a point source as a point image with

perfect geometrical focusing over its typically large NA. Such a perfect focusing element turns a diverging spherical wavefront from a point into a converging spherical wavefront, as shown in Fig. 2.6. Under conditions of exit-pupil radius and object and image-plane distances being much larger than the light wavelength, Wolf and Richards [13] provided a comprehensive treatment of approximate diffractive vector-field propagation in an imaging system. By means of an accurate stationary-phase approximation, this approach treats each source ray as a plane wave with an associated transverse polarization that undergoes the transformation appropriate to the transmission of a plane wave locally at the point at which the ray intersects the surface of the focusing element [31]. Applications of this approach to high NA single-molecule microscopy have been proposed by a number of authors [20, 26, 32].

An ideal high-NA focusing element acts in three important ways. First, it rotates the electric field vector locally so the electric field of a light ray leaving the element, just as the electric field of a light ray incident on it, stays transverse to the direction of the ray. Second, if we assume perfectly transmissive optics, its interaction with the optical wavefront modifies the amplitude of the wavefront in such a manner that the optical power is conserved locally. Third, it changes the phase of the incident wavefront in a pupil-position-dependent manner to turn it into a converging wavefront. As shown in Fig. 2.6, this phase change in the pupil at location \vec{r} , relative to that at the pupil center, is by amount

$$\delta\phi(\vec{r}) = -k_O\overline{AB} - k_I\overline{BC} = -k_O(r - z_O) - k_I(|\vec{r}_{I0} - \vec{r}| - z_I), \quad (2.13)$$

where $k_I = n_I\omega/c$ is the optical propagation constant in the image space of refractive index n_I , \vec{r}_{I0} is the location of the Gaussian image of a point source at the origin under perfect geometrical focusing. The image plane will be taken to be a distance z_I away from the plane of the exit pupil. We shall take z_O and z_I to be large compared to the optical wavelength, $\lambda = 2\pi c/\omega$, which is a necessary condition for the validity

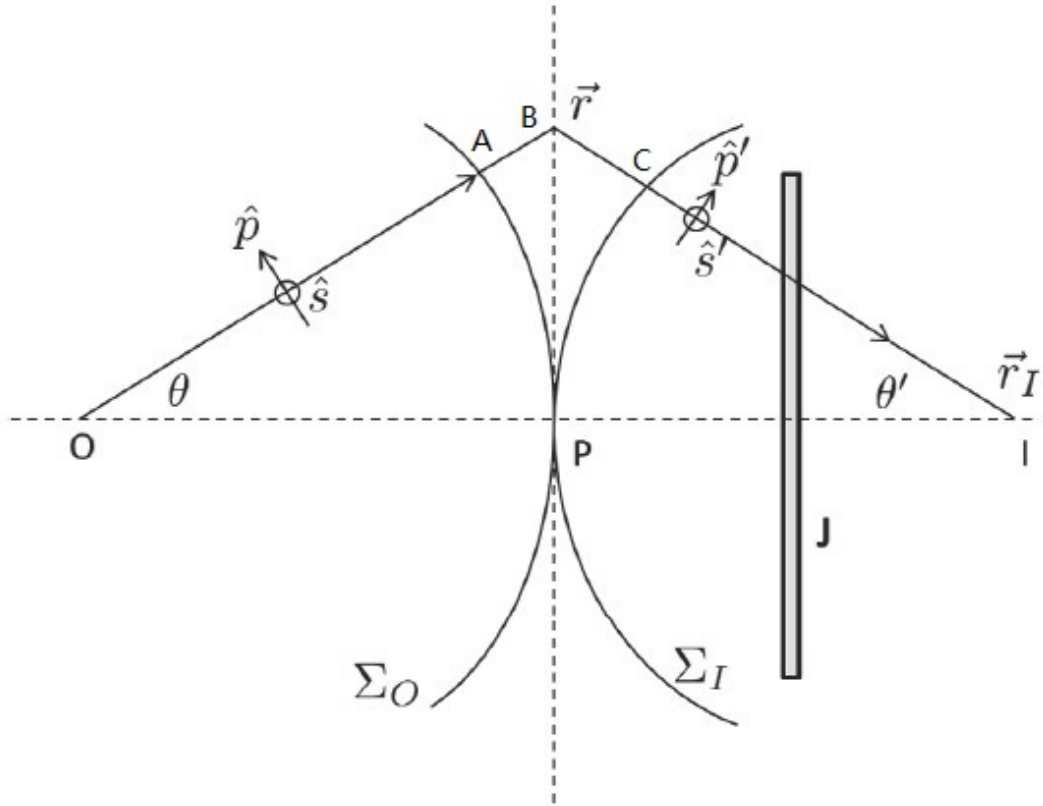


Figure 2.6: Transformation of an incident wavefront Σ_O into the outgoing (imaging) wavefront Σ_I , with the pupil shown by a dashed vertical line. The two linear s and p polarizations for a typical ray crossing the two wavefronts are also shown. A polarization analyzer, denoted by **J**, is inserted in the beam path following the focusing lens.

of our analysis and is typically an excellent assumption.

In a practical high-NA microscope, with the sample placed under a cover slip and an immersion liquid between the slip and the objective, even the slightest optical phase and amplitude changes from depth variations of the fluorescent label molecules and index fluctuations result in aberrations that can compromise the ability to achieve extreme sub-wavelength 3D localization of the labels. Spherical aberration is another geometric phase error, quartic in pupil coordinates in the lowest

order, that cannot be entirely compensated in a high-NA system and must be added to (2.13). Further, transversely varying amplitude changes caused by the reflection of rays incident at large angles at the optical surfaces of the objective amount, in effect, to an apodization of the pupil, but this is typically mitigated by suitable anti-reflection coatings. We shall assume here that all such complications have been largely eliminated by proper design, and treat the microscope as a perfect geometrical imager. Equivalently, the results of this chapter may be regarded as providing upper bounds on the performance of a practical microscope.

The field vector will be expressed in terms of its s and p linear polarizations with respect to (w.r.t.) the ray direction, with unit orthonormal basis vectors (\hat{s}, \hat{p}) and (\hat{s}', \hat{p}') in the object and image spaces, respectively, with the identity of the s polarizations in the two spaces imposed. The rotation of the field vector is described by the matrix, \mathbf{M}_L ,

$$\mathbf{M}_L(\vec{r}) = \underline{\hat{s}} \underline{\hat{s}}^T + \underline{\hat{p}'} \underline{\hat{p}'}^T, \quad (2.14)$$

where \hat{p}' is obtained by rotating \hat{p} by angle $(\theta + \theta')$ about the fixed polarization vector, \hat{s} , with the angles θ and θ' being the inclination angles for the two rays w.r.t. the optical axis, which we take to be the z axis, *i.e.*, $\theta = \cos^{-1}(z_O/r)$, $\theta' = \cos^{-1}(z_I/|\vec{r} - \vec{r}_{I0}|)$. Since \hat{s} and \hat{p} are simply the spherical-coordinate basis vectors $\hat{\phi}$ and $\hat{\theta}$, respectively, it follows that

$$\hat{p}' = \hat{r} \sin(\theta + \theta') + \hat{\theta} \cos(\theta + \theta'). \quad (2.15)$$

These relations between the polarization basis vectors and the coordinate basis vectors may be used to express \mathbf{M}_L explicitly in terms of the spherical coordinates of the pupil point, \vec{r} , w.r.t. the reference source point taken at the origin of the coordinate system.

The polarizing optical element, denoted by \mathbf{J} in Fig. 2.6, follows the focusing element in the beam path. Its purpose is to analyze the image-forming beam in

its two transverse polarization components in order to examine how the different polarizations of the beam are transformed by the imager, depending on the state of polarization of the emitting dipole. In the simplest case of a perfect polarizer, it is described by the matrix operator,

$$\mathbf{J} = \underline{\hat{e}} \underline{\hat{e}}^\dagger, \quad (2.16)$$

where $\underline{\hat{e}}$ is the unit polarization vector representing the polarization being analyzed. For a linear polarizer, this vector may be $\underline{\hat{x}}$ or $\underline{\hat{y}}$ for the x or y polarization, while for the case where no polarization analysis of the imaging beam is performed, \mathbf{J} is simply the identity matrix (in the polarization plane). We shall consider three specific examples of \mathbf{J} here, namely $\underline{\hat{x}} \underline{\hat{x}}^T$, $\underline{\hat{y}} \underline{\hat{y}}^T$, and the identity matrix, represented by their sum. These are all represented by the single idempotent matrix,

$$\mathbf{J} = \alpha \underline{\hat{x}} \underline{\hat{x}}^T + \beta \underline{\hat{y}} \underline{\hat{y}}^T, \quad \mathbf{J}^2 = \mathbf{J}, \quad (2.17)$$

in which (α, β) is either (1,0) or (0,1) or (1,1).

In the absence of any polarization dependence of either the lens or the phase mask, which we assume here, the wavefront phase change (2.13) resulting from perfect lens focusing and that due to the spiral phase mask, $\Psi(u, \phi)$, amount to a multiplication of the incident EM field by the corresponding complex phase exponentials.

On the whole, thus, the propagation of the field from the source dipole to the pupil plane, as described by (2.11), followed by the action of the focusing and polarizing elements, as described by (2.13), (2.14), and (2.17), and imposition of the engineered pupil phase, yield the following transformation of the source dipole-moment vector to the column vector representing the electric field of the imaging radiation in the exit pupil:

$$\begin{aligned} \underline{p} \longrightarrow \underline{E}'_P(\vec{r}) &= \frac{k_O^2 e^{ik_O r - ik_O \hat{r} \cdot \vec{r}_O}}{4\pi\epsilon_0 r} \exp[i\delta\phi(\vec{r}) + i\psi(u, \phi)] \\ &\times \mathbf{J} \mathbf{M}_L(\vec{r}) \mathbf{M}_0(\hat{r}) \underline{p}. \end{aligned} \quad (2.18)$$

2.4.4 Propagation to the Image Plane

As noted in [13], the use of geometrical optics to describe the rotation of the ray and associated field polarization at optical interfaces from the object to the image space entails a modification of the electric-field amplitude, even when there is no loss of light due to reflection or absorption. Since an area element dA of the exit-pupil plane is transformed to area elements, $dA \cos \theta$ and $dA \cos \theta'$, when projected orthogonal to the ray directions on the object and image sides, respectively, energy conservation requires that the incoming and outgoing radiation fluxes on the two sides, proportional to $n_0 |\vec{E}_O|^2 \cos \theta dA$ and $n_I |\vec{E}_I|^2 \cos \theta' dA$, be equal to each other. This implies the following modification of the field amplitude between the object and image spaces:

$$|\vec{E}_I| = \sqrt{\frac{n_O \cos \theta}{n_I \cos \theta'}} |\vec{E}_O|. \quad (2.19)$$

We shall henceforth set n_I to 1, as is typical for a practical microscope, so $k_I = k = \omega/c$.

The electric field vector in the image plane is given by a diffractive propagation of the pupil-plane field on the right-hand side (RHS) of (2.18) to the image plane. In view of the assumption that the aperture and image-plane distance are large compared to the wavelength, the image-plane field at position \vec{r}_I , accounting for the amplitude adjustment factor (2.19), is given by the Rayleigh-Sommerfeld diffraction formula,

$$\begin{aligned} \vec{E}_I(\vec{r}_I) &= \frac{k}{2\pi i} \int P(\vec{\rho}) \sqrt{\frac{n_O \cos \theta}{\cos \theta'}} \vec{E}'_P(\vec{r}) \frac{e^{ik|\vec{r}_I - \vec{r}|}}{|\vec{r}_I - \vec{r}|} \cos \theta' d^2 \rho \\ &= \frac{k \sqrt{n_O}}{2\pi i} \int P(\vec{\rho}) \sqrt{\cos \theta \cos \theta'} \vec{E}'_P(\vec{r}) \frac{e^{ik|\vec{r}_I - \vec{r}|}}{|\vec{r}_I - \vec{r}|} d^2 \rho, \end{aligned} \quad (2.20)$$

where $P(\vec{\rho})$ is the pupil function, typically the binary indicator function taking the value 1 inside the pupil and 0 outside. The specific choice of the obliquity factor,

$\cos \theta'$, given by

$$\cos \theta' = z_I / |\vec{r}_I - \vec{r}|, \quad (2.21)$$

in the first equation in (2.20) results from the use of the Dirichlet boundary condition for a planar aperture in the radiation zone, as shown in Ref. [33]. Its preference over other competing forms of the obliquity factor is justified in Appendix A by a careful angular-spectrum based analysis of the diffractive propagation law. The square-root factor in the integrand of the first equation adjusts the field amplitude, as required by (2.19), and gives rise to a more symmetrical form for the overall obliquity factor, which, as we show in Appendix B, yields a rigorous conservation of the optical flux.

On substituting (2.18) into (2.20) and using (2.13), along with $k_O = k n_O$, we obtain the following expression for the image-plane electric field written in the column-vector form:

$$\begin{aligned} \underline{E}_I(\vec{r}_I) = & \frac{k^3 n_O^{5/2} e^{ik(n_O z_O + z_I)}}{8i\pi^2 \epsilon_0} \int d^2 \rho P(\vec{\rho}) \frac{e^{i\Phi(\vec{r}, \vec{r}_I)}}{r |\vec{r}_I - \vec{r}|} \\ & \times \sqrt{\cos \theta \cos \theta'} \mathbf{J} \mathbf{M}_L(\vec{r}) \mathbf{M}_O(\hat{r}) \underline{p}, \end{aligned} \quad (2.22)$$

where the overall phase function in the pupil has the value

$$\Phi(\vec{r}, \vec{r}_I) = \psi(u, \phi) + k(|\vec{r}_I - \vec{r}| - |\vec{r}_{I0} - \vec{r}| - n_O \hat{r} \cdot \vec{r}_O). \quad (2.23)$$

This phase may be well approximated by expanding the difference between the first two terms inside the parentheses on the RHS of (2.23) to first order in the vector separating the image point \vec{r}_I from the Gaussian image point \vec{r}_{I0} ,

$$\Phi(\vec{r}, \vec{r}_I) = \psi(u, \phi) + k[\hat{k}_I \cdot (\vec{r}_I - \vec{r}_{I0}) - n_O \hat{r} \cdot \vec{r}_O], \quad (2.24)$$

where \hat{k}_I is the unit vector along the image-space ray from \vec{r} to \vec{r}_{I0} ,

$$\hat{k}_I = \frac{(\vec{r}_{I0} - \vec{r})}{|\vec{r}_{I0} - \vec{r}|}. \quad (2.25)$$

2.4.5 Generalized Spiral Phase Profile

For an axially defocused point dipole, for which $\vec{r}_O = \delta z_O \hat{z}$, the pupil phase retardation resulting from its defocus, according to (2.24), is $-kn_O \hat{r} \cdot \vec{r}_O = -kn_O \delta z_O \cos \theta$, along a ray from the source intersecting the pupil at position $\vec{\rho}$ and making angle θ with the optical axis. This added phase retardation from axial defocus increases over the pupil as the incident ray angle θ is changed from 0 (at pupil center) to $\tan^{-1}(R/z_O)$ (at the edge of the pupil of radius R). We subdivide the pupil into L contiguous annular zones, much as we did in the paraxial analysis of the rotating PSF imager, but now choose the outer radius, ρ_l , of the l th zone by requiring that at pupil points at this radial distance the defocus-induced phase retardation relative to the central ray, namely $kn_O \delta z_O (1 - \cos \theta)$ at $\rho = \rho_l$, be proportional to $l \delta z_O$, *i.e.*,

$$kn_O \delta z_O \left(1 - \frac{z_O}{\sqrt{z_O^2 + \rho_l^2}} \right) = \gamma l \delta z_O. \quad (2.26)$$

With the choice (4.3) for the spiral phase, the overall pupil phase (2.24) at the outer radius of the l th zone will then have the requisite rotational form, $l(a\phi + \gamma \delta z_O)$, with respect to the azimuthal and defocus coordinates. Dividing (2.26) by its value corresponding to the outermost zone, for which $l = L$ and $\rho_L = R$, eliminates the proportionality constant, γ , and yields the outer radius of the l th zone by the relation:

$$\frac{1 - \frac{z_O}{\sqrt{z_O^2 + \rho_l^2}}}{1 - \frac{z_O}{\sqrt{z_O^2 + R^2}}} = \frac{l}{L}, \quad (2.27)$$

which may be expressed in terms of the (object-side) NA, namely $\text{NA} = n_O R / (z_O^2 + R^2)^{1/2}$, if necessary. For paraxial propagation, $\rho_l \leq R \ll z_O$, relation (2.27) simplifies to the choice, $\rho_l = R(l/L)^{1/2}$, made in Ref. [1].

We shall set $n_O = 1$ in the rest of the dissertation for the purposes of our theoretical analysis, henceforth regarding NA as being a purely geometrical aperture

variable, namely $\sin \theta_O$. It would be simple enough to re-insert any factors involving n_O for liquid-immersed objectives to restore the full definition of NA and expressions for the electric field in the rest of the dissertation.

2.4.6 Polarization Dependent Rotating PSF

We take the detector plane to be orthogonal to the optical (z) axis of the imager. The expected image intensity, $I(\vec{r}_I)$, on the detector is then given by the z component of the time-averaged Poynting vector,

$$I(\vec{r}_I) = \frac{1}{2} \text{Re } \hat{z} \cdot [\vec{E}_I(\vec{r}_I) \times \vec{H}_I^*(\vec{r}_I)] \quad (2.28)$$

where the magnetic field, $\vec{H}_I(\vec{r}_I)$, at the image plane may be calculated by applying Faraday's law to (2.22). For a vanishingly small image-side numerical aperture that we assume throughout this dissertation, $R \ll z_I$, $\vec{H}_I(\vec{r}_I)$ turns out to be essentially $(\epsilon_0/\mu_0)^{1/2} \hat{z} \times \vec{E}_I(\vec{r}_I)$, so the use of the simple vector triple product identity in (2.28) implies the following expression for $I(\vec{r}_I)$:

$$I(\vec{r}_I) = \frac{1}{2} \sqrt{\frac{\epsilon_0}{\mu_0}} |\hat{z} \times \vec{E}_I(\vec{r}_I)|^2. \quad (2.29)$$

The full rotational character of the intensity (2.29) and its dependence on the state of polarization of the emitter may be made more explicit by evaluating the product $\mathbf{J} \mathbf{M}_L(\vec{r}) \mathbf{M}_O(\hat{r}) \underline{p}$ present in (2.22) and then substituting for $\Psi(u, \phi)$ its spiral phase structure that we discussed in the previous section.

As we show in Appendix C, this yields the following expression for the electric field:

$$\begin{aligned} \hat{z} \times \vec{E}_I(\vec{r}_I) = & \frac{k^3 \sqrt{z_O} R^2 \exp[ik(z_O + z_I)]}{16i\pi^2 \epsilon_0 z_I} \int d^2u P(Ru) \\ & \times (1 + u^2 \tan^2 \theta_O)^{-3/4} \exp \left[-i 2\pi \vec{u} \cdot \vec{s}_I \right. \\ & \left. + i\psi(u, \phi) - i \frac{k\delta z_O}{(1 + u^2 \tan^2 \theta_O)^{1/2}} \right] \vec{F}(\theta, \phi), \end{aligned} \quad (2.30)$$

where $\theta_O = \sin^{-1}(\text{NA})$ is the half angle of the light cone incident on the objective, $\vec{u} = \vec{\rho}/R$ is the normalized pupil-position vector we defined earlier, $\vec{s}_I = \vec{r}_I/(\lambda z_I/R)$ is the image-plane position vector in units of the Airy disk radius, and \vec{F} is the following function of spherical angles in the object space:

$$\begin{aligned} \vec{F}(\theta, \phi) = & \hat{x}\beta\{p_x \sin 2\phi(1 - \cos \theta) - p_y[(1 + \cos \theta) \\ & + \cos 2\phi(1 - \cos \theta)] + 2p_z \sin \phi \sin \theta\} \\ & + \hat{y}\alpha\{p_x[(1 + \cos \theta) - \cos 2\phi(1 - \cos \theta)] \\ & - p_y \sin 2\phi(1 - \cos \theta) - 2p_z \cos \phi \sin \theta\}. \end{aligned} \quad (2.31)$$

In the limit of low NA, *i.e.*, for $\sin \theta_O \ll 1$, we may set θ equal to 0 in (2.31), which reduces \vec{F} to the constant vector, $2(-\beta p_y \hat{x} + \alpha p_x \hat{y})$, along which the magnetic field vector of the imaging beam is oriented in this limit. We may extract from the image intensity data, proportional to $|\vec{F}|^2 \sim (\alpha^2 |p_x|^2 + \beta^2 |p_y|^2)$, the magnitudes of p_x and p_y separately by means of a polarization analysis along the x and y axes, corresponding to (α, β) taking the value (1,0) and (0,1), respectively. The image fields, being transverse, are insensitive, however, to the longitudinal (z) component of the dipole in the low-NA limit. Importantly, the rotational character of the PSF resulting from the combination of the last two terms in the exponential inside the integrand of (2.30) is fully preserved, resulting in a relatively long interval of axial defocus, δz_O , around 0 over which the PSF largely rotates uniformly about the Gaussian image point with changing axial position of the emitter, as predicted in [1].

For moderate to high NA, on the other hand, the three components of the dipole emitter affect the image field differently. By first expressing the sine and cosine functions of ϕ as combinations of complex, pure-phase exponentials, writing $\vec{u} \cdot \vec{s}_I$ as $u s_I \cos(\phi - \phi_I)$, and then transforming $\phi \rightarrow \phi + \phi_I$, we see that the different terms in $\vec{F}(\theta, \phi)$ contribute terms in the PSF, which, although all rotating at the

same rate with changing axial position, are superposed coherently with ϕ_I dependent coefficients in the image plane. Even though the rotational character of the PSF contributed by the combination of $\psi(u, \phi)$ and the defocus-dependent phase term in (2.30) is thus no longer exact for a general dipole orientation, the PSF, as we shall see presently, still rotates approximately, while maintaining its general shape, with changing values of defocus over an extended range that is rather similar to that for the case of low NA.

By integrating (2.28) over the image plane and using (2.29), we obtain the total time-averaged power

$$P(p_x, p_y, p_z) \sim \int_0^{2\pi} \int_{u=0}^1 d\phi du u(1 + u^2 \tan^2 \theta_O)^{-3/2} |\vec{F}|^2. \quad (2.32)$$

According to expression (2.31) for \vec{F} with $\alpha = \beta = 1$, the total power integrals for purely x and z-polarized dipole have the forms

$$P(1, 0, 0) \sim \int_0^1 du u(1 + u^2 \tan^2 \theta_O)^{-3/2} 2(1 + \cos^2 \theta), \quad (2.33)$$

and

$$P(0, 0, 1) \sim \int_0^1 du u(1 + u^2 \tan^2 \theta_O)^{-3/2} 4 \sin^2 \theta, \quad (2.34)$$

after the ϕ integration. Utilizing relations $\tan \theta = (Ru)/Z_O$ and $\cos \theta = (1 + u^2 \tan^2 \theta_O)^{-1/2}$, the above integrals over u can be transformed to

$$P(1, 0, 0) \sim \int_0^{\theta_O} d\theta 2 \sin \theta (1 + \cos^2 \theta); \quad P(0, 0, 1) \sim \int_0^{\theta_O} d\theta 4 \sin^3 \theta. \quad (2.35)$$

Therefore the ratio of $P(0, 0, 1)$ to $P(1, 0, 0)$ can be evaluated as

$$\frac{P(0, 0, 1)}{P(1, 0, 0)} = \frac{2(2 - \cos \theta_O - \cos^2 \theta_O)}{4 + \cos \theta_O + \cos^2 \theta_O}, \quad (2.36)$$

where $\theta_O = \sin^{-1}(\text{NA})$. In Fig. 2.7 we plot the ratio (2.36) to show that it grows with increasing NA.

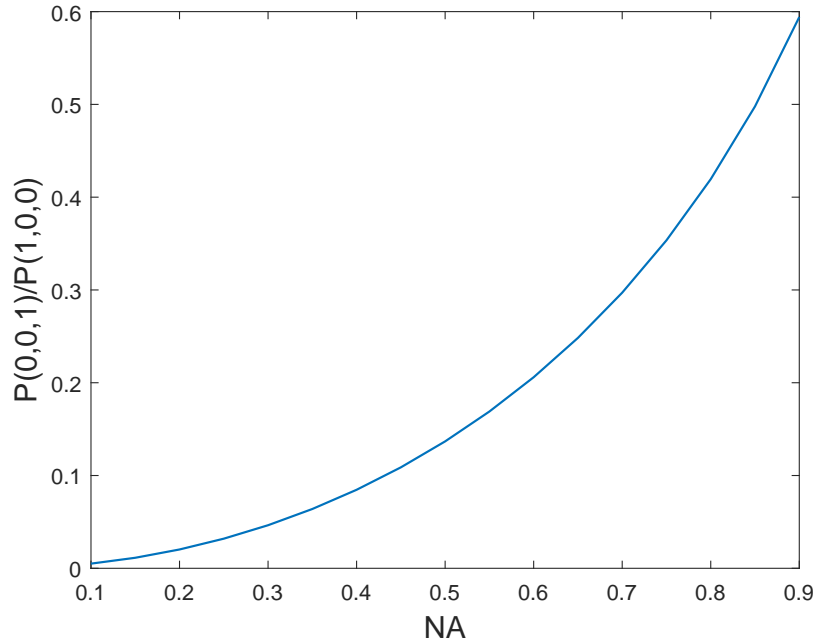


Figure 2.7: Ratio of $P(0,0,1)$ to $P(1,0,0)$ vs NA.

We now illustrate graphically the modification of the spatial pixel-wise distribution of the PSF signal, $I(\vec{r}_I)$, that results from changing the state of 3D polarization of the point dipole emitter and how these modifications are accentuated by increasing the NA of the imaging microscope. In the next two figures, no polarization analysis of the PSF has been performed, *i.e.*, $\alpha = \beta = 1$, so the total PSF signal power is being plotted in each instance. As we shall see, with increasing NA, the differences among the PSFs for the various transversely polarized emitters increase, but their differences from the PSF for the longitudinally polarized emitter decrease. A linear polarization analysis of the PSF signal, achieved by setting (α, β) to either $(1,0)$ or $(0,1)$ in (2.31), can, however, magnify these differences, as we shall discuss later.

In the four panels of Fig. 2.8, we display the PSF corresponding to the point dipole emitting in x -polarized (XP; top left), y -polarized (YP; top right), left circularly polarized (LCP; bottom left), and z -polarized (ZP; bottom right) states. The axial

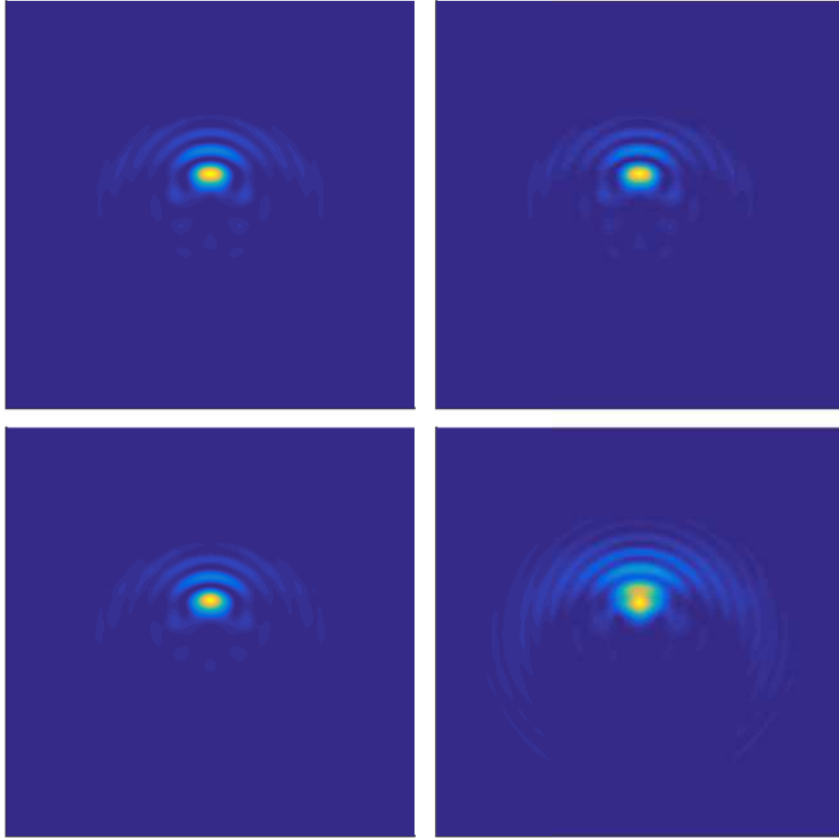


Figure 2.8: The PSF signal, for low NA of value 0.2, for XP (top left); YP (top right); LCP (bottom left) ; and ZP (bottom right) state of emission for the point dipole emitter located in the plane of Gaussian focus, for a seven-zone phase mask, $L = 7$, with $a = 1$, $b = 0$. The full array size in each panel is 16×16 in units of squared Airy disk radius (see text). The color coding in each PSF, with yellow representing its brightest pixel and blue its faintest, is only for the ease of visualization of its spatial structure. The brightest pixel of the PSF in the bottom right plot is, in fact, over 100 times fainter than those for the other three plots, which agrees well with Fig. 2.7. Image taken from Ref. [29].

defocus parameter, defined here as $k\delta z_O$, which is simply 2π times the number of waves of axial displacement of the source from the plane of Gaussian focus, was chosen to be 0 for these plots, but in subsequent plots we have changed its value over a wide range to see how the PSF rotates with changing axial displacement of the

source point. For the plots in Fig. 2.8, NA was chosen to be low at 0.2, corresponding to $R/z_O = 0.204$, while the PSFs corresponding to the same four polarization states for a high value of NA, namely 0.9, for which $R/z_O = 2.06$, are shown in Fig. 2.9. For the low NA value, all cases of transversely polarized dipoles generated PSF intensity patterns that are rather indistinguishable, both in their spatial structure and the intensity of their brightest pixel, but for the longitudinally polarized dipole emission (bottom right), the brightest pixel was considerably fainter by a factor of over a hundred, which is consistent with the small ratio shown in Fig. 2.7 for low NA. The spatial form of the PSF in the latter case is also perceptibly different from those of the others.

A comparison of Figs. 2.8 and 2.9 shows that with increasing geometric NA, the differences of the PSFs corresponding to the source dipole emitting in different transverse polarization states (XP, YP, or LCP) grow, becoming sufficiently different in form that their differences can be exploited to recover the full state of polarization of the emitter. By contrast, the brightness of the PSF signal for the purely longitudinally polarized emitter tends to catch up with that for the transversely polarized emitters, its brightest pixel being fainter only by a factor of 2 at NA of 0.9, which is also consistent with the growth of the ratio shown in Fig. 2.7 with increasing NA.

These differences can be greatly exaggerated by means of a linear polarization analysis of the PSF signals, as achieved mathematically by varying the relative strength of the parameters α and β in (2.31) that we noted earlier. Thus, for example, for the dipole in the XP state of emission the x -polarized component of the PSF signal turns out to be about 60 times as bright as its y component at the high NA of 0.9, but nearly 10^5 times as bright at the low NA of 0.2. A similar relationship holds for the YP polarized emitter when the y -polarized component of the corresponding PSF is compared to its x -polarized component. We note that while this linear dichroism between the x and y polarized components of the emitted signal is

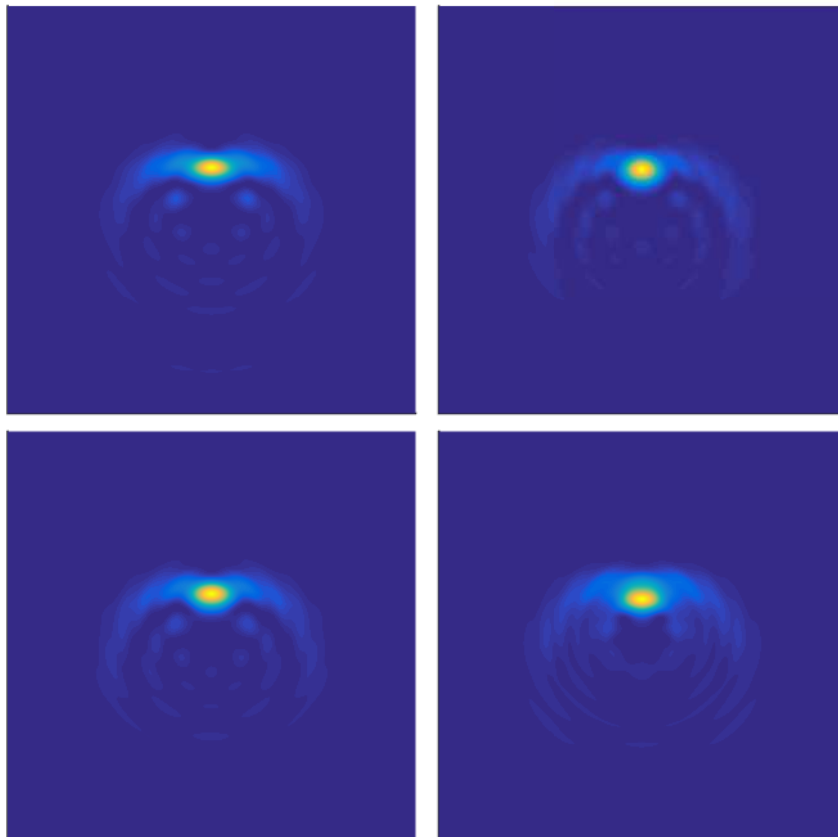


Figure 2.9: Same as Fig. 2.8, except for high NA of value 0.9. The XP, YP, and LCP emission states have PSFs with comparable brightest pixels, within 10% of one another, but which are a factor of 2 brighter than for the ZP emission state. This phenomenon also agrees well with the growing ratio plotted in Fig. 2.7. Image taken from Ref. [29].

ameliorated by increase of the NA, it is still substantial even at the highest geometric NA values in a practical microscope, and thus can be exploited at arbitrary NA values to distinguish between linear polarization states. At the high NA value of 0.9, such analysis, as we shall presently show via the results of our simulations, can discriminate between linear and circular polarization states of emission as well, since even for emission in linear polarization oriented at 45° or 135° to the x axis, the dif-

ference in the signal strength from the case of circularly polarized emission is about 10%. All other axes of linear polarization of the emitter entail a larger difference. The longitudinal (z) component of the dipole moment is easily distinguished from its transverse components, as we noted earlier, in terms of the relative contributions to the total PSF signal power that can be separately attributed to these components.

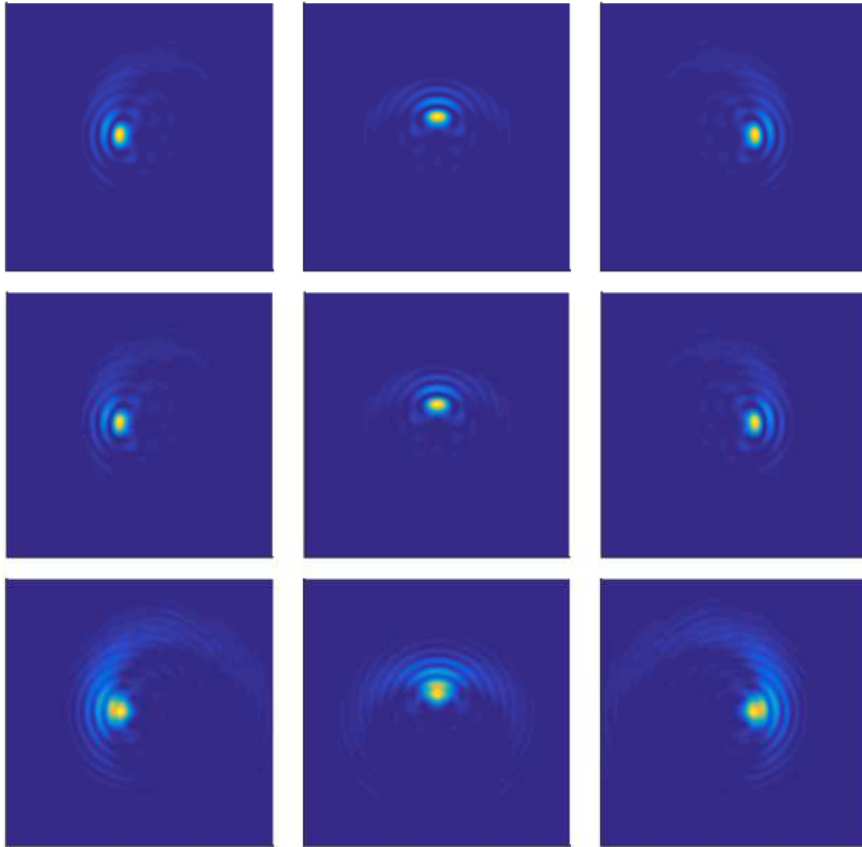


Figure 2.10: The rotating PSF signals on the sensor array for the XP (1st row); YP (2nd row); and ZP (3rd row) states of emission for the point dipole for the low-NA case, namely for $NA=0.2$. The figures in each row from left to right display the PSFs corresponding to the values -162π , 0 , and $+162\pi$ radians for the defocus parameter, $k\delta z_O$, or equivalently δz_O being -3.25 , 0 , and $+3.25$ units of the wave depth of field, λ/NA^2 , of the microscope. Image taken from Ref. [29].

In Figs. 2.10 and 2.11, we display the rotation of the PSF with changing value

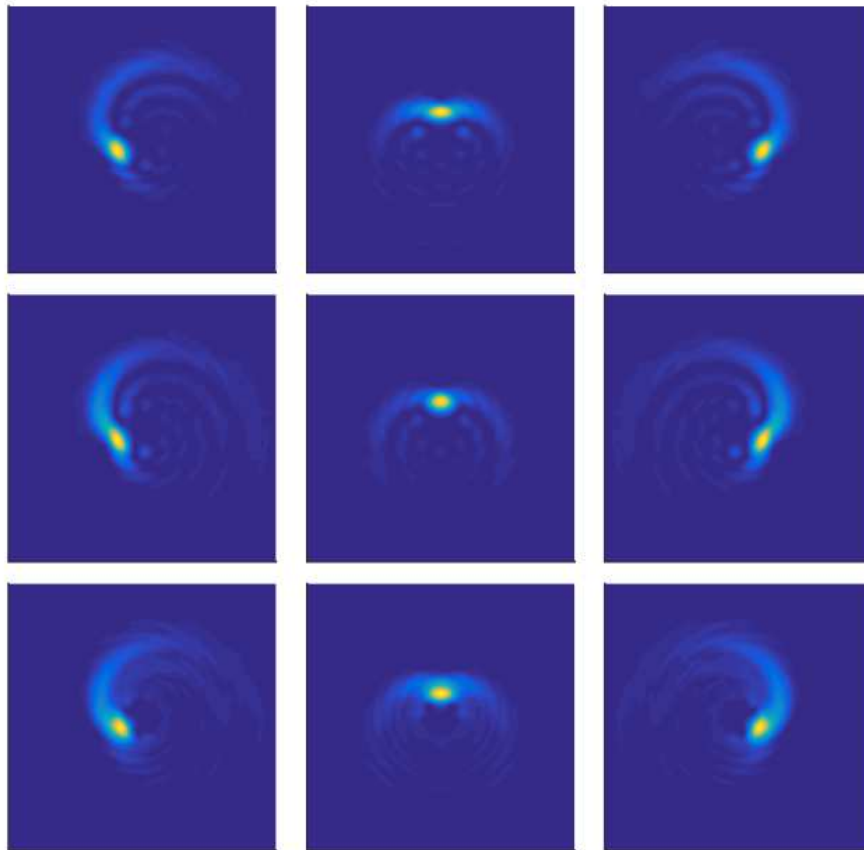


Figure 2.11: Same as Fig. 2.10, except NA is chosen to be higher at 0.9, but δz_O taking the same three values in units of λ/NA^2 as in Fig. 2.10. Image taken from Ref. [29].

of the axial-defocus parameter. The three rows of figures refer, respectively, to the cases of XP, YP, and ZP polarization states of dipole emission. The corresponding modulation transfer function (MTF) signals are shown in Figs. 2.12 and 2.13. The fact that the MTF signal fills the spatial frequency plane rather densely around dc in each case indicates excellent prospects for a rather robust recovery of source parameters, as we shall verify in the next section in our simulation-based numerical studies. Note also a definitive rotational behavior of both the PSF and MTF with changing axial depth of the emitter. However, their shape and size do change signifi-

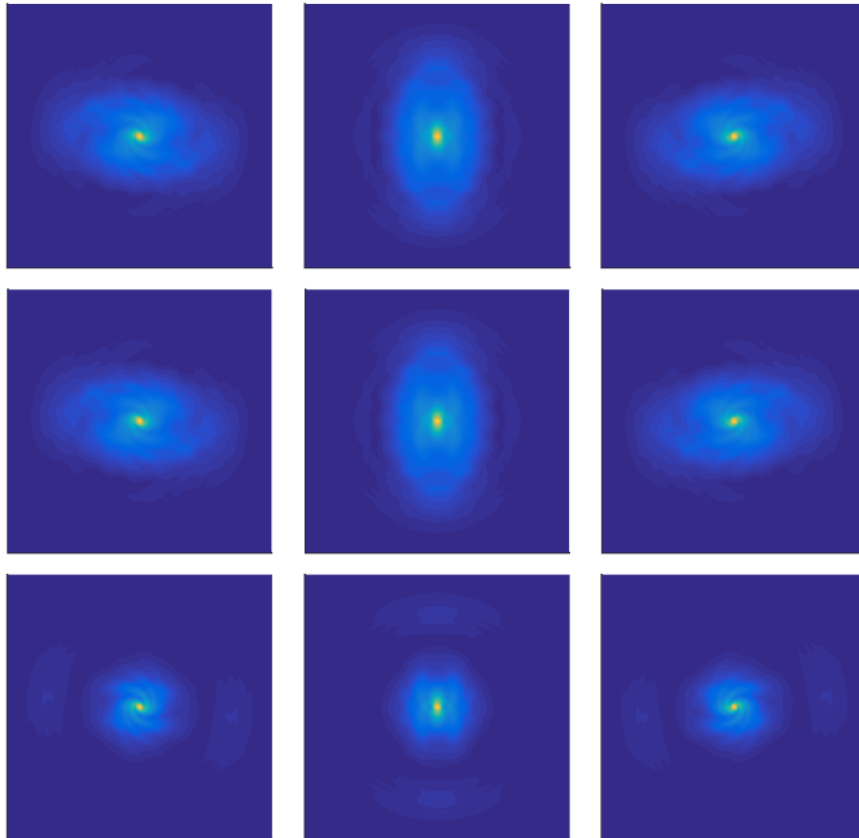


Figure 2.12: The MTF signals corresponding to the PSFs in Fig. 2.10. For the chosen parameter values, the array in each panel is the minimal square circumscribing the disk of diffraction limited bandwidth of the imager. Image taken from Ref. [29].

cantly with such rotation, particularly for the high-NA case. This is quite consistent with the discussion about the presence of a ϕ -dependent factor in the integrand that tends to undermine the rotational character of the PSF with changing axial depth and can become quite significant at large values of NA. Nevertheless, we clearly see the joint-polarimetric-localization capability of our high-NA imager.

We note importantly that regardless of the value of the NA the rotated orientation of the elliptical region surrounding the brightest pixel in the PSF contains excellent information about the 3D location of the emitter, since the rate of rota-

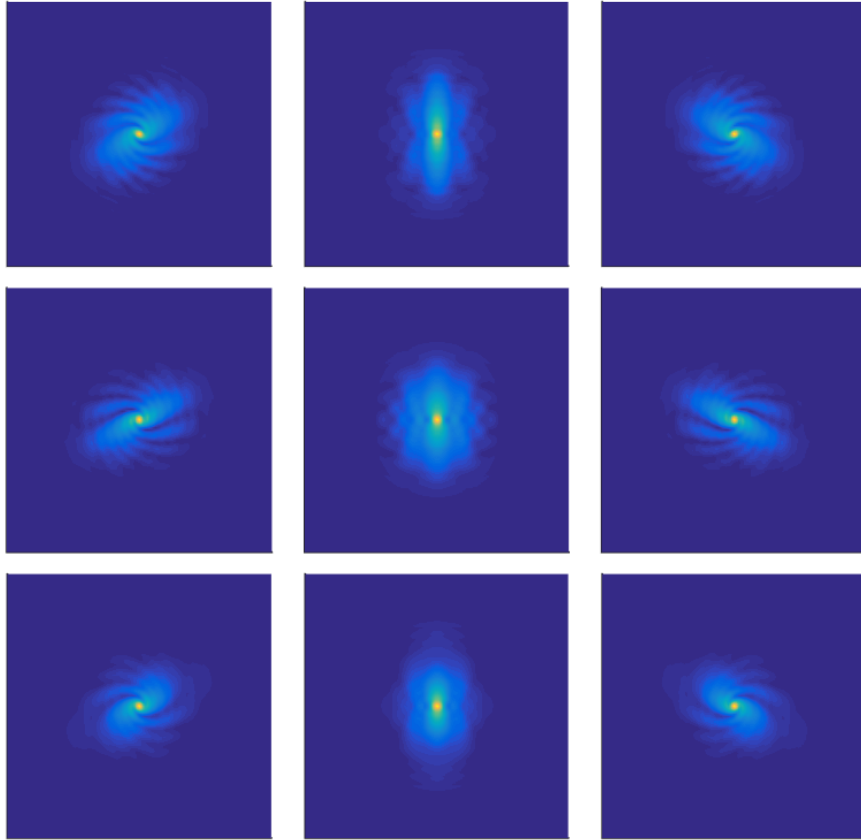


Figure 2.13: Same as Fig. 2.12, except for high NA of value 0.9. Image taken from Ref. [29].

tion of this bright elliptical lobe is uniform with defocus δz_O and roughly equal to $k(1 - \cos \theta_O)/(aL)$, according to (2.30) on which the zone-radius condition (2.27) is imposed. This implies that the elliptical lobe rotates by angle π over an axial defocus change equal to $aL/[2(1 - \cos \theta_O)]$ waves. This information can be used to obtain a starting guess for δz_O and by applying the PSF model (2.30) the corresponding transverse location, $(\delta x_O, \delta y_O)$, as we discuss in the next section where we also describe how we remove the ambiguity between the two possible values of δz_0 corresponding to any specific orientation of the elliptical lobe. The detailed spatial form and strength of the polarization-analyzed PSF signals also contain sufficiently

discriminating information about the state of 3D polarization of the emitter. In a single 2D snapshot acquired by a single sensor array, such an imager can thus perform a joint estimation of 3D locations and states of polarization of many well separated point emitters located in a 3D volume that is many waves deep even at the highest NA.

2.4.7 Simultaneous Reconstruction of Dipole Orientation and Position from Rotating PSF

We simulated image data for the case of a single dipole emitter being linearly polarized under varying values of mean total photon number under the Poisson shot-noise model valid for the rather typical EM-CCD cameras employed in the photon-counting mode by practical single-molecule imaging microscopes. The data-dependent Poisson noise is generated by using the MATLAB *poissrnd* code. All the results in this section refer to the case of the higher, experimentally more relevant geometric NA value of 0.9.

We specify the orientation of the oscillating dipole in terms of the x and y components of the unit vector along it, namely n_x and n_y , with its z component, $n_z = \sqrt{1 - n_x^2 - n_y^2}$, chosen to be non-negative to prevent physically irrelevant ambiguity in its orientation. We formulated the inverse problem of reconstructing the orientation and 3D position of the point dipole emitter from the noisy image data as a minimization problem with respect to the five parameters n_x , n_y , δx_O , δy_O , and δz_O , where δx_O , δy_O , and δz_O are the x , y , and z coordinates of the dipole position in the object space. We use maximum-likelihood estimation for photons behaving as a Poisson process, for which the cost function to be minimized is

$$C(n_x, n_y, \delta x_O, \delta y_O, \delta z_O) = \sum_{j=1}^{N_p} [\hat{I}_x(j) - I_x(j) \cdot \ln(\hat{I}_x(j)) + \hat{I}_y(j) - I_y(j) \cdot \ln(\hat{I}_y(j))] \quad (2.37)$$

where \hat{I}_x and \hat{I}_y denote 2D arrays representing the estimated spatial distributions of

the light intensity, as functions of the five parameters, at the detector in the x and y polarization channels, respectively. The corresponding noisy image data arrays for those channels are denoted by I_x and I_y .

For each set of values of the five parameters, 200 noisy data frames for each average total photon number were generated for each of the two linear polarizations into which the PSF data are analyzed. The closeness of the starting guess for the values of these parameters to their true values was particularly critical for the three location parameters, $\delta x_O, \delta y_O, \delta z_O$, to achieve a successfully convergent minimization. Two possible guesses for δz_O , as we noted earlier, are provided by the orientation of the brightest image lobe, which is the least noise affected region in the PSF data and thus most robustly characterized. The corresponding transverse location, $(\delta x_O, \delta y_O)$, for each δz_O value, was calculated from the PSF model (2.30) from which the location of the brightest pixel relative to the source location was numerically evaluated. The latter piece of information was then applied to the brightest pixel of the noisy image data, and thus the corresponding guess for the transverse source location, $(\delta x_O, \delta y_O)$, determined. The two possible values of the 3D location coordinates thus determined were subsequently substituted, one at a time, into the cost function, (2.37), and the optimization routine, for which we used the Matlab *fminunc* code, was allowed to minimize it iteratively. On convergence, the smaller of the two minimized values of the cost function was then taken to correspond to the correct estimate of the five parameters of interest. The above disambiguation process was largely insensitive to the starting guesses for the dipole orientation parameters, (n_x, n_y) , and so we set them to (0,0) at the start for each of the two minimizations. This process correctly estimated the true values of all five parameters with high precision over each of the 200 simulated noisy data frames for all the 4 mean total photon number values we used, which are 2500, 5000, 7500 and 10000.

In Fig. 2.14 we plot the standard deviation of the successfully reconstructed dipole

orientation components for the XZP state ($n_x = 1/\sqrt{2}$, $n_y = 0$, $n_z = 1/\sqrt{2}$), while δx_O and δy_O were both fixed at 0, and the axial displacement, δz_O , was changed from -4λ to 0 to $+4\lambda$, corresponding to $k\delta z_O$ changing from -8π to 0 to $+8\pi$ radians. For NA=0.9, these extremal displacements at the boundaries of the defocus range are, respectively, -3.25 and +3.25 units of the characteristic DOF, λ/NA^2 , of an ideal microscope. We note that the orientation of the emitting dipole is best determined when it is “in focus,” with the error being less than a tenth of a degree, but even for $\pm 4\lambda$ of axial defocus, the error is still acceptably small. Similar results were obtained for other emitter polarizations as well.

In Figs. 2.15-2.17, we plot the standard deviation of each of the three coordinates of the successfully recovered 3D location of the dipole emitter for three different cases of the dipole orientations, namely along the x , y , and z axes, respectively. Each of these figures has nine subplots, corresponding to the three coordinates and three different values of axial defocus, namely -4λ , 0, and $+4\lambda$. The emitter is located at the image center, $\delta x_O = \delta y_O = 0$, in the transverse plane at each value of the axial defocus. For purposes of illustration, λ was chosen to be 550 nm for these plots. We note that the transverse coordinates are always better determined than the axial coordinate, with the standard deviation of the values of the recovered coordinates being essentially independent of the state of the emitter polarization. In principle, transverse localization errors no larger than a few nm are possible, with the axial localization being a factor of 2-3 worse.

2.5 Conclusions

In this chapter we have provided a fully vectorial electromagnetic model of the rotating PSF image of a single molecule point dipole emitter formed by a microscope of arbitrary NA with a generalized version of the original spiral phase mask. Our

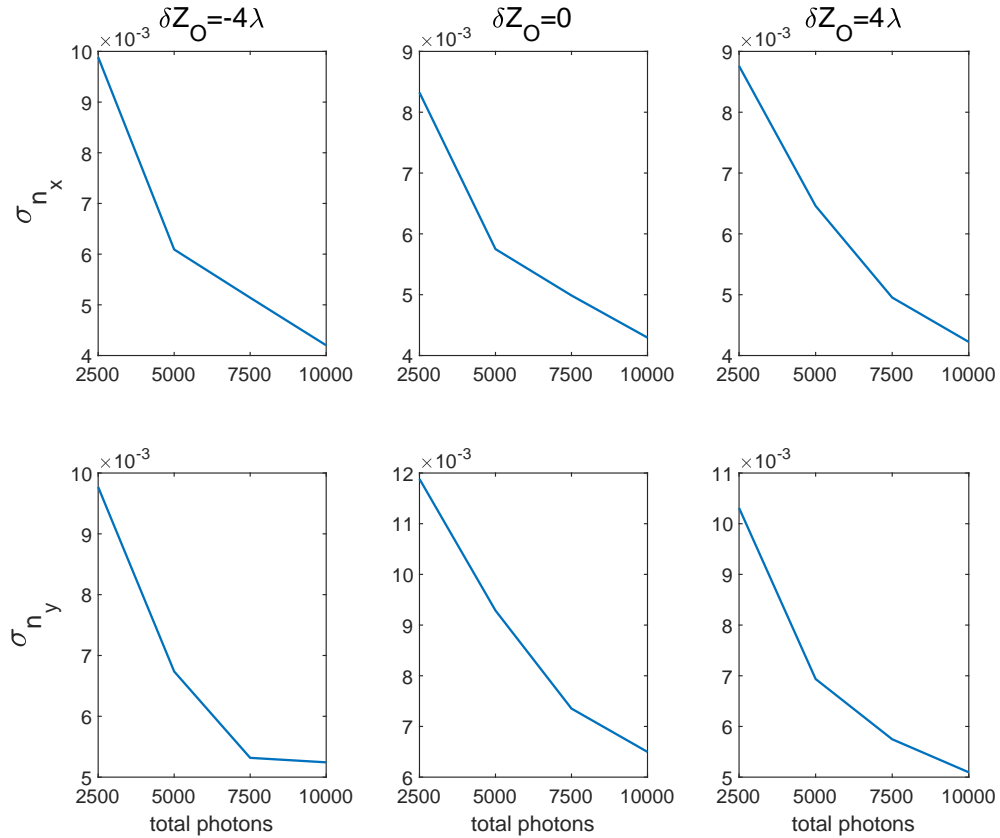


Figure 2.14: Standard deviation of the estimated n_x and n_y vs average total photon number for XZP state of the dipole source fixed at the center of the object plane and δz_O changed from -4λ (1st column) to 0 (2nd column) to 4λ (3rd column). The value of NA was chosen to be 0.9 here corresponding to $R/z_O = 2.06$ with $n_O = 1$.

analysis is justified in the usually applicable limit of optical components and propagation path lengths being large when compared to the imaging wavelength. In the limit of low NA, the model reduces to the scalar-field version of the rotating PSF. For high NA, the shape of our PSF becomes sensitively dependent on the state of source polarization, and the brightest region of the PSF can still rigidly rotate as a function of the axial position of the source. We have analyzed the polarization dependent rotating image in two orthogonal linear polarization channels, and discussed how

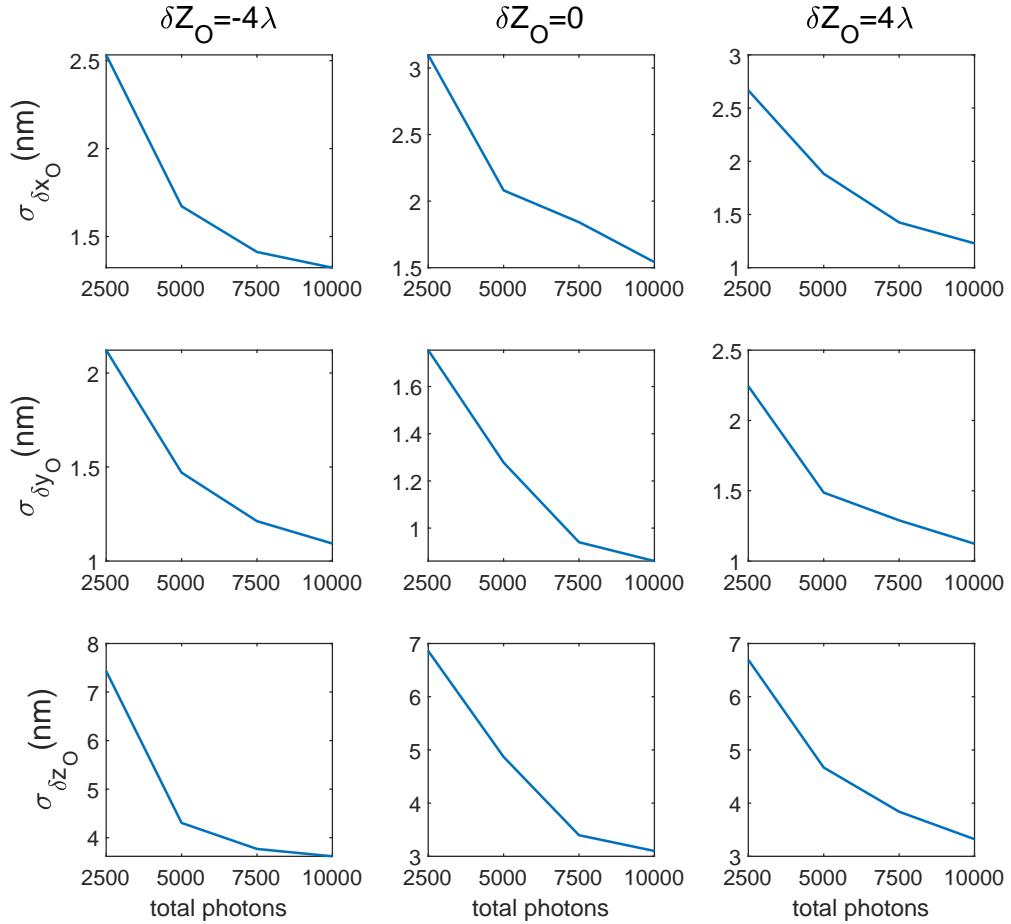


Figure 2.15: Standard deviation of the estimated δx_O , δy_O and δz_O (top to bottom) vs average total photon number for (left to right) $\delta z_O = -4\lambda$, 0 , and $+4\lambda$ for the x polarized state of emission, with $\lambda = 550 \text{ nm}$ and $\text{NA}=0.9$.

such polarization analysis can extract more detailed information about the dipole orientation. Numerical simulations have confirmed that the 3D position and orientation of the point dipole emitter can be robustly recovered using maximum-likelihood estimation.

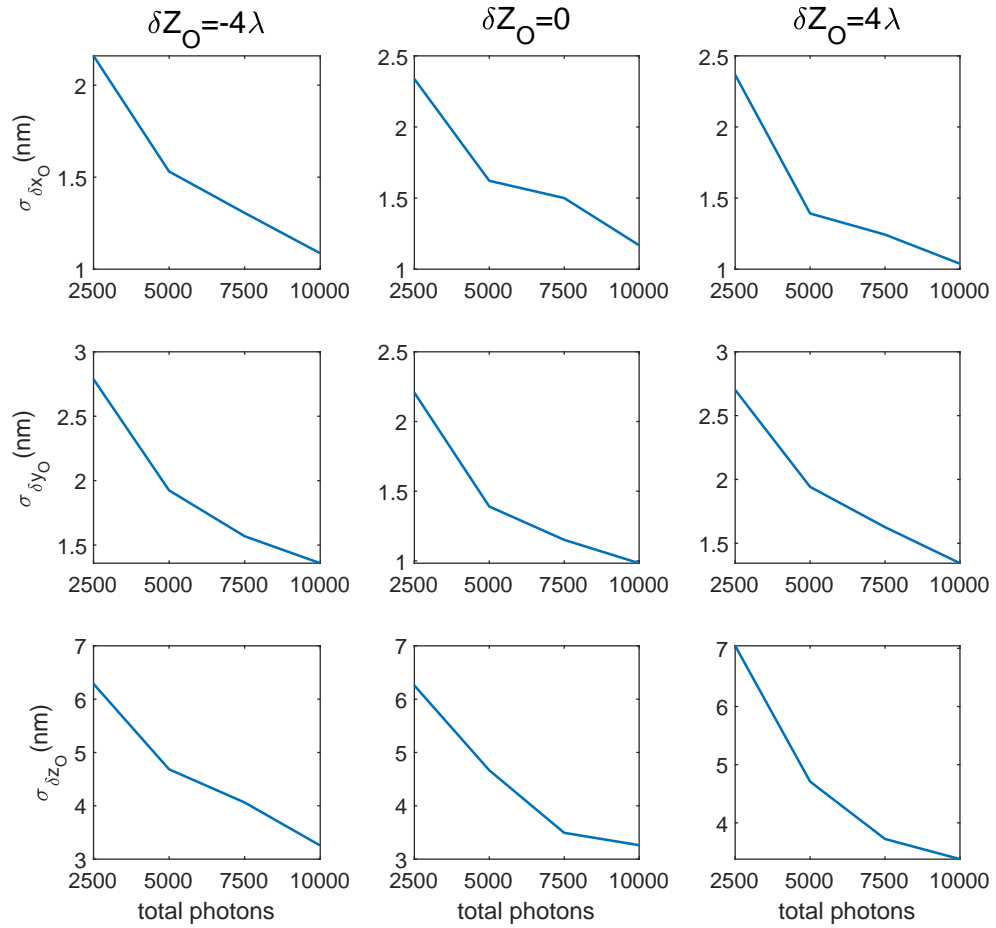


Figure 2.16: Same as Fig. 2.15 except for the y polarized state of dipole emission.

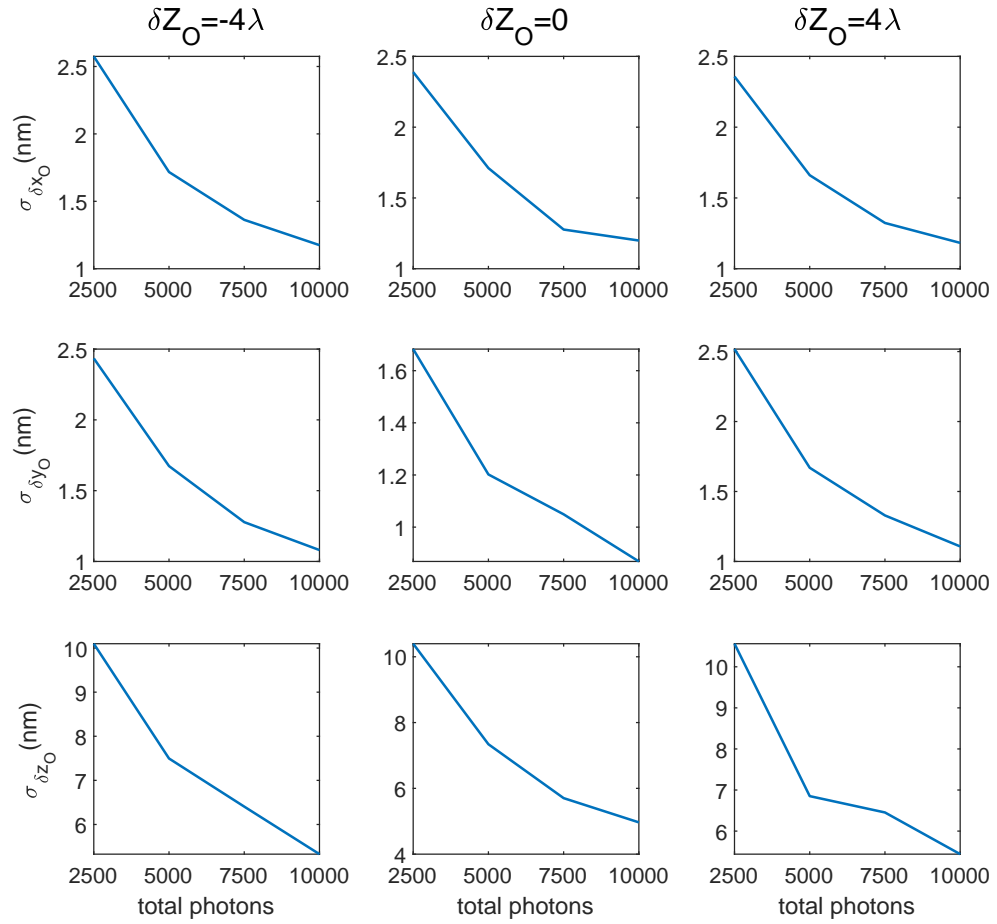


Figure 2.17: Same as Fig. 2.15 except for the z polarized state of dipole emission.

References

- [1] S. Prasad, “Rotating point spread function via pupil-phase engineering,” *Opt. Lett.* **38**, 585-587 (2013).
- [2] R. Piestun, Y. Y. Schechner, and J. Shamir, “Propagation-invariant wave fields with finite energy,” *J. Opt. Soc. Am. A* **17**, 294-303 (2000).
- [3] Y. Y. Schechner, R. Piestun and J. Shamir, “Wave propagation with rotating intensity distributions,” *Phys. Rev. E* **54**, R50 (1996).
- [4] S. Pavani and R. Piestun, “High-efficiency rotating point spread functions,” *Opt. Express* **16**, 3484-3489 (2008).
- [5] M. Lew, S. Lee, M. Badieirostami, and W. E. Moerner, “Corkscrew point spread function for far-field three-dimensional nanoscale localization of point objects,” *Opt. Lett.* **36**, 202-204 (2011).
- [6] J. Durnin, J. J. Miceli, Jr., and J. H. Eberly, “Diffraction-free beams,” *Phys. Rev. Lett.* **58**, 1499 (1987).
- [7] J. Durnin, “Exact solutions for nondiffracting beams. I. The scalar theory,” *J. Opt. Soc. Am. A* **4**, 651-654 (1987).
- [8] A. Vasara, J. Turunen, and A. T. Friberg, “Realization of general nondiffracting beams with computer-generated holograms,” *J. Opt. Soc. Am. A* **6**, 1748-1754 (1989).
- [9] G. Grover, K. DeLuca, S. Quirin, J. DeLuca, and R. Piestun, “Super-resolution photon-efficient imaging by nanometric double-helix point spread function localization of emitters (SPINDLE),” *Opt. Express* **20**, 26681-26695 (2012).
- [10] R. Kumar, “Three-Dimensional Imaging using a Novel Rotating Point Spread Function Imager,” Doctoral dissertation, The University of New Mexico, Albuquerque, NM (2015).

References

- [11] R. Kumar and S. Prasad, "PSF rotation with changing defocus and applications to 3D imaging for space situational awareness," AMOS Technical paper (2013).
[http : //www.amostech.com/TechnicalPapers/2013.cfm](http://www.amostech.com/TechnicalPapers/2013.cfm)
- [12] E. Wolf, "Electromagnetic diffraction in optical systems I. An integral representation of the image field," Proc. Royal Soc. London A **253**, 349-357 (1959).
- [13] B. Richards and E. Wolf, "Electromagnetic diffraction in optical systems II. Structure of the image field in aplanatic systems," Proc. Royal Soc. London A **253**, 358-379 (1959).
- [14] D. Flagello, T. Milster, and A. Rosenbluth, "Theory of high-NA imaging in homogeneous thin films," J. Opt. Soc. Am. A **13**, 53-64 (1996).
- [15] K. Youngworth and T. Brown, "Focusing of high numerical aperture cylindrical vector beams," Opt. Express **17**, 77-87 (2000).
- [16] J. Braat, P. Dirksen, A. Janssen, and A. van de Nes, "Extended Nijboer-Zernike representation of the vector field in the focal region of an aberrated high-aperture optical system," J. Opt. Soc. Am. A **20**, 2281-2292 (2003).
- [17] A. Asatryan, C. Sheppard, and C. de Sterke, "Vector treatment of second-harmonic generation produced by tightly focused vignetted Gaussian beams," J. Opt. Soc. Am. A **21**, 2206-2212 (2004).
- [18] T. Ha, T. A. Laurence, D. S. Chemla, S. Weiss, "Polarization spectroscopy of single fluorescent molecules," J. Phys. Chem. B **103**, 6839-6850 (1999).
- [19] E. J. Peterman, H. Sosa, and W. E. Moerner, "Single-molecule fluorescence spectroscopy and microscopy of biomolecular motors," Annu. Rev. Phys. Chem. **55**, 79-96 (2004).
- [20] M. Bohmer and J. Enderlein, "Orientation imaging of single molecules by wide-field epifluorescence microscopy," J. Opt. Soc. Am. B **20**, 554-559 (2003).
- [21] J. Enderlein, E. Toprak, and P. R. Selvin, "Polarization effect on position accuracy of fluorophore localization," Opt. Express **14**, 8111-8120 (2006).
- [22] D. Patra, H. Gregor and J. Enderlein, "Image analysis of defocused single-molecule images for three-dimensional molecule orientation studies," J. Phys. Chem. A **108**, 6836-6841 (2004).
- [23] M. A. Lieb, J. M. Zavislan and L. Novotny, "Single-molecule orientations determined by direct emission pattern imaging," J. Opt. Soc. Am. B **21**, 1210-1215 (2004).

References

- [24] B. Sick, B. Hecht and L. Novotny, “Orientational imaging of single molecules by annular illumination,” *Phys. Rev. Lett.* **85**, 4482-4485 (2000).
- [25] E. Toprak, J. Enderlein, S. Syed, S. A. McKinney, R. G. Petschek, T. Ha, Y. E. Goldman and P. R. Selvin, “Defocused orientation and position imaging (DOPI) of myosin V,” *Proc. Natl. Acad. Sci. U. S. A.* **103**, 6495-6499 (2006).
- [26] A. S. Backer and W. E. Moerner, “Extending single-molecule microscopy using optical Fourier processing,” *J. Phys. Chem. B* **118**, 8313-8329 (2014).
- [27] A. S. Backer, M. P. Backlund, A. R. von Diezmann, S. J. Sahl and W. E. Moerner, “A bisected pupil for studying single-molecule orientational dynamics and its application to three-dimensional super-resolution microscopy,” *Appl. Phys. Lett.* **104**, 193701-193701-5 (2014).
- [28] X. Huang, I. El-Sayed, W. Qian, and M. El-Sayed. “Cancer cells assemble and align gold nanorods conjugated to antibodies to produce highly enhanced, sharp, and polarized surface Raman spectra: A potential cancer diagnostic marker,” *Nano Lett.* **7**, 1591-1597 (2007).
- [29] Z. Yu and S. Prasad, “High-numerical-aperture microscopy with a rotating point spread function,” *J. Opt. Soc. Am. A* **33**, B58-B69 (2016).
- [30] J. Jackson, *Classical Electrodynamics*, 2nd edition (Wiley, 1999).
- [31] M. Mansuripur, “Distribution of light at and near the focus of high-numerical-aperture objectives,” *J. Opt. Soc. Am. A* **3**, 2086-2093 (1986).
- [32] J. Enderlein, E. Toprak, and P. Selvin, “Polarization effects on position accuracy of fluorophore localization,” *Opt. Express* **14**, 8111-8120 (2006).
- [33] J. Goodman, *Introduction to Fourier Optics*, 3rd edition (Roberts, 2005), Chap. 3.
- [34] This is consistent with the fact that rays emerge from the objective parallel to the optical axis and are then focused by a tube lens with a focal length typically 10-20 larger than that of the objective.
- [35] G. Golub and C. Van Loan, *Matrix Computations*, 3rd edition (Johns Hopkins, 1996).
- [36] V. Gruev, R. Perkins, and T. York, “CCD polarization imaging sensor with aluminum nanowire optical filters,” *Opt. Express* **18**, 19087-19094 (2010).

References

- [37] K. Sasagawa, S. Shishido, K. Ando, H. Matsuoka, T. Noda, T. Tokuda, K. Kakiuchi, and J. Ohta, “Image sensor pixel with on-chip high extinction ratio polarizer based on 65-nm standard CMOS technology aluminum nanowire optical filters,” *Opt. Express* **21**, 11132-11140 (2013).

Chapter 3

3D Polarimetric Imaging via SAM-OAM Conversion

3.1 Introduction

We propose in this Chapter a new polarimetric imaging protocol based on the conversion of the wave polarization, which at the most elementary level represents the state of the spin angular momentum (SAM) of any photon in the wave, to a corresponding orbital angular momentum (OAM) state [1]. The so-modified source radiation will then be passed into a spiral phase mask (SPM) to perform full 3D polarimetric imaging. Unlike the high NA imaging approach developed in the previous chapter, this new approach does not depend on the NA of the imager being large, since it does not use the large obliquity of rays to create a dependence of the imaging beam on the nature of polarization of the dipole emitter. It therefore can be also applied to telescope imaging. We shall illustrate this approach for the simple case of paraxial imaging, $NA \ll 1$, obviating any complications of a vector-field treatment.

3.2 The Basic Concept of q-plate Technology

Since SAM is associated with optical polarization and OAM with the optical wavefront, at first sight they appear to be quite independent, non-interacting properties of light, at least in the paraxial limit. For this reason, for about ten years after the publication of the seminal paper by Allen et al [2], which started the current field of research in the optical OAM, the possibility of an interaction between SAM and internal OAM taking place in a single paraxial optical beam was not considered. The generation and control of optical OAM has been based only on essentially polarization-independent tools, such as cylindrical lenses [2], spiral phase plates [3], holograms [4, 5] and certain optical elements in suitable interferometric setups [6, 7].

In 2006, Marrucci *et al.* [8] proposed that anisotropic inhomogeneous media such as liquid crystals (LC) could give rise to a previously unrecognized optical process in which the interaction of SAM of light with the medium's birefringence gives rise to the appearance of OAM, arising from the medium's inhomogeneity. In rotationally symmetric geometries, this process involves no net transfer of angular momentum to matter, so that the SAM of the photon is entirely converted into its OAM. For this reason, the process was dubbed spin-to-orbital conversion of angular momentum, and the first LC-based device achieving this conversion was named q-plate [8, 9]. This exciting invention has been attracting increasing attention and given rise in recent years to a number of new results and to significant progress [10] in the field of orbital angular momentum of light. Particularly promising are quantum photonic applications, because the polarization control of OAM allows the transfer of quantum information from the SAM qubit subspace to the OAM subspace of the photon and vice versa.

The q-plate is a patterned birefringent half-wave plate with the orientation of its local optical axis changing as a function of the azimuthal angle coordinate ϕ in the

plate plane by the linear relation

$$\alpha(u, \phi) = q\phi + \alpha_0, \quad (3.1)$$

where q is required, for periodicity (single-valuedness) of the optical axis, to be either half-integral or integral.

The q-plate transforms the column vector $(E_x, E_y)^T$ of the x and y components of the electric field of radiation locally by the following Jones matrix

$$\mathbf{Q} = \mathbf{R}(-\alpha)\mathbf{W}\mathbf{R}(\alpha), \quad (3.2)$$

where the form of \mathbf{Q} can be interpreted as a rotation to the local birefringent axes followed by the relative phase shift and the inverse rotation to the original axes, $\mathbf{R}(\alpha)$ is the usual 2D rotation matrix,

$$\mathbf{R}(\alpha) = \begin{pmatrix} \cos \alpha & \sin \alpha \\ -\sin \alpha & \cos \alpha \end{pmatrix}, \quad (3.3)$$

and \mathbf{W} denotes the phase retardation matrix of a half-wave plate,

$$\mathbf{W} = \begin{pmatrix} 1 & 0 \\ 0 & -1 \end{pmatrix}. \quad (3.4)$$

Performing the simple matrix product in (3.2) yields the following result:

$$\mathbf{Q} = \begin{pmatrix} \cos 2\alpha & \sin 2\alpha \\ \sin 2\alpha & -\cos 2\alpha \end{pmatrix}. \quad (3.5)$$

Under the Jones matrix (3.5), the x , y -component column vectors, $(1 \pm i)^T$, corresponding to the two circularly polarized waves are transformed as follows:

$$\begin{pmatrix} 1 \\ \pm i \end{pmatrix} \longrightarrow e^{\pm i2\alpha} \begin{pmatrix} 1 \\ \mp i \end{pmatrix} = e^{\pm i2q\phi} e^{\pm i2\alpha_0} \begin{pmatrix} 1 \\ \mp i \end{pmatrix}.$$

The wave undergoes a perfect flip of its helicity and a OAM vorticity change by amount $\pm 2q$. A few examples of q-plate geometries for different values of q and α_0 are shown in Fig. 3.1. The last two cases correspond to rotationally symmetric plates, giving rise to perfect spin-to-orbital angular momentum conversion, with no angular momentum transfer to the plate. But in the non-rotationally-symmetric case (a), the material undergoes an angular momentum change of ± 1 unit of \hbar . In the rest of this Chapter, we shall, for definiteness, use the q-plate with $q = 1$ and $\alpha_0 = 0$.

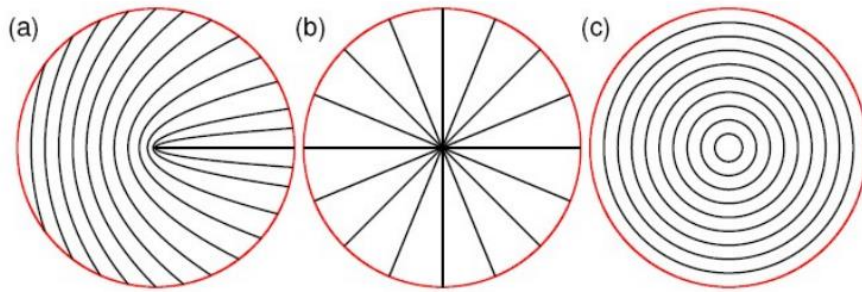


Figure 3.1: Examples of q-plates. The tangent to the lines shown indicate the local direction of the optical axis. (a) $q = 1/2$, $\alpha_0 = 0$; (b) $q = 1$, $\alpha_0 = 0$; (c) $q = 1$, $\alpha_0 = \pi/2$. Image taken from Ref. [8].

3.3 Improved 3D Polarimetric Imaging via SAM-OAM Conversion

For the purposes of illustration, consider the problem of imaging a point dipole emitter that is transversely polarized orthogonal to the z axis expressed as

$$\vec{p} = p_x \hat{x} + p_y \hat{y} = p_+ \hat{e}_+ + p_- \hat{e}_-, \quad (3.6)$$

with $p_{\pm} = \frac{1}{\sqrt{2}}(p_x \mp ip_y)$, where $\hat{e}_{\pm} = (\hat{x} \pm i\hat{y})/\sqrt{2}$ are the circular-polarization (CP) unit basis vectors. Here we define the four Stokes parameters of emission, up to an

Chapter 3. 3D Polarimetric Imaging via SAM-OAM Conversion

overall common factor, as

$$\begin{aligned}
 s_0 &= \langle |p_x|^2 \rangle + \langle |p_y|^2 \rangle = \langle |p_+|^2 \rangle + \langle |p_-|^2 \rangle; \\
 s_1 &= \langle |p_x|^2 \rangle - \langle |p_y|^2 \rangle = 2\text{Re}\langle p_+^* p_- \rangle; \\
 s_2 &= 2\text{Re}\langle p_x^* p_y \rangle = 2\text{Im}\langle p_+^* p_- \rangle; \text{ and} \\
 s_3 &= 2\text{Im}\langle p_x^* p_y \rangle = \langle |p_+|^2 \rangle - \langle |p_-|^2 \rangle.
 \end{aligned} \tag{3.7}$$

In the limit of low NA, the total image-plane electric field, \vec{E}_I , for the imaging system in the previous chapter reduces to the form

$$\vec{E}_I = E_{Ix}\hat{x} + E_{Iy}\hat{y} \sim \int d^2u P(Ru) \exp[-i2\pi\vec{u}\cdot\vec{s}_I + i\Psi(u, \phi) + i\frac{\pi R^2 \delta z_O}{\lambda z_O^2}](p_x\hat{x} + p_y\hat{y}), \tag{3.8}$$

where $E_{Ix(y)}$ is the $x(y)$ component of the total image plane electric field \vec{E}_I . The expected image intensity $I_{x(y)}$ in the $x(y)$ polarization channel has the simple form

$$I_{x(y)} \sim \langle |E_{Ix(y)}|^2 \rangle. \tag{3.9}$$

By means of a polarization analysis, we are able to extract $|p_x|$ and $|p_y|$ separately, but the image plane intensity is insensitive to the relative phase difference between p_x and p_y , which means in the low NA limit s_2 and s_3 are unable to be encoded in our previous SPM-based imaging system even when there is linear polarization analysis.

We next discuss the image field modification created by a q-plate with $q = 1$ and $\alpha_0 = 0$, for which the Jones calculus w.r.t. the elementary pure-helicity states \hat{e}_\pm yields

$$\hat{e}_\pm \longrightarrow e^{\pm i2\phi} \hat{e}_\mp. \tag{3.10}$$

Chapter 3. 3D Polarimetric Imaging via SAM-OAM Conversion

Under the transformation law (3.10) of the q-plate, which is placed in a plane conjugate to the exit pupil of the imager, the final expression for the image-plane electric field has the form

$$\begin{aligned}
 \vec{E}_I(\vec{r}_I) &\sim \int d^2u P(Ru) \exp[-i 2\pi\vec{u} \cdot \vec{s}_I + i\psi(u, \phi) + i\frac{\pi R^2 \delta z_O}{\lambda z_O^2}] \\
 &\quad \times (p_- e^{-i2\phi_u} \hat{e}_+ + p_+ e^{+i2\phi_u} \hat{e}_-) \\
 &= \int d^2u P(Ru) \exp[-i 2\pi\vec{u} \cdot \vec{s}_I + i\psi(u, \phi) + i\frac{\pi R^2 \delta z_O}{\lambda z_O^2}] \\
 &\quad \times \frac{1}{\sqrt{2}} [(p_+ e^{+i2\phi_u} + p_- e^{-i2\phi_u}) \hat{x} - i(p_+ e^{+i2\phi_u} - p_- e^{-i2\phi_u}) \hat{y}]. \tag{3.11}
 \end{aligned}$$

Substituting (3.11) into (3.9) and using (3.7) for the Stokes parameters, we have I_x and I_y as

$$I_x \sim \frac{|a_+|^2 + |a_-|^2}{2} s_0 - \frac{|a_+|^2 - |a_-|^2}{2} s_3 + \text{Re}(a_+^* a_-) s_1 - \text{Im}(a_+^* a_-) s_2, \tag{3.12}$$

$$I_y \sim \frac{|a_+|^2 + |a_-|^2}{2} s_0 - \frac{|a_+|^2 - |a_-|^2}{2} s_3 - \text{Re}(a_+^* a_-) s_1 + \text{Im}(a_+^* a_-) s_2, \tag{3.13}$$

where a_{\pm} are defined as the integrals

$$a_{\pm} = \int d^2u P(Ru) \exp[-i 2\pi\vec{u} \cdot \vec{s}_I + i\psi(u, \phi) \pm i2\phi + i\frac{\pi R^2 \delta z_O}{\lambda z_O^2}]. \tag{3.14}$$

We see I_x and I_y can now encode all the 4 Stokes parameters. However, the total image intensity $I = I_x + I_y$ has the form,

$$I \sim (|a_+|^2 + |a_-|^2) s_0 - (|a_+|^2 - |a_-|^2) s_3, \tag{3.15}$$

which can still encode s_3 because of the q-plate, but has no sensitivity to s_1 and s_2 , thus the polarization analysis is still needed to fully encode the Stokes vector.

In Fig. 3.3, we display from top to bottom the PSF signal corresponding to the point dipole with $\delta z_O = 0$ emitting in x-linearly polarized (XLP), y-linearly polarized (YLP), 45°-linearly polarized (45LP), 135°-linearly polarized (135LP), left circularly polarized (LCP), and right circularly polarized (RCP) states. The figures in each row

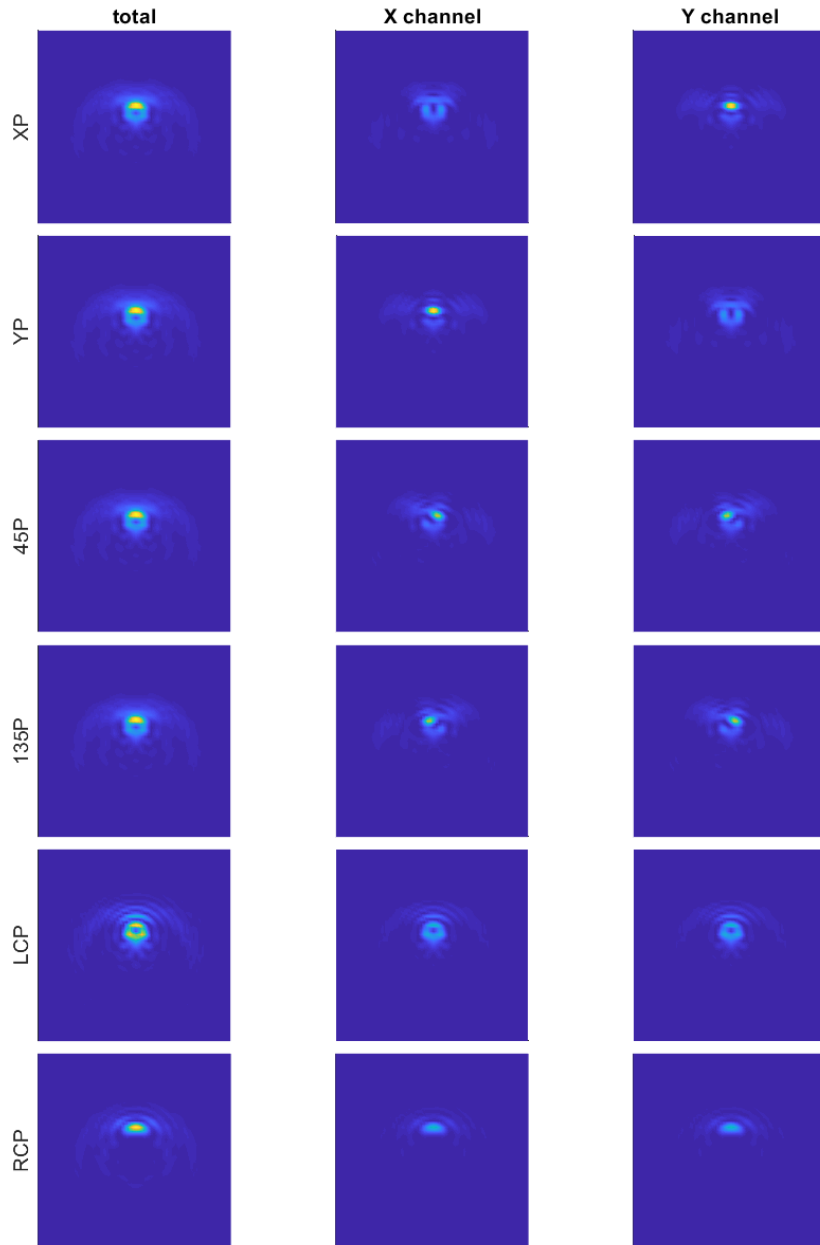


Figure 3.2: The total PSF signal (1st column), PSF signal in x polarization channel (2nd column) and y polarization channel (3rd column) for the point dipole emitter located in the plane of Gaussian focus in XLP, YLP, 45LP, 135LP, LCP and RCP states (from top to bottom).

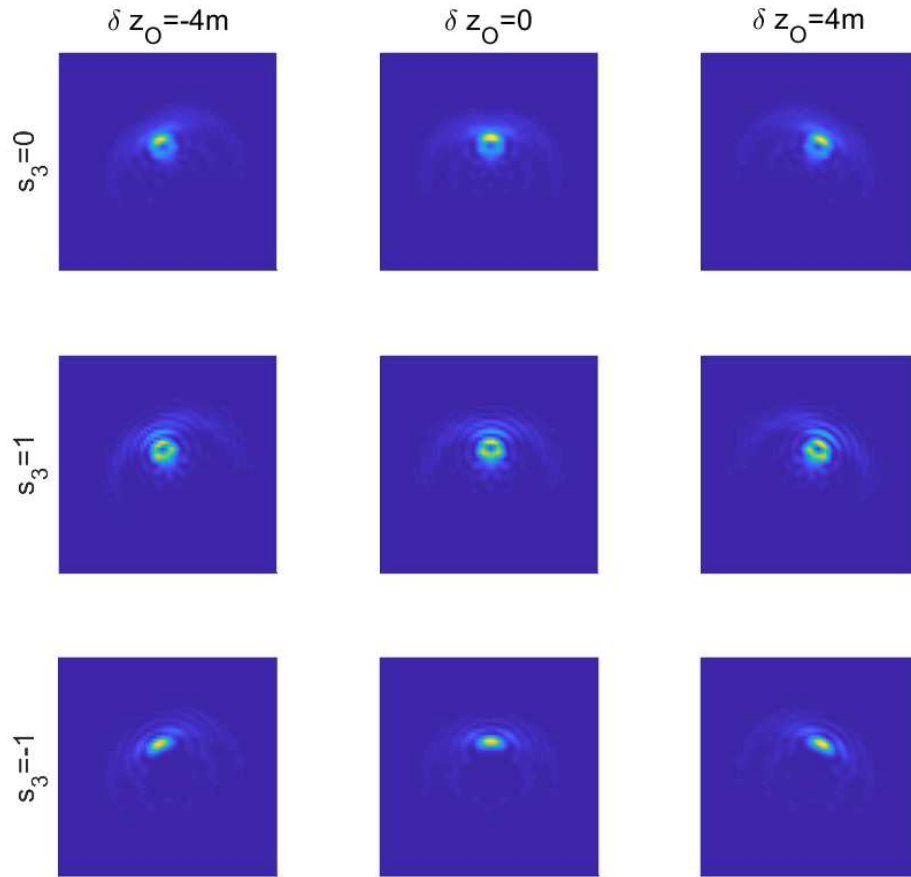


Figure 3.3: The total rotating PSF signals for emission of the point dipole with $s_3 = 0$ (1st row); $s_3 = 1$ (2nd row); and $s_3 = -1$ (3rd row). s_0 is fixed to be 1. The figures in each row from left to right display the PSFs corresponding to the values -4m , 0 , and 4m for δz_O . We choose $\lambda = 1\mu\text{m}$, $R=0.5\text{ m}$, $z_O = 1000\text{m}$.

from left to right display the spatial distribution of the total image intensity, and the image intensities in the x polarization and y polarization channels. We see that the total image intensities for emission states with different s_3 are obviously different, the total image intensities for the 4 linearly polarized emissions with $s_3 = 0$ are the same, but the signals in the two polarization channels can disambiguate the 4 states

very well.

In Fig. 3.4, we display the rotation of the total PSF for changing value of δz_O . The three rows of figures refer, respectively, to the cases of $s_3 = 0, 1$, and -1 . For purposes of illustration, we choose $\lambda = 1\mu m$, $R = 0.5m$, and $z_O = 1000m$ for the rest of this chapter.

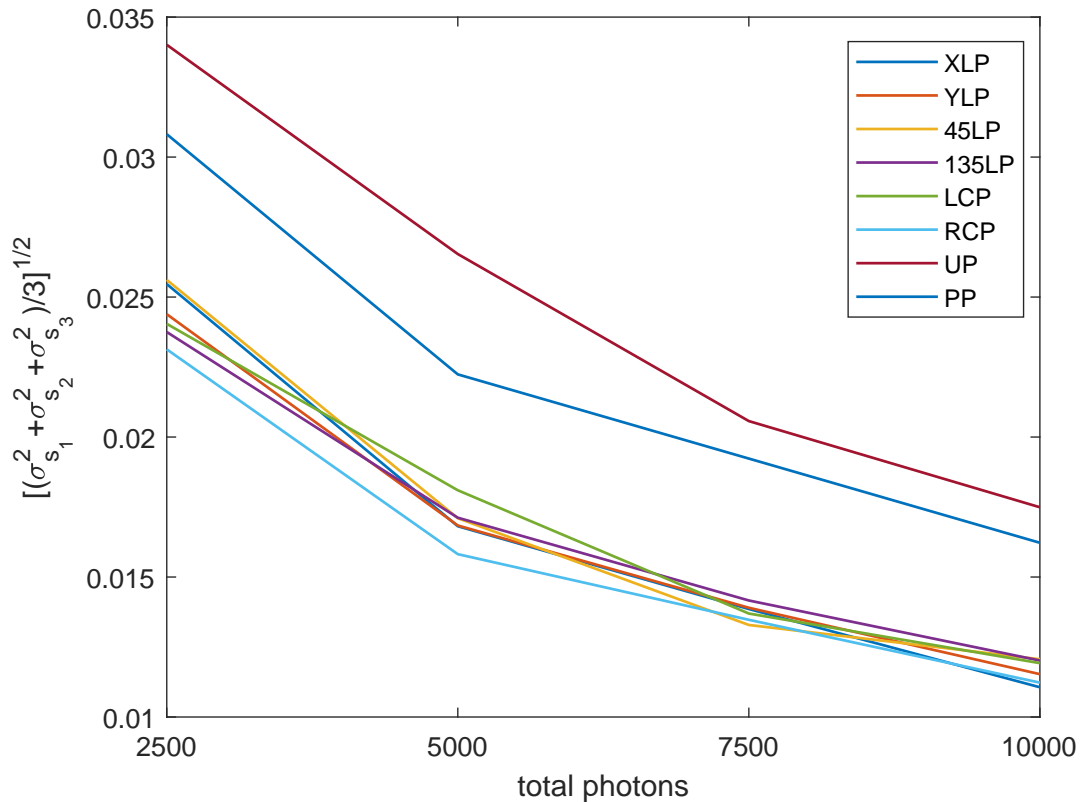


Figure 3.4: The square root of the average variance of the reconstructed Stokes parameters vs average total photon number for dipole at $\delta z_O = 0$ emitting in XLP, YLP, 45LP, 135LP, LCP, RCP, UP and PP (1, 0.5, 0.4, 0.3) states.

We formulated the inverse problem of simultaneously reconstructing the normalized Stokes vector (s_0 fixed at 1) and the 3D location of the point dipole from the noisy image data under the Poisson shot-noise model as a minimization problem with

respect to the 6 parameters, s_1 , s_2 , s_3 , δx_O , δy_O , and δz_O . The maximum-likelihood estimation with cost function similar to Eq. (2.31) is used. For each set of values of the 6 parameters and each of the two linear polarization channels we generated 200 noisy data frames for each average total photon number.

In Fig. 3.5 we plot the square root of the average variance of the reconstructed s_1 , s_2 and s_3 for point dipole at $\delta z_O = 0$ emitting in XLP, YLP, 45LP, 135LP, LCP, RCP, unpolarized (UP) and partially polarized (PP) states (we choose $s_1 = 0.5$, $s_2 = 0.4$, $s_3 = 0.3$ for the PP state). All the emission states are reconstructed with good accuracy, but the perfectly polarized states have slightly better performances.

In Fig 3.6, we plot the standard deviation of each of the three coordinates of the recovered 3D location of the dipole emitter in XLP state. The figure has nine subplots, corresponding to the three coordinates and three different values of δz_O , namely $-4m$, 0 , and $+4m$. The emitter is located at the image center, $\delta x_O = \delta y_O = 0$, in the transverse plane at each value of the axial defocus. We see that the transverse localization errors are much smaller than the error of axial localization. This may have to do with the $1/NA$ vs $1/NA^2$ scaling of the lateral vs longitudinal localization errors, particularly at small values of NA.

3.4 Conclusions

In this chapter we have proposed a novel 3D polarimetric imaging approach that utilizes the process of SAM-OAM conversion in conjunction with the SPM-based rotating PSF idea. In the low NA limit, the q-plate-modified imaging system with separate x and y linear polarization channels can fully encode the polarization state of a transversely polarized point dipole emitter and determine its 3D location in a snapshot mode. Our approach may be extended to the 3D polarimetric imaging of multiple point sources and extended sources.

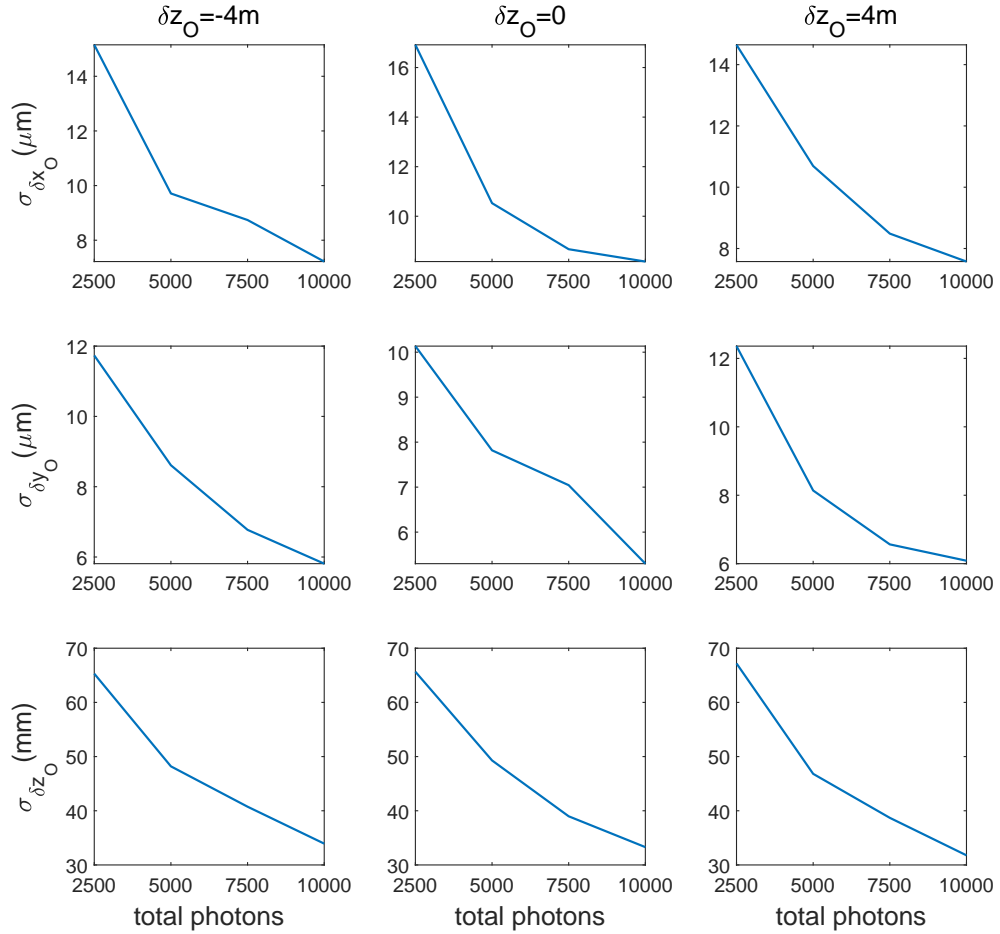


Figure 3.5: Standard deviation of the estimated δx_O , δy_O and δz_O (top to bottom) vs average total photon number for (left to right) $\delta z_O = -4m$, 0 , and $+4m$ for the x polarized state of emission, with $\lambda = 1\mu m$, $R = 0.5m$, $z_O = 1000m$.

References

- [1] K. Y. Bliokh, F. J. Rodriguez-Fortuno, F. Nori, and A. V. Zayats, “Spin-orbit interactions of light,” *Nat. Photonics* **9**, 796 (2015).
- [2] L. Allen, M. W. Beijersbergen, R. J. C. Spreeuw, and J. P. Woerdman, “Orbital angular momentum of light and the transformation of Laguerre-Gaussian laser modes,” *Phys. Rev. A* **45**, 8185-8189 (1992).
- [3] M. W. Beijersbergen, R. P. C. Coerwinkel, M. Kristensen, and J. P. Woerdman, “Helical-wavefront laser beams produced with a spiral phaseplate,” *Opt. Commun.* **112**, 321 (1994).
- [4] V. Y. Bazhenov, M. S. Soskin, and M. V. Vasnetsov, “Screw Dislocations in Light Wavefronts,” *J. Mod. Opt.* **39**, 985 (1992)
- [5] I. V. Basistiy, V. Y. Bazhenov, M. S. Soskin, and M. V. Vasnetsov, “Optics of light beams with screw dislocations,” *Opt. Commun.* **103**, 422 (1993).
- [6] J. Leach, M. J. Padgett, S. M. Barnett, S. Franke-Arnold, J. Courtial, “Measuring the orbital angular momentum of a single photon,” *Phys. Rev. Lett.* **88**, 257901 (2002).
- [7] S. Slussarenko, V. D’Ambrosio, B. Piccirillo, L. Marrucci, and E. Santamato, “The Polarizing Sagnac Interferometer: A tool for light orbital angular momentum sorting and spin-orbit photon processing,” *Opt. Express* **18**, 27205 (2010).
- [8] L. Marrucci, C. Manzo, and D. Paparo, “Optical Spin-to-Orbital Angular Momentum Conversion in Inhomogeneous Anisotropic Media,” *Phys. Rev. Lett.* **96**, 163905 (2006).
- [9] L. Marrucci, C. Manzo, D. Paparo, “Pancharatnam-Berry phase optical elements for wavefront shaping in the visible domain: switchable helical modes generation,” *Appl. Phys. Lett.* **88**, 221102 (2006).

References

- [10] Lorenzo Marrucci, Ebrahim Karimi, Sergei Slussarenko, Bruno Piccirillo, Enrico Santamato, Eleonora Nagali, and Fabio Sciarrino, “Spin-to-orbital conversion of the angular momentum of light and its classical and quantum applications,” *J. Opt.* **13**, 064001 (2011)

Chapter 4

Achieving Quantum Limited 3D Super-resolution

4.1 Introduction

Lord Rayleigh's criterion [1] for resolving a pair of incoherent point sources has been the theoretical bedrock of optical resolution since its formulation in 1879. It asserts that it is essentially impossible to distinguish two incoherent point sources, when they are separated from each other by a distance much smaller than the characteristic width of the point spread function (PSF) of the optical system. Despite its strong influence on several decades of work on the optical resolution possible in imaging systems, this intuitive criterion developed mainly for the human eye is not a fundamental limit. In the past few decades, advances in single-molecule optical super-resolution techniques have enabled scientists to sidestep Rayleigh's limit. The approach is to turn the resolution problem into one of PSF fitting and localization of single fluorophors by selective excitation in which two closeby fluorophors are not radiating at the same time. Performing PSF fittings over individual sources one frame

Chapter 4. Achieving Quantum Limited 3D Super-resolution

at a time from many such frames yield a composite superresolved image [2]-[7]. While such techniques have achieved spectacular success, they require a careful control of the emission, which is not always possible, especially for astronomical imaging.

It is also known that for two sources with overlapping radiations on the image plane, computational image processing can beat Rayleigh's criterion if sufficiently large numbers of photons illuminate the image pixels [8]-[13], but the precision deteriorates dramatically at a fixed photon number, when Rayleigh's criterion is violated. In classical estimation theory, the classical Fisher information (CFI) matrix provides the inverse of the classical Cramér-Rao bound (CCRB), which furnishes a lower bound on the variance of any unbiased estimator [14, 15]. For a given imaging system and a fixed number of collected photons, the CFI carried by the intensity distribution of the light in the image-plane falls to zero as the transverse separation between the sources becomes smaller than the Rayleigh's limit [16, 17]. This phenomenon was dubbed Rayleigh's curse by Tsang, Nair and Lu [18]. It suggests a fundamental limitation of the standard imaging protocol in resolving incoherent point sources.

Tsang *et al.* [18] also revisited the problem of resolving two identical incoherent point sources from the perspective of quantum metrology and quantum estimation theory, in which the CFI matrix can be further maximized over all possible quantum mechanically allowed measurements to yield what has been called the quantum Fisher information (QFI) matrix. The inverse of QFI [19]-[23] matrix, called the quantum Cramér-Rao bound (QCRB), provides the ultimate lower bound on the variance of an unbiased estimation of the parameters superseding, in general, that provided by the CFI matrix. The authors of Ref. [18] derived the QFI and QCRB for estimating the separation of an incoherent source-pair in one transverse dimension, which surprisingly turns out to be a finite constant independent of the separation of the sources. They also showed that this ultimate quantum limit optimized over

Chapter 4. Achieving Quantum Limited 3D Super-resolution

all possible measurements allowed by quantum mechanics, is in fact saturated by classical phase-sensitive measurements. As a consequence, Rayleigh's criterion turns out no longer to be fundamental to the problem. Its relevance arises because standard direct imaging discards all the phase information contained in the field. This ground-breaking result has been generalized and experimentally verified by a number of groups [24]-[39]. While transverse spatial resolution can be significantly enhanced by these methods, three-dimensional (3D) super-resolution of simultaneously emitting closeby sources is still a challenging task. Researchers have proposed various approaches, such as interferometric microscope [39, 40], engineered PSF [41]-[45], and multiplane imager [46, 47], to achieve 3D single point source super-localization. In spite of these advanced techniques, determining a small axial separation between two simultaneously emitting incoherent point sources is still difficult. In this Chapter we will treat the problem of estimating the full 3D separation vector for a pair of incoherent, equally bright point sources, when the pair centroid is known and an imager with a circular aperture is used. We will first calculate the 3×3 QFI matrix w.r.t. the three components of the pair separation vector, and show that it is constant and diagonal. We will also show that the pair-separation QFI is in fact identical to the source localization QFI, which underscores the fundamental importance of photon-state localization as the basis for determining the ultimate estimation-theoretic bound for both the source separation and localization problems. We will next propose specific projective-measurement protocols that can attain the corresponding QCRB in the cases of pure lateral and axial separations and in the limit of small separations. Finally we will present simulations of an experimental proposal to achieve quantum-limited 3D pair separation. The main work in this Chapter was published in Ref. [48].

4.2 QFI Matrix for 3D Pair Separation

We first set the stage for our model. When two mutually incoherent point sources with equal intensities emits a photon that is subsequently transmitted through an imaging aperture, the photon is described by the density operator

$$\hat{\rho} = \frac{1}{2} (|K_+\rangle\langle K_+| + |K_-\rangle\langle K_-|), \quad (4.1)$$

in which $|K_{\pm}\rangle$ are pure one-photon states passing through the aperture, corresponding to individual emissions by the two sources located at 3D positions, $\pm(\mathbf{r}_{\perp}, r_z)$.

The corresponding dimensionless transverse and axial semi-separations, \mathbf{l}_{\perp} and l_z , are related to \mathbf{r}_{\perp} and r_z as

$$\mathbf{l}_{\perp} = \mathbf{r}_{\perp}/\sigma_0, \quad l_z = r_z/\zeta_0, \quad (4.2)$$

where $\sigma_0 = \lambda z_O/R$ and $\zeta_0 = \lambda z_O^2/R^2$ are the characteristic transverse and axial resolution scales [49] corresponding to the optical wavelength λ of the point sources, an aperture of radius R , and distance z_O from the aperture to the pair centroid when located at the on-axis and in-focus position w.r.t. the aperture.

Our analysis presented here is technically correct only under the paraxial propagation conditions of a low-NA imager. However, for a high-NA imager, our results still provide an approximate description of the fundamental precision with which a pair of point sources may be resolved by the imager.

The coordinate representations, $\langle \mathbf{s} | K_{\pm} \rangle$, of the two states are the amplitude PSFs in the image-plane. Their momentum-space representations are the wavefunctions in the exit pupil of the imager [49],

$$\langle \mathbf{u} | K_{\pm} \rangle = \exp(\pm i\phi_0) P(\mathbf{u}) \exp[\mp i(2\pi \mathbf{l}_{\perp} \cdot \mathbf{u} + \pi l_z u^2)], \quad (4.3)$$

in which the linear and quadratic phases of each wavefunction represent, respectively, its tilt and curvature due to the off-axis, defocused location of the corresponding

Chapter 4. Achieving Quantum Limited 3D Super-resolution

source, and $P(\mathbf{u})$ denotes a general aperture function. For a clear aperture, $P(\mathbf{u})$ is simply $1/\sqrt{\pi}$ times its indicator function, corresponding to the Airy PSF, while in its Gaussian form, it yields the Gaussian PSF. More generally, $P(\mathbf{u})$ need only obey the normalization condition,

$$\int d^2u |P(\mathbf{u})|^2 = 1, \quad (4.4)$$

that follows from requiring $\langle K_{\pm}|K_{\pm}\rangle = 1$.

The two non-zero eigenvalues, e_{\pm} , and the associated orthonormal eigenstates, $|e_{\pm}\rangle$, of $\hat{\rho}$ given by Eq. (4.1) are readily calculated to be

$$e_{\pm} = (1 \pm \Delta)/2; \quad |e_{\pm}\rangle = [2(1 \pm \Delta)]^{-1/2} (|K_{+}\rangle \pm |K_{-}\rangle), \quad (4.5)$$

where Δ is the inner product, $\Delta = \langle K_{-}|K_{+}\rangle$, which we render real and positive by a proper choice of the phase constant, ϕ_0 .

The QFI matrix [19, 20, 21] is defined to have elements (see Appendix D)

$$H_{\mu\nu} \stackrel{\text{def}}{=} \text{ReTr} (\hat{\rho} \hat{L}_{\mu} \hat{L}_{\nu}), \quad (4.6)$$

where Re denotes the real part, \hat{L}_{μ} is the symmetric logarithmic derivative (SLD) of $\hat{\rho}$ w.r.t. parameter l_{μ} , defined by the relation,

$$\partial_{\mu} \hat{\rho} = \frac{1}{2} (\hat{L}_{\mu} \hat{\rho} + \hat{\rho} \hat{L}_{\mu}), \quad (4.7)$$

where for brevity we denote $\partial \hat{\rho} / \partial l_{\mu}$ as $\partial_{\mu} \hat{\rho}$. By taking the matrix element of \hat{L}_{μ} between the eigenstates $|e_i\rangle$ and $|e_j\rangle$ of $\hat{\rho}$, with eigenvalues e_i, e_j , respectively, and dividing both sides of the resulting expression by $(e_i + e_j)/2$, we obtain its matrix elements in the eigenbasis of $\hat{\rho}$,

$$\langle e_i | \hat{L}_{\mu} | e_j \rangle = \frac{2 \langle e_i | \partial_{\mu} \hat{\rho} | e_j \rangle}{(e_i + e_j)}. \quad (4.8)$$

Using expression (4.8) in the definition (4.6) of QFI and evaluating the trace in the eigenbasis of $\hat{\rho}$ immediately yields

$$H_{\mu\nu} = \text{Re} \sum_{i \in \mathcal{R}} \sum_j \frac{4e_i}{(e_i + e_j)^2} \langle e_i | \partial_{\mu} \hat{\rho} | e_j \rangle \langle e_j | \partial_{\nu} \hat{\rho} | e_i \rangle, \quad (4.9)$$

Chapter 4. Achieving Quantum Limited 3D Super-resolution

where \mathcal{R} denotes the set of values of the index that labels the eigenstates that span the range space of $\hat{\rho}$, or the subspace of non-zero eigenvalues of $\hat{\rho}$.

By decomposing the j sum into a sum over the range space of $\hat{\rho}$ and another over its null space, $j \notin \mathcal{R}$, for which $e_j = 0$, we may evaluate the latter sum via the completeness relation,

$$\sum_{j \notin \mathcal{R}} |e_j\rangle\langle e_j| = \hat{I} - \sum_{j \in \mathcal{R}} |e_j\rangle\langle e_j|.$$

We may thus express $H_{\mu\nu}$ in Eq. (4.9) as

$$\begin{aligned} H_{\mu\nu} &= \text{Re} \sum_{i \in \mathcal{R}} \frac{4}{e_i} \langle e_i | \partial_\mu \hat{\rho} \partial_\nu \hat{\rho} | e_i \rangle \\ &+ \text{Re} \sum_{i \in \mathcal{R}} \sum_{j \in \mathcal{R}} \left[\frac{4e_i}{(e_i + e_j)^2} - \frac{4}{e_i} \right] \langle e_i | \partial_\mu \hat{\rho} | e_j \rangle \langle e_j | \partial_\nu \hat{\rho} | e_i \rangle. \end{aligned} \quad (4.10)$$

For the two-state $\hat{\rho}$ discussed here, the range space is two-dimensional, and the general expression for the QFI matrix element reduces to the form,

$$\begin{aligned} H_{\mu\nu} &= \text{Re} \sum_{i=\pm} \frac{4}{e_i} \langle e_i | \partial_\mu \hat{\rho} \partial_\nu \hat{\rho} | e_i \rangle \\ &+ \text{Re} \sum_{i=\pm} \sum_{j=\pm} \left[\frac{4e_i}{(e_i + e_j)^2} - \frac{4}{e_i} \right] \langle e_i | \partial_\mu \hat{\rho} | e_j \rangle \langle e_j | \partial_\nu \hat{\rho} | e_i \rangle. \end{aligned} \quad (4.11)$$

We may simplify the derivatives in Eq. (4.11) by noting the eigenvector identity, $\partial_\mu [(\hat{\rho} - e_i \hat{I}) | e_i \rangle] = 0$, *i.e.*,

$$\partial_\mu \hat{\rho} | e_i \rangle = \partial_\mu e_i | e_i \rangle - (\hat{\rho} - e_i \hat{I}) \partial_\mu | e_i \rangle. \quad (4.12)$$

Taking the inner product of Eq. (4.12) with $\langle e_j |$ and then using the eigenrelation, $\langle e_j | (\hat{\rho} - e_i) = (e_j - e_i) \langle e_j |$, and the orthonormality of the eigenstates, we obtain one of the needed matrix elements,

$$\langle e_j | \partial_\mu \hat{\rho} | e_i \rangle = \delta_{ij} \partial_\mu e_i + (e_i - e_j) \langle e_j | \partial_\mu | e_i \rangle. \quad (4.13)$$

Chapter 4. Achieving Quantum Limited 3D Super-resolution

Multiplying Eq. (4.12) by its adjoint, with μ in the former replaced by ν , we obtain the following expression for the first of the matrix elements in Eq. (4.11):

$$\langle e_i | \partial_\mu \hat{\rho} \partial_\nu \hat{\rho} | e_i \rangle = \partial_\mu e_i \partial_\nu e_i + \partial_\mu \langle e_i | (\hat{\rho} - e_i \hat{I})^2 \partial_\nu | e_i \rangle, \quad (4.14)$$

with the eigenrelation, $(\hat{\rho} - e_i \hat{I}) | e_i \rangle = 0$, eliminating the other two terms in the product. A substitution of relations (4.13) and (4.14) into Eq. (4.11) simplifies it, particularly when the $i = j$ terms in the double sum in Eq. (4.11) are combined with its first sum and we note that in the remaining two, $i \neq j$ terms of the double sum, $e_i + e_j = e_+ + e_- = 1$, and $e_+ - e_- = \Delta$. The QFI matrix element may thus be expressed as

$$\begin{aligned} H_{\mu\nu} = & \sum_{i=\pm} \frac{1}{e_i} \partial_\mu e_i \partial_\nu e_i + 4\text{Re} \sum_{i=\pm} \frac{1}{e_i} (\partial_\mu \langle e_i |) (\hat{\rho} - e_i \hat{I})^2 \partial_\nu | e_i \rangle \\ & + 4\Delta^2 \text{Re} \sum_{i \neq j} \left(\frac{1}{e_i} - e_i \right) \langle e_i | \partial_\mu | e_j \rangle \langle e_j | \partial_\nu | e_i \rangle. \end{aligned} \quad (4.15)$$

The first sum in expression (4.15) may be regarded as the classical part of QFI, the second sum the contribution of quantum fluctuations of the photon state to QFI, and the final sum an additional contribution from the pair cross-coherence, $\Delta \neq 0$.

From the specific forms of the eigenvalues and eigenvectors in (4.5), we see that

$$\partial_\mu | e_\pm \rangle = \mp \frac{\partial_\mu \Delta}{2(1 \pm \Delta)} | e_\pm \rangle + \frac{1}{\sqrt{2(1 \pm \Delta)}} (\partial_\mu | K_+ \rangle \pm \partial_\mu | K_- \rangle). \quad (4.16)$$

By successively taking the inner product of Eq. (4.16) with $| e_+ \rangle$ and $| e_- \rangle$, we obtain the matrix elements,

$$\begin{aligned} \langle e_+ | \partial_\mu | e_+ \rangle &= -\frac{\partial_\mu \Delta}{2(1 + \Delta)} + \frac{1}{2(1 + \Delta)} (\langle K_+ | + \langle K_- |) (\partial_\mu | K_+ \rangle + \partial_\mu | K_- \rangle); \\ \langle e_- | \partial_\mu | e_+ \rangle &= \frac{1}{2\sqrt{1 - \Delta^2}} (\langle K_+ | - \langle K_- |) (\partial_\mu | K_+ \rangle + \partial_\mu | K_- \rangle). \end{aligned} \quad (4.17)$$

Since $\langle K_+ | K_+ \rangle$ is 1, by taking its derivative, we have

$$(\partial_\mu \langle K_+ |) | K_+ \rangle + \langle K_+ | \partial_\mu | K_+ \rangle = 0. \quad (4.18)$$

Chapter 4. Achieving Quantum Limited 3D Super-resolution

Since the wavefunctions, $\langle \mathbf{u} | K_{\pm} \rangle$, have the form (4.3), we may express $(\partial_{\mu} \langle K_+ |) | K_+ \rangle$ as $\langle K_- | \partial_{\mu} | K_- \rangle$, therefore

$$\langle K_+ | \partial_{\mu} | K_+ \rangle = -\langle K_- | \partial_{\mu} | K_- \rangle. \quad (4.19)$$

By taking the derivative of $\langle K_- | K_+ \rangle = \Delta$, which is real due to the choice of the phase constant ϕ_0 , we have $(\partial_{\mu} \langle K_- |) | K_+ \rangle + \langle K_- | \partial_{\mu} | K_+ \rangle = \partial_{\mu} \Delta$. Because of the form (4.3) of $\langle \mathbf{u} | K_{\pm} \rangle$, we have $(\partial_{\mu} \langle K_- |) | K_+ \rangle = \langle K_- | \partial_{\mu} | K_+ \rangle$, therefore

$$\langle K_- | \partial_{\mu} | K_+ \rangle = \langle K_+ | \partial_{\mu} | K_- \rangle = \frac{1}{2} \partial_{\mu} \Delta. \quad (4.20)$$

By using (4.19) and (4.20), we may simplify the matrix elements (4.17) as,

$$\langle e_+ | \partial_{\mu} | e_+ \rangle = 0; \quad \langle e_- | \partial_{\mu} | e_+ \rangle = \frac{1}{\sqrt{1 - \Delta^2}} \langle K_+ | \partial_{\mu} | K_+ \rangle. \quad (4.21)$$

Due to the eigen-relation, $\hat{\rho} = e_+ | e_+ \rangle \langle e_+ | + e_- | e_- \rangle \langle e_- |$, and the first relation in (4.21), we may write

$$(\hat{\rho} - e_+ \hat{I}) \partial_{\mu} | e_+ \rangle = e_- | e_- \rangle \langle e_- | \partial_{\mu} | e_+ \rangle - e_+ \partial_{\mu} | e_+ \rangle. \quad (4.22)$$

By taking the inner product of Eq. (4.22) with its adjoint, with μ in the former replaced by ν , we obtain

$$\begin{aligned} (\partial_{\mu} \langle e_+ |) (\hat{\rho} - e_+ \hat{I})^2 \partial_{\nu} | e_+ \rangle &= (e_-^2 - e_- e_+) \langle e_- | \partial_{\mu} | e_+ \rangle^* \langle e_- | \partial_{\nu} | e_+ \rangle \\ &\quad - e_- e_+ (\partial_{\mu} \langle e_+ |) | e_- \rangle \langle e_- | \partial_{\nu} | e_+ \rangle + e_+^2 (\partial_{\mu} \langle e_+ |) \partial_{\nu} | e_+ \rangle \\ &= -(e_-^2 - 2e_- e_+) \langle e_+ | \partial_{\mu} | e_- \rangle \langle e_- | \partial_{\nu} | e_+ \rangle \\ &\quad + e_+^2 (\partial_{\mu} \langle e_+ |) \partial_{\nu} | e_+ \rangle, \end{aligned} \quad (4.23)$$

in which we used the relations, $(\partial_{\mu} \langle e_+ |) | e_- \rangle = \partial_{\mu} (\langle e_+ | e_- \rangle) - \langle e_+ | \partial_{\mu} | e_- \rangle$ and $\langle e_+ | e_- \rangle = 0$ to reach the last equality.

From formula (4.16), we may calculate $(\partial_{\mu} \langle e_+ |) \partial_{\nu} | e_+ \rangle$ in Eq. (4.23) as

$$\begin{aligned}
 (\partial_\mu \langle e_+ |) \partial_\nu |e_+\rangle &= \left[-\frac{\partial_\mu \Delta}{2(1+\Delta)} \langle e_+ | + \frac{1}{\sqrt{2(1+\Delta)}} (\partial_\mu \langle K_+ | + \partial_\mu \langle K_- |) \right] \\
 &\times \left[-\frac{\partial_\nu \Delta}{2(1+\Delta)} |e_+\rangle + \frac{1}{\sqrt{2(1+\Delta)}} (\partial_\nu |K_+\rangle + \partial_\nu |K_-\rangle) \right] \\
 &= -\frac{\partial_\mu \Delta \partial_\nu \Delta}{4(1+\Delta)^2} \\
 &\quad + \frac{1}{2(1+\Delta)} (\partial_\mu \langle K_+ | + \partial_\mu \langle K_- |) (\partial_\nu |K_+\rangle + \partial_\nu |K_-\rangle), \quad (4.24)
 \end{aligned}$$

in which to arrive at the last equality we used expression (4.5) for the eigenstate $|e_+\rangle$ and the first relation in Eq. (4.21) and its Hermitian adjoint to make the simplifications,

$$\langle e_+ | (\partial_\nu |K_+\rangle + \partial_\nu |K_-\rangle) = \frac{1}{\sqrt{2(1+\Delta)}} \partial_\nu \Delta; \quad (\partial_\mu \langle K_+ | + \partial_\mu \langle K_- |) |e_+\rangle = \frac{1}{\sqrt{2(1+\Delta)}} \partial_\mu \Delta. \quad (4.25)$$

Interchanging e_+ and e_- everywhere in Eq. (4.23) yields the second matrix element we need,

$$(\partial_\mu \langle e_- |) (\hat{\rho} - e_-)^2 \partial_\nu |e_-\rangle = -(e_+^2 - 2e_- e_+) \langle e_- | \partial_\mu |e_+\rangle \langle e_+ | \partial_\nu |e_-\rangle + e_-^2 (\partial_\mu \langle e_- |) \partial_\nu |e_-\rangle, \quad (4.26)$$

in which the last of the matrix elements is given by replacing Δ by $-\Delta$ and $|K_-\rangle$ by $-|K_-\rangle$ in Eq. (4.24),

$$(\partial_\mu \langle e_- |) \partial_\nu |e_-\rangle = -\frac{\partial_\mu \Delta \partial_\nu \Delta}{4(1-\Delta)^2} + \frac{1}{2(1-\Delta)} (\partial_\mu \langle K_+ | - \partial_\mu \langle K_- |) (\partial_\nu |K_+\rangle - \partial_\nu |K_-\rangle). \quad (4.27)$$

Since $K_\pm(\mathbf{u})$ are mutually complex-conjugate phase exponentials over the aperture, it follows that $(\partial_\mu \langle K_+ |) \partial_\nu |K_-\rangle = (\partial_\mu \langle K_- |) \partial_\nu |K_+\rangle^*$ and $(\partial_\mu \langle K_+ |) \partial_\nu |K_+\rangle = (\partial_\mu \langle K_- |) \partial_\nu |K_-\rangle^*$, the latter being already real, the last part of expression (4.24)

Chapter 4. Achieving Quantum Limited 3D Super-resolution

reduces further. Substituting the so-reduced form of this expression into relation (4.23) and the resulting expression into form (4.15) for the QFI matrix element and noting from relation (4.5) that $\partial_\mu e_i \partial_\nu e_i = (1/4)\partial_\mu \Delta \partial_\nu \Delta$, $i = \pm$, yields an exact cancellation of all $\partial_\mu \Delta \partial_\nu \Delta$ terms and yields the following simplified expression for the QFI matrix element:

$$\begin{aligned}
 H_{\mu\nu} = & -\frac{4}{e_+} \text{Re} \{ (e_-^2 - 2e_- e_+) \langle e_+ | \partial_\mu | e_- \rangle \langle e_- | \partial_\nu | e_+ \rangle \} \\
 & -\frac{4}{e_-} \text{Re} \{ (e_+^2 - 2e_- e_+) \langle e_- | \partial_\mu | e_+ \rangle \langle e_+ | \partial_\nu | e_- \rangle \} \\
 & + 4 \text{Re} [(\partial_\mu \langle K_+ |) \partial_\nu | K_+ \rangle] + 4\Delta^2 \text{Re} \sum_{i \neq j} \left(\frac{1}{e_i} - e_i \right) \langle e_i | \partial_\mu | e_j \rangle \langle e_j | \partial_\nu | e_i \rangle.
 \end{aligned} \tag{4.28}$$

The first two terms and the last term on the RHS of Eq. (4.28) may be combined and simplified with the second identity in Eq. (4.21), and noting that $e_-^2 - 2e_+ e_- = (e_+ - e_-)^2 - e_+^2 = \Delta^2 - e_+^2$ and analogously $e_+^2 - 2e_+ e_- = \Delta^2 - e_-^2$ to derive the more compact result,

$$H_{\mu\nu} = 4 [(\partial_\mu \langle K_+ |) \partial_\nu | K_+ \rangle + \langle K_+ | \partial_\mu | K_+ \rangle \langle K_+ | \partial_\nu | K_+ \rangle]. \tag{4.29}$$

By using expression (4.3) for $\langle \mathbf{u} | K_+ \rangle$, we may evaluate Eq. (4.29) in terms of the gradient of the phase function,

$$\Psi(\mathbf{u}; \boldsymbol{\ell}) = 2\pi \mathbf{l}_\perp \cdot \mathbf{u} + \pi l_z u^2, \tag{4.30}$$

independently of ϕ_0 as

$$H_{\mu\nu} = 4 [\langle \partial_\mu \Psi \partial_\nu \Psi \rangle - \langle \partial_\mu \Psi \rangle \langle \partial_\nu \Psi \rangle], \tag{4.31}$$

where angular brackets now denote averages over the modulus squared aperture function, $|P(\mathbf{u})|^2$.

Form (4.31) of QFI underscores the fundamental role of the correlations of the wavefront gradient in the aperture in controlling the error of estimation of the pair

separation. For a clear circular aperture, to which we restrict attention in the rest of this chapter and for which $|P(\mathbf{u})|^2$ is $1/\pi$ times its indicator function, simple integrations yield the following averages:

$$\langle u_i \rangle = 0; \quad \langle u_i u_j \rangle = \frac{\delta_{ij}}{4}; \quad \langle u^2 \rangle = \frac{1}{2}; \quad \langle u^4 \rangle = \frac{1}{3}; \quad i, j = x, y, \quad (4.32)$$

and thus the following purely diagonal form of the per-photon 3D QFI matrix:

$$\mathbf{H}(l_x, l_y, l_z) = \begin{pmatrix} 4\pi^2 & 0 & 0 \\ 0 & 4\pi^2 & 0 \\ 0 & 0 & \frac{\pi^2}{3} \end{pmatrix}, \quad (4.33)$$

which is independent altogether of the 3D pair-separation coordinates.

We next show that QFI for localizing a single source, say the one located at $+(\mathbf{l}_\perp, l_z)$, is identical to that we have just obtained for 3D pair separation. For this problem, only the middle term in expression (4.15) contributes, since $\hat{\rho} = |K_+\rangle\langle K_+|$ has a single fixed non-zero eigenvalue, $e_+ = 1$, with eigenstate $|e_+\rangle = |K_+\rangle$, and $(\hat{\rho} - \hat{I})^2 = \hat{I} - |K_+\rangle\langle K_+|$. In view of these relations and normalization, $\langle K_+|K_+\rangle = 1$, which requires that $(\partial_\mu \langle K_+|)|K_+\rangle = -\langle K_+|\partial_\mu|K_+\rangle$, the resulting QFI becomes identical to Eq. (4.29) for QFI for source-pair separation. The equality of the QFI matrices for source localization and pair separation shows that the general problem is one of estimating the photon state, independent of the nature of its emitter.

4.3 Achieving QFI in Two Special Cases

In this section we show that QCRB is achievable via complete orthonormal wavefront projections in two special cases of either a purely transversely separated or axially separated source pair. For sources in the same transverse plane, for which $l_z = 0$, consider an orthonormal basis, $\mathcal{A} = \{A_{mn}(\mathbf{u})|m, n \in \mathbb{Z}\}$, of states in the aperture

Chapter 4. Achieving Quantum Limited 3D Super-resolution

plane obeying the condition, $|\langle K_+ | A_{mn} \rangle| = |\langle K_- | A_{mn} \rangle|$, $\forall m, n$. Since $\langle \mathbf{u} | K_+ \rangle = \langle \mathbf{u} | K_- \rangle^*$, this condition is met by *any* real basis. The probability $P_{mn}^{(A)}$ of detecting the photon in A_{mn} state, which is given by $\langle A_{mn} | \hat{\rho} | A_{mn} \rangle$, may then be expressed as $P_{mn}^{(A)} = |\langle K_+ | A_{mn} \rangle|^2$, from which we have the CFI matrix elements,

$$J_{\mu\nu}[\mathcal{A}] = \sum_{m,n} \frac{\partial_\mu P_{mn}^{(A)} \partial_\nu P_{mn}^{(A)}}{P_{mn}^{(A)}} = 4 \sum_{m,n} \partial_\mu |\langle A_{mn} | K_+ \rangle| \partial_\nu |\langle A_{mn} | K_+ \rangle|. \quad (4.34)$$

If we assume further that the phases of $\langle K_+ | A_{mn} \rangle$ have no \mathbf{l}_\perp dependence, then Eq. (4.34) reduces to

$$J_{\mu\nu}[\mathcal{A}] = 4 \sum_{m,n} (\partial_\mu \langle K_+ |) | A_{mn} \rangle \langle A_{mn} | \partial_\nu | K_+ \rangle = 4 (\partial_\mu \langle K_+ |) \partial_\nu | K_+ \rangle. \quad (4.35)$$

with the second equality following from the completeness relation,

$$\sum_{m,n} | A_{mn} \rangle \langle A_{mn} | = \hat{I}.$$

For $\mu, \nu = x, y$, $J_{\mu\nu}[\mathcal{A}]$ matches QFI in expression (4.29) since for the choice, $\phi_0 = 0$, we make to render the phases of $\langle K_+ | A_{mn} \rangle$ independent of \mathbf{l}_\perp , $\langle K_+ | \partial_\mu | K_+ \rangle$, vanishes identically for any inversion symmetric aperture.

The orthonormal sine-cosine Fourier basis states in polar coordinates, (u, ϕ) ,

$$\begin{aligned} \text{CC}_{mn}(\mathbf{u}) &= \sqrt{\frac{c_m c_n}{\pi}} \cos(2\pi m u^2) \cos n\phi, & m, n = 0, 1, \dots; \\ \text{CS}_{mn}(\mathbf{u}) &= \sqrt{\frac{c_m c_n}{\pi}} \cos(2\pi m u^2) \sin n\phi, & m = 0, 1, \dots, n = 1, 2, \dots; \\ \text{SC}_{mn}(\mathbf{u}) &= \sqrt{\frac{c_m c_n}{\pi}} \sin(2\pi m u^2) \cos n\phi, & m = 1, 2, \dots, n = 0, 1, \dots; \\ \text{SS}_{mn}(\mathbf{u}) &= \sqrt{\frac{c_m c_n}{\pi}} \sin(2\pi m u^2) \sin n\phi, & m, n = 1, 2, \dots; \end{aligned} \quad (4.36)$$

with $c_n = 2 - \delta_{n0}$, constitute one such basis that achieves QFI for the case of pure transverse pair separation as their overlap integrals with the photon wavefront of each source can be readily shown in Appendix E to have phases that are independent of that separation.

Chapter 4. Achieving Quantum Limited 3D Super-resolution

For the source pair purely separated along the optical axis, *i.e.*, $l_{\perp} = 0$, only the $n = 0$ subset of the sine-cosine basis, as we need no angular localization, achieves QCRB w.r.t. l_z , as we show next. The relevant probability amplitudes are

$$\begin{aligned}\langle A_{m0}|K_+\rangle &= \frac{1}{\sqrt{\pi}} \int_0^1 du u \exp(-i\pi l_z u^2) A_{m0}(u) \\ &= \frac{1}{2\sqrt{\pi}} \exp\left(-i\pi \frac{l_z}{2}\right) \int_{-1/2}^{1/2} dv \cos(\pi l_z v) A_{m0}(\sqrt{v+1/2}),\end{aligned}\quad (4.37)$$

with $A = \text{CC}, \text{SC}$. We used the variable transformation, $v = u^2 - 1/2$, followed by a symmetrization of the resulting integrand to reach the second equality in Eq. (4.37) that involves a purely real integral. In view of the form (4.37), we have $|\langle A_{m0}|K_+\rangle| = \exp(i\pi l_z/2) \langle A_{m0}|K_+\rangle$, which allows us, analogously to Eq. (4.34) with $\mu = \nu = z$, to express FI w.r.t. l_z as

$$\begin{aligned}J_{zz}[\mathcal{A}] &= 4 \sum_m |\partial_z \langle A_{m0}|K_+\rangle|^2 \\ &= 4 \sum_m [\partial_z(\langle K_+|)|A_{m0}\rangle - i(\pi/2)\langle K_+|A_{m0}\rangle] \\ &\quad \times [\langle A_{m0}|\partial_z|K_+\rangle + i(\pi/2)\langle A_{m0}|K_+\rangle] \\ &= 4 [\partial_z(\langle K_+|)|\partial_z|K_+\rangle - i(\pi/2)\langle K_+|\partial_z|K_+\rangle \\ &\quad + i(\pi/2)(\partial_z|K_+\rangle|K_+\rangle + (\pi/2)^2] \\ &= 4 [\partial_z(\langle K_+|)|\partial_z|K_+\rangle - \pi^2/4] \\ &= 4 [\partial_z(\langle K_+|)|\partial_z|K_+\rangle + \langle K_+|\partial_z|K_+\rangle^2]\end{aligned}\quad (4.38)$$

in which we used the completeness of the $|A_{m0}\rangle$ states over the aperture for ϕ -invariant wavefunctions like $\langle \mathbf{u}|K_+\rangle$ characteristic of an axially separated source pair and relations, $\langle K_+|\partial_z|K_+\rangle = (\partial_z \langle K_+|)|K_+\rangle^* = -i\pi \langle u^2 \rangle = -i\pi/2$, to derive the various expressions. We see from expression (4.29) that the $\{A_{m0}|A = \text{CC}, \text{SC}, m = 0, 1, \dots\}$ basis achieves QFI w.r.t. l_z for an axially separated source pair. More generally, *any real* basis of orthonormal projections, $\{|B_m\rangle\}$, for which the equality, $|\langle B_m|K_+\rangle| = |\langle B_m|K_-\rangle|$, certainly holds, will achieve QFI.

4.4 Achieving QFI in the Limit of Small Separations

In this section we show that projections that are well matched to the linear tilt and quadratic defocus parts of the aperture phase function, $\Psi(\mathbf{u})$, given by Eq. (4.30), can achieve full 3D QFI in the limit of small separations, $l_{\perp}, l_z \ll 1$. Let us consider aperture-plane wavefront projections into the first four Zernike basis functions [50],

$$Z_1 = \frac{1}{\sqrt{\pi}}, \quad Z_2 = \frac{2}{\sqrt{\pi}}u \cos \phi, \quad Z_3 = \frac{2}{\sqrt{\pi}}u \sin \phi, \quad Z_4 = \sqrt{\frac{3}{\pi}}(2u^2 - 1). \quad (4.39)$$

We see that Z_2 and Z_3 correlate perfectly with the tilt phases corresponding to the x and y components of the transverse separation vector, \mathbf{l}_{\perp} , and may thus be regarded as matched filters [51] for the latter. By contrast, Z_1 and Z_4 are both partially matched to the quadratic pupil phase corresponding to the axial separation, l_z , with their probabilities remaining finite when $l_z \rightarrow 0$. The imperfect match of the latter with a single projection mode, since each of Z_1 and Z_4 has a nonvanishing overlap integral with the quadratic pupil phase function, causes striking differences, as we shall see, in the estimation error bounds that are achievable in the limit of vanishing separation.

The probability of detecting the photon in Zernike mode, Z_n , may be expressed as

$$P_n = \left[\int d^2u P(u) Z_n(\mathbf{u}) \cos \Psi \right]^2 + \left[\int d^2u P(u) Z_n(\mathbf{u}) \sin \Psi \right]^2, \quad (4.40)$$

for $n = 1, 2, 3$, and 4, with the probability of finding it in the remaining, unmeasured modes being

$$\bar{P} = 1 - P_1 - P_2 - P_3 - P_4. \quad (4.41)$$

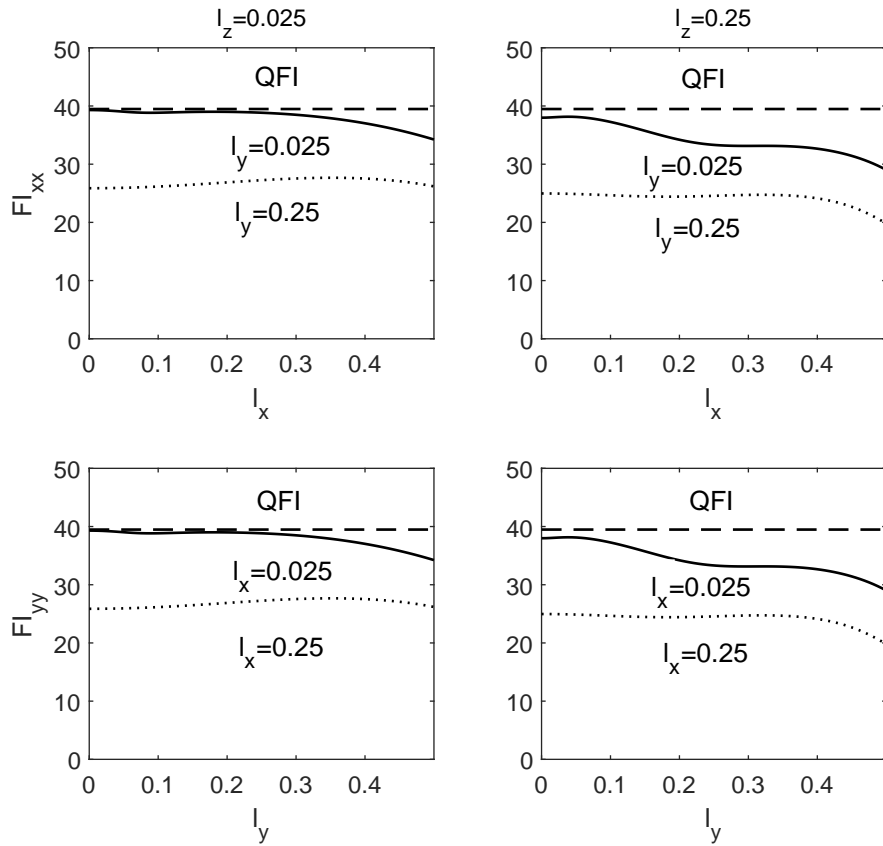


Figure 4.1: Plots of QFI (dashed line) and CFI w.r.t. $l_{x(y)}$ for $l_{y(x)} = 0.025$ (lower curve) and $l_{y(x)} = 0.25$ (upper curve) and for $l_z = 0.025$ (left panels) and $l_z = 0.25$ (right panels).

For a clear circular aperture, for which $P(\mathbf{u})$ is simply $1/\sqrt{\pi}$ times the indicator function of the unit-radius aperture, and for small separation coordinates, $l_{\perp}, l_z \ll 1$, we retain only the first two orders in the Taylor expansions of the $\sin \Psi$ and $\cos \Psi$ in functions Eq. (4.40). Orthonormality of the Zernikes implies $\int d^2u P(u) Z_n(\mathbf{u}) = \delta_{n1}$, from which it follows that up to the lowest two orders in Ψ and thus in ℓ , P_n has the form,

$$P_n = \begin{cases} 1 - (\langle \Psi^2 \rangle - \langle \Psi \rangle^2) & n = 1 \\ \pi \left[\langle Z_n \Psi \rangle^2 + \frac{1}{4} \langle Z_n \Psi^2 \rangle^2 - \frac{1}{3} \langle Z_n \Psi \rangle \langle Z_n \Psi^3 \rangle \right] & n \geq 2, \end{cases} \quad (4.42)$$

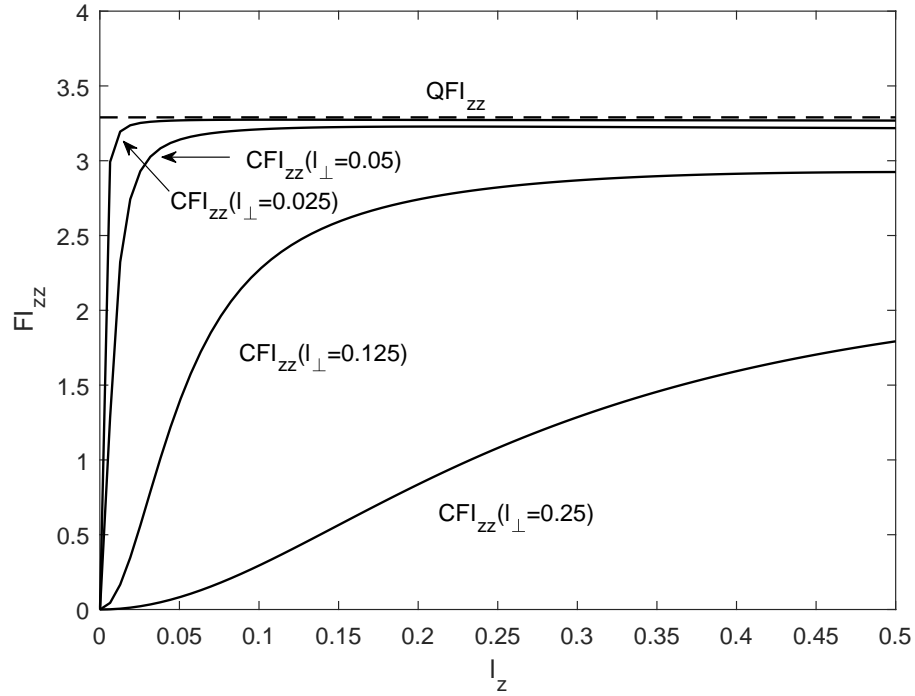


Figure 4.2: Plots of QFI (dash line) and CFI w.r.t. l_z , for four different values of l_\perp , namely 0.025, 0.05, 0.125, and 0.25.

in which angular brackets denote averages over the clear aperture. Using expressions (4.30) for the wavefront phase, and the Zernike modes (4.39), we may easily evaluate these averages to obtain the probabilities to two lowest significant orders in the separation vector, $\boldsymbol{\ell}$,

$$P_n = \begin{cases} 1 - \pi^2(l_\perp^2 + l_z^2/12) + O(l_\perp^4, l_z^4) & n = 1 \\ \pi^2 l_x^2 [1 + O(l_\perp^2, l_z^2)] & n = 2 \\ \pi^2 l_y^2 [1 + O(l_\perp^2, l_z^2)] & n = 3 \\ \pi^2 l_z^2 / 12 + O(l_z^4, l_z^2 l_\perp^2, l_\perp^4) & n = 4 \end{cases} \quad (4.43)$$

Since $(\partial_x P_2)^2 / P_2 = (\partial_y P_3)^2 / P_3 = 4\pi^2 [1 + O(l_z^2)]$, we see that each reaches QFI in the limit $l_z \rightarrow 0$. By contrast, the Z_4 projection contributes to FI w.r.t. l_z the term, $(\partial_z P_4)^2 / P_4$, which is of form $(\pi^2/3) \{l_z^2 / [l_z^2 (1 + O(l_\perp^2)) + O(l_\perp^4)]\}$ and vanishes in the

limit $l_z \rightarrow 0$ if $l_\perp \neq 0$. The same form implies, however, that for $l_\perp \ll 1$, FI as a function of l_z rises to a value comparable to the QFI, $\pi^2/3$, over an interval of order l_\perp^2 . All other contributions to the various matrix elements of FI are negligibly small in the limit of vanishing ℓ , so the inverse of the diagonal elements of FI determine the corresponding CRBs to the most significant order in ℓ .

In Figs. (4.1) and (4.2) we show the numerical evaluation of CFI matrix elements for the proposed wavefront projection protocol with the first four Zernike modes. In Fig. (4.1) we display the CFI for transverse separations of the source pair along the x and y axes (top and bottom panels) for two values of their axial separation (left and right panels) and two values of the other transverse coordinate (upper and lower curves). In Fig. (4.2) we display the CFI for the axial separation of the source pair for four values of their transverse separation. The corresponding diagonal elements of the QFI matrix are shown in dashed line for comparison. Our earlier assertion about the attainability of the QFI in small separation limit is clearly verified with these two figures.

4.5 Maximum-Likelihood Estimation of Pair Separation

Paúr *et al.* showed that wavefront projections could be achieved by digital holographic techniques [28]. Let us consider encoding the sum, $\sum_{n=1}^N Z_n(\mathbf{u}) \cos(\mathbf{q}_n \cdot \mathbf{u})$, as the distribution of the amplitude transmittance of a plate. Let the imaging wavefront, which is an incoherent superposition of the photon wavefunctions $\langle \mathbf{u} | K_\pm \rangle$ and carries M photons, be incident on such a plate that is placed in the aperture, and then optically focused on a sensor. Let us note that $\cos(\mathbf{q}_n \cdot \mathbf{u})$ occurring in the plate transmittance function may be expressed as 1/2 times the sum of two exponentials,

$\exp(\pm \mathbf{q}_n \cdot \mathbf{u})$. As a result, the plate will cause the M photons to divide into N pairs of oppositely located spots, with the n th pair of spots corresponding to an obliquely propagating wave pair that carries the Z_n projection of the incident wavefront along the spherical-angle pair, $(\theta_n, \pm\phi_n)$, with $\theta_n = \sin^{-1}(q_n/k)$, $\phi_n = \tan^{-1}(q_{ny}/q_{nx})$. The numbers of photons detected at the central pixels of the spots taken pairwise furnish estimates of the probabilities of the wavefront being in the corresponding modes. The remaining photons that are not detected provide an estimate of the wavefront being in the remaining states of a complete basis of which the subset, $\{Z_n, n = 1, \dots, N\}$, defines the observed states. According to Appendix F, the probability of detecting m_1, \dots, m_N photons in the N projective channels is given by the multinomial (MN) distribution, which for perfect quantum-efficiency detectors has the form

$$\text{Prob}(\bar{m}, \{m_n\}|\{P_n\}) = M! \frac{\bar{P}^{\bar{m}}}{\bar{m}!} \prod_{n=1}^N \frac{(P_n)^{m_n}}{m_n!}, \quad (4.44)$$

in which $\bar{m} = M - \sum_{n=1}^N m_n$ and $\bar{P} = 1 - \sum_{n=1}^N P_n$ are, respectively, the number and probability of undetected photons. Here $N = 4$. Expressing the P_n in terms of the separation coordinates, l_x, l_y, l_z , we performed maximum-likelihood (ML) estimation by numerically minimizing $-\ln \text{Prob}$ over the separation coordinates using Matlab's *fminunc* minimizer, for various separations, 20,000 noisy frames, each with $M = 10^6$ photons and generated with Matlab's *mnrnd* code, our starting guess is always chosen to be $l_x = l_y = l_z = 0.25$.

In Fig. 4.3 we plot the per-photon CRBs w.r.t. l_x (top panels) and l_y (bottom panels) for two different values of their axial separation, $l_z = 0.025$ (left panels) and 0.25 (right panels). In each plot, we chose two different values of the other transverse coordinate, namely 0.025 and 0.25 , displayed with two different curves in each figure. Note that CRB w.r.t. each transverse-separation coordinate increases with increasing value of the other coordinate due to a cross-talk between the two transverse coordinates. Changing the longitudinal separation, however, has a less pronounced effect on those curves. As the pair separation increases, using only the

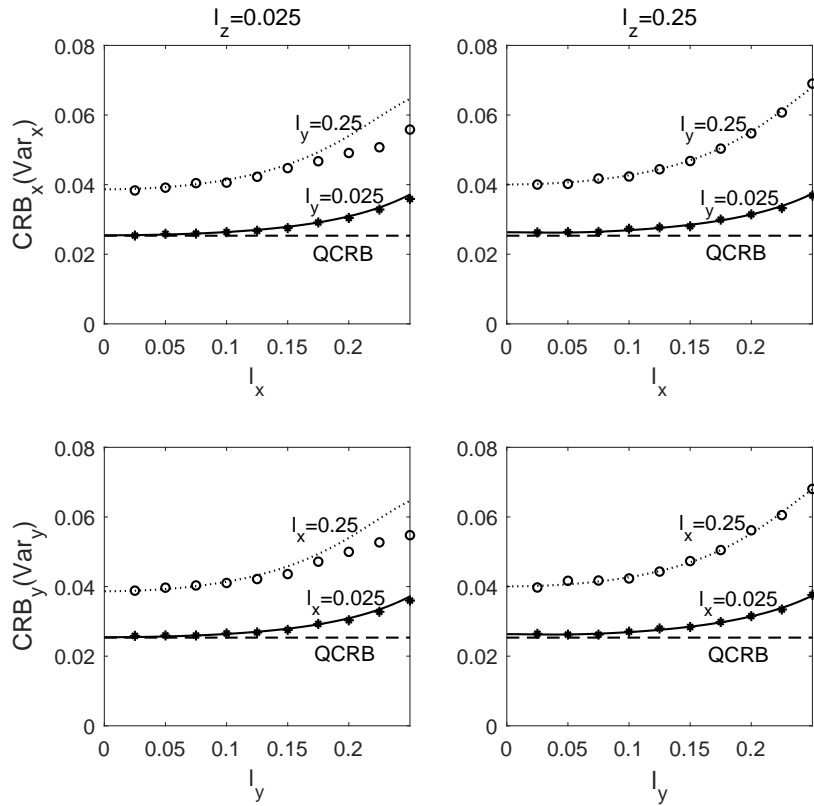


Figure 4.3: Plots of CRBs w.r.t. $l_{x(y)}$ for $l_{y(x)} = 0.025$ (lower curve) and $l_{y(x)} = 0.25$ (upper curve) and for $l_z = 0.025$ (left panels) and $l_z = 0.25$ (right panels). Variances obtained from ML estimation are shown by different marker symbols. Image taken from Ref. [48].

first four Zernikes is insufficient to estimate \mathbf{l}_\perp , which accounts in part for the rising CRB curves. The discrete points identified by marker symbols are the results of the sample-based variance (per photon) of the ML estimate of the separation coordinates that we obtained in our numerical simulations. Note that the results of simulation are consistently lower than the corresponding CRB curves, which is most discernible in the left panels ($l_z = 0.025$). This is because the ML estimates of the separation coordinates are biased, particularly that for l_z , and standard CRBs do not provide the correct lower bounds without including bias-gradient based modifications [14, 15].

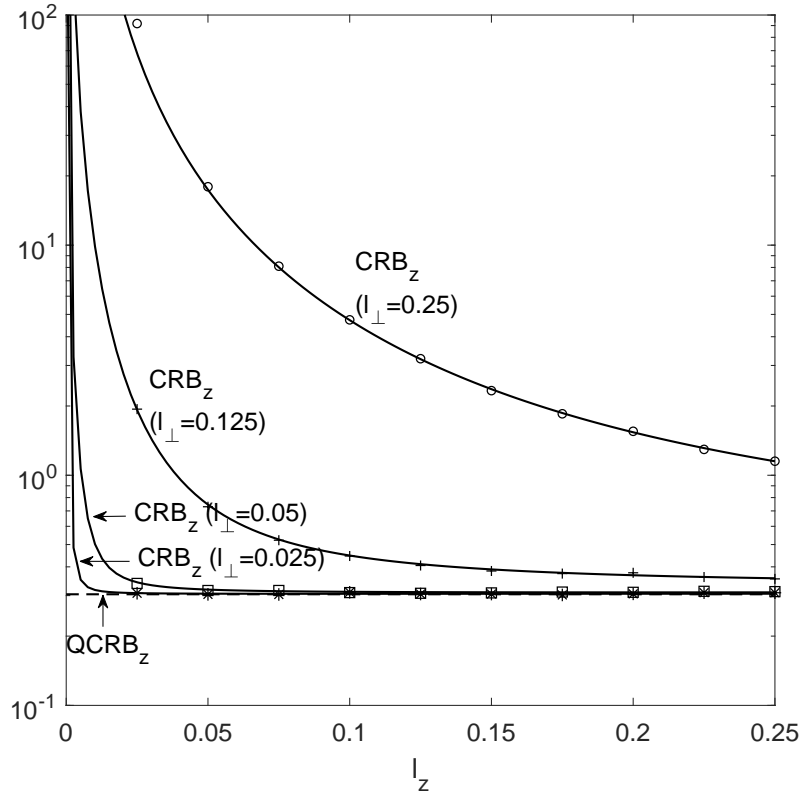


Figure 4.4: Plots of CRB w.r.t. l_z , for four different values of l_\perp , namely 0.025, 0.05, 0.125, and 0.25. Variances obtained from ML estimation are shown by different marker symbols. Image taken from Ref. [48].

In Fig. 4.4 we plot the per-photon CRBs w.r.t. l_z for four different values of l_\perp . We observe divergent behavior as l_z approaches zero, corresponding to the vanishing of $J_{zz}[Z]$ whenever $l_\perp \neq 0$ that we noted earlier. This behavior is quite in contrast with the rather weak dependence on l_z which we observed in Fig. 4.3 for the CRBs w.r.t. l_\perp . The cross-talk between the uncertainties in simultaneously estimating the three pair-separation coordinates inherently present in the small set of Zernike projections increases the CRB for the l_z estimation as l_\perp increases. The simulated values of the variance of the estimator of l_z , indicated by marker symbols, agree well with the theoretical CRB values.

4.6 Conclusions

In this Chapter we have treated the fundamental limits in estimating the full 3D separation vector of a balanced incoherent source pair with known centroid by calculating the corresponding QFI matrix and proposing specific projection bases for which the corresponding QCRB can be saturable in special cases of pure lateral and axial separations and in the limit of small separations. We have also used maximum-likelihood estimation with Zernike channels to confirm the predicted attainability of the bounds. The fact that the QCRBs are saturated by purely classical measurements using Zernike projections, while surprising, parallels previous results for 2D pair super-resolution [27].

References

- [1] L. Rayleigh, “XXXI. Investigations in Optics, with Special Reference to the Spectroscope,” *Philos. Mag.* **8**, 261 (1879).
- [2] W. E. Moerner and L. Kador, “Optical detection and spectroscopy of single molecules in a solid,” *Phys. Rev. Lett.* **62**, 2535 (1989).
- [3] S. W. Hell and J. Wichmann, “Breaking the diffraction resolution limit by stimulated emission: stimulated-emission-depletion fluorescence microscopy,” *Opt. Lett.* **19**, 780 (1994).
- [4] E. Betzig, “Proposed method for molecular optical imaging,” *Opt. Lett.* **20**, 237 (1995).
- [5] W. E. Moerner, “New Directions in Single-Molecule Imaging and Analysis,” *Proc. Natl. Acad. Sci. U.S.A.* **104**, 12596 (2007).
- [6] S. W. Hell, “Far-Field Optical Nanoscopy,” *Science* **316**, 1153 (2007).
- [7] E. Betzig, G.H. Patterson, R. Sougrat, O. W. Lindwasser, S. Olenych, J. S. Bonifacino, M. W. Davidson, J. Lippincott-Schwartz, and H. F. Hess, “Imaging Intracellular Fluorescent Proteins at Nanometer Resolution,” *Science* **313**, 1642 (2006).
- [8] C. Rushforth and R. Harris, “Restoration, resolution, and noise,” *J. Opt. Soc. Am.* **58**, 539-545 (1968).
- [9] M. Bertero and C. De Mol, “Superresolution by data inversion,” *Progress in Optics* **XXXVI**, 129-178 (1996).
- [10] L. Lucy, “Statistical limits to superresolution,” *Astron. Astrophys.* **261**, 706-710 (1992).

References

- [11] M. Shahram and P. Milanfar, “Imaging below the diffraction limit: a statistical analysis,” *IEEE Trans. Image Process.* **13**, 677-689 (2004).
- [12] S. Ram, E. Sally Ward, and R. Ober, “Beyond Rayleigh’s criterion: a resolution measure with application to single-molecule microscopy,” *Proc. Natl. Acad. Sci. USA* **103**, 4457-4462 (2006).
- [13] S. Prasad, “Asymptotics of Bayesian error probability and 2D pair superresolution,” *Opt. Express* **22**, 16029-16048 (2014).
- [14] H. Van Trees, *Detection, Estimation, and Modulation Theory, Part I* (Wiley, 1968), Chap.2.
- [15] S. Kay, *Fundamentals of Statistical Signal Processing: I. Estimation Theory* (Prentice Hall, 1993), Chap.3.
- [16] E. Bettens, D. Van Dyck, A. Den Dekker, J. Sijbers, and A. Van den Bos, “Model-based two-object resolution from observations having counting statistics,” *Ultramicroscopy* **77**, 37-48 (1999)
- [17] S. Ram, E. S. Ward, and R. J. Ober, “Beyond Rayleigh’s criterion: a resolution measure with application to single-molecule microscopy,” *Proc. Natl. Acad. Sci. U. S. A.* **103**, 4457-4462 (2006).
- [18] M. Tsang, R. Nair, and X.-M. Lu, “Quantum Theory of Superresolution for Two Incoherent Optical Point Sources,” *Phys. Rev. X* **6**, 031033 (2016).
- [19] C. Helstrom, *Quantum Detection and Estimation Theory* (Academic Press, 1976), vol. 123.
- [20] S. Braunstein and C. Caves, “Statistical distance and the geometry of quantum states,” *Phys. Rev. Lett.* **72**, 3439-3443 (1994).
- [21] M. Paris, “Quantum estimation for quantum technology,” *Int. J. Quant. Inform.* **7**, 125-137 (2009).
- [22] M. Szczykulska, T. Baumgraz, and A. Dutta, “Multi-parameter quantum metrology,” *Adv. Physics X*, vol. 1, 621-639 (2016).
- [23] D. Safranek, “Simple expression for the quantum Fisher information matrix,” arXiv: 1801.00945 [quant-ph] (2018).
- [24] R. Nair and M. Tsang, “Far-field superresolution of thermal electromagnetic sources at the quantum limit,” *Phys. Rev. Lett.* **117**, 190801 (2016).

References

- [25] C. Lupo and S. Pirandola, “Ultimate precision bound of quantum and sub-wavelength imaging,” *Phys. Rev. Lett.* **117**, 190802 (2016).
- [26] F. Yang, R. Nair, M. Tsang, C. Simon, and A. Lvovsky, “Fisher information for far-field linear optical superresolution via homodyne or heterodyne detection in a higher-order local oscillator mode,” *Physical Review A* **96**, 063829 (2017).
- [27] S. Ang, R. Nair, and M. Tsang, “Quantum limit for two-dimensional resolution of two incoherent optical point sources,” *Phys. Rev. A* **95**, 063847 (2017).
- [28] M. Paur, B. Stoklasa, Z. Hradil, L. Sanchez-Soto, and J. Rehacek, “Achieving the ultimate optical resolution,” *Optica* **10**, 1144-1147 (2016).
- [29] Z. S. Tang, K. Durak, and A. Ling, “Fault-tolerant and finite-error localization for point emitters within the diffraction limit,” *Opt. Express* **24**, 22004-22012 (2016).
- [30] F. Yang, A. Taschilina, E. S. Moiseev, C. Simon, and A. I. Lvovsky, “Far-field linear optical superresolution via heterodyne detection in a higher-order local oscillator mode,” *Optica* **3**, 1148-1152 (2016).
- [31] W. K. Tham, H. Ferretti, and A. M. Steinberg, “Beating Rayleigh’s Curse by Imaging Using Phase Information,” *Phys. Rev. Lett.* **118**, 070801 (2017).
- [32] J. Rehacek, Z. Hradil, B. Stoklasa, M. Paur, J. Grover, A. Krzic, and L. L. Sanchez-Soto, “Multiparameter quantum metrology of incoherent point sources: Towards realistic superresolution,” *Phys. Rev. A.* **96**, 062107 (2017).
- [33] J. Rehacek, Z. Hradil, D. Koutny, J. Grover, A. Krzic, and L. L. Sanchez-Soto, “Optimal measurements for quantum spatial superresolution,” *Phys. Rev. A.* **98**, 012013 (2018).
- [34] M. Tsang, “Subdiffraction incoherent optical imaging via spatial-mode demultiplexing,” *New J. Phys.* **19**, 023054 (2017).
- [35] M. Tsang, “Subdiffraction incoherent optical imaging via spatial-mode demultiplexing: Semiclassical treatment,” *Phys. Rev. A.* **97**, 023830 (2018).
- [36] M. Tsang, “Conservative classical and quantum resolution limits for incoherent imaging,” *J. Mod. Opt.* **65**, 1385 (2018).
- [37] R. Kerviche, S. Guha, and A. Ashok, Fundamental limit of resolving two point sources limited by an arbitrary point spread function, in *Proceedings of the 2017 IEEE International Symposium on Information Theory (ISIT)* (IEEE, New York, 2017), pp. 441-445.

References

- [38] A. Chrostowski, R. Demkowicz-Dobrzanski, M. Jarzyna, and K. Banaszek, “On super-resolution imaging as a multiparameter estimation problem,” *Int. J. Quantum. Inform.* **15**, 1740005 (2017).
- [39] M. Backlund, Y. Shechtman, and R. Walsworth, “Fundamental precision bounds for three-dimensional optical localization microscopy with Poisson statistics,” *Phys. Rev. Lett.* **121**, 023904 (2018).
- [40] G. Shtengel, J. A. Galbraith, C. G. Galbraith, J. Lippincott-Schwartz, J. M. Gillette, S. Manley, R. Sougrat, C. M. Waterman, P. Kanchanawong, M. W. Davidson, R. D. Fetter, and H. F. Hess, “Interferometric fluorescent super-resolution microscopy resolves 3D cellular ultrastructure,” *Proc. Natl. Acad. Sci. USA* **106**, 3125-3130 (2009).
- [41] S. Pavani and R. Piestun, “Three dimensional tracking of fluorescent microparticles using a photon-limited double-helix response system,” *Opt. Express* **16**, 22048-22057 (2008).
- [42] M. Lew, S. Lee, M. Badieirostami, and W. Moerner, “Corkscrew point spread function for far-field three-dimensional nanoscale localization of pointlike objects,” *Opt. Lett.* **36**, 202-204 (2011).
- [43] S. Prasad, “Rotating point spread function via pupil-phase engineering,” *Opt. Lett.* **38**, 585-587 (2013).
- [44] Z. Yu and S. Prasad, “High-numerical-aperture microscopy with a rotating point spread function,” *J. Opt. Soc. Am. A* **33**, B58-B69 (2016).
- [45] B. Huang, W. Wang, M. Bates, and X. Zhuang, “Three-dimensional super-resolution imaging by stochastic optical reconstruction microscopy,” *Science* **319**, 810-813 (2008).
- [46] S. Ram, P. Prabhat, J. Chao, E. Ward, and R. Ober, “High accuracy 3D quantum dot tracking with multifocal plane microscopy for the study of fast intracellular dynamics in live cells,” *Biophys. J.* **95**, 6025-6043 (2008).
- [47] M. F. Juetten, T. J. Gould, M. D. Lessard, M. J. Mlodzianoski, B. S. Nagpure, B. T. Bennett, S. T. Hess, and J. Bewersdorf, “Three-dimensional sub-100 nm resolution fluorescence microscopy of thick samples,” *Nat. Methods* **5**, 527 (2008).
- [48] Z. Yu and S. Prasad, “Quantum Limited Superresolution of an Incoherent Source Pair in Three Dimensions,” *Phys. Rev. Lett.* **121**, 180504 (2018).
- [49] J. Goodman, *Introduction to Fourier Optics*, 4th edition (Freeman, 2017), Chap. 6.

References

- [50] R. Noll, "Zernike polynomials and atmospheric turbulence," *J. Opt. Soc. Am.* **66**, 207-211 (1976).
- [51] G. Turin, "An introduction to matched filters," *IRE Trans. Inform. Th.* **6**, 311-329 (1960).

Chapter 5

Quantum Limited 3D pair Super-localization and Super-resolution

5.1 Introduction

In the previous Chapter we extended the analysis of quantum limited estimation of the separation of a pair of equally bright incoherent point sources from one and two transverse dimensions to include the third, axial dimension, when the centroid of the pair is well located in advance. The quantum limit on the variance of unbiased estimation of the three-dimensional (3D) separation vector, as determined by the inverse of the QFI matrix [1, 2, 3], can be simply expressed in terms of the correlation of the wavefront phase gradients in the imaging aperture. Because of the linearity of the wavefront phase with respect to (w.r.t) the pair-separation vector, the QFI matrix and its inverse, QCRB, both have constant values independent of the separation of the sources.

In this Chapter we will extend our work further to the more realistic situation that the 3D centroid location of the source pair along with their 3D separation are both unknown and need to be estimated. We will calculate the 6×6 QFI matrix and the corresponding QCRB for joint estimation of the 3D position of the centroid and the separation of a pair of equally bright sources. We will then discuss the fundamental estimation-theoretic tradeoffs between the two tasks of centroid and separation estimations. We will also discuss the impact of centroid localization uncertainty on the classical wavefront projection approach to realize quantum limited estimation of the pair separation vector. The main work in this Chapter was published in Ref. [4].

5.2 QFI for Jointly Estimating the Centroid and the Separation of a Pair of Incoherent Point Sources with Equal Brightness

As we saw in the previous Chapter, the QFI matrix, \mathbf{H} , is defined to have elements $H_{\mu\nu} \stackrel{\text{def}}{=} \text{ReTr} (\hat{\rho} \hat{L}_\mu \hat{L}_\nu)$, where the density operator $\hat{\rho}$ has the form,

$$\hat{\rho} = \frac{1}{2} \left(|\tilde{K}_+\rangle\langle\tilde{K}_+| + |\tilde{K}_-\rangle\langle\tilde{K}_-| \right), \quad (5.1)$$

for a photon emitted by two incoherent point sources with equal brightness and captured by the imaging aperture. The six parameters, l_x, l_y, l_z and s_x, s_y, s_z of interest in this Chapter are the three Cartesian components of the normalized pair-semi-separation and pair-centroid position vectors, $\boldsymbol{\ell}$ and \mathbf{s} , respectively. Here \mathbf{s} is defined in the same way as $\boldsymbol{\ell}$ is in previous Chapter. The two pure single-photon states, $|\tilde{K}_\pm\rangle$, are emitted by the two point sources located at $\mathbf{s} \pm \boldsymbol{\ell}$, respectively. The corresponding normalized wavefunctions have the following representations over the

aperture (see Appendix G):

$$\begin{aligned} \langle \mathbf{u} | \tilde{K}_\pm \rangle &= \exp(\pm i\phi_0) P(\mathbf{u}) \exp(-i2\pi \mathbf{s}_\perp \cdot \mathbf{u} - i\pi s_z u^2) \\ &\quad \times \exp[\mp i\Psi(\mathbf{u}; \boldsymbol{\ell})], \end{aligned} \quad (5.2)$$

in which $P(\mathbf{u})$ is a general pupil function obeying the normalization condition,

$$\int d^2u |P(\mathbf{u})|^2 = 1, \quad (5.3)$$

the phase function, $\Psi(\mathbf{u}; \boldsymbol{\ell})$, has the form,

$$\Psi(\mathbf{u}; \boldsymbol{\ell}) = 2\pi \mathbf{u} \cdot \mathbf{l}_\perp + \pi u^2 l_z, \quad (5.4)$$

and the phase constant, ϕ_0 , is properly chosen to make the inner product, $\Delta \stackrel{\text{def}}{=} \langle \tilde{K}_- | \tilde{K}_+ \rangle$, real, as before. In view of relations (5.2) and (5.4) for the wavefunction and Ψ , this inner product may be expressed as

$$\Delta = \exp(-2i\phi_0) \int d^2u |P(\mathbf{u})|^2 \exp(i4\pi \mathbf{l}_\perp \cdot \mathbf{u} + i2\pi l_z u^2), \quad (5.5)$$

which like the phase constant, ϕ_0 , is independent of the centroid position vector, \mathbf{s} . For the clear, unit-radius circular aperture, $P(\mathbf{u})$ is simply $1/\sqrt{\pi}$ times the indicator function for the aperture.

The QFI matrix elements for only estimating the separation parameters, when the centroid position is perfectly known in advance, were shown in the previous Chapter to be,

$$H_{\mu\nu}^{(l)} = 4 [\langle \partial_\mu^{(l)} \Psi \partial_\nu^{(l)} \Psi \rangle - \langle \partial_\mu^{(l)} \Psi \rangle \langle \partial_\nu^{(l)} \Psi \rangle], \quad (5.6)$$

where angular brackets here denote weighted aperture averages, with $|P(\mathbf{u})|^2$ being the weight function.

The minimum error of simultaneously estimating $\boldsymbol{\ell}$ and \mathbf{s} is given by the inverse of a 6×6 QFI matrix of which $\mathbf{H}^{(l)}$ given by expression (5.6) may be regarded as a

3×3 diagonal block. The full QFI matrix may be organized as a collection of four 3×3 blocks,

$$\mathbf{H} = \left(\begin{array}{c|c} \mathbf{H}^{(ll)} & \mathbf{H}^{(ls)} \\ \hline \mathbf{H}^{(sl)} & \mathbf{H}^{(ss)} \end{array} \right), \quad (5.7)$$

with matrix elements defined as

$$\begin{aligned} H_{\mu\nu}^{(ab)} &= H_{\nu\mu}^{(ba)} \\ &= \text{ReTr} (\hat{\rho} \hat{L}_\mu^{(a)} \hat{L}_\nu^{(b)}); \quad a, b = l, s; \quad \mu, \nu = x, y, z. \end{aligned} \quad (5.8)$$

The remaining matrix elements, $H_{\mu\nu}^{(ls)}, H_{\mu\nu}^{(ss)}$, follow from their general form,

$$\begin{aligned} H_{\mu\nu}^{(ab)} &= \sum_{i=\pm} \frac{1}{e_i} \partial_\mu^{(a)} e_i \partial_\nu^{(b)} e_i \\ &+ 4\text{Re} \sum_{i=\pm} \frac{1}{e_i} (\partial_\mu^{(a)} \langle e_i |) (\hat{\rho} - e_i \hat{I})^2 \partial_\nu^{(b)} |e_i\rangle \\ &+ 4\Delta^2 \text{Re} \sum_{i \neq j} \left(\frac{1}{e_i} - e_i \right) \langle e_i | \partial_\mu^{(a)} |e_j\rangle \langle e_j | \partial_\nu^{(b)} |e_i\rangle, \end{aligned} \quad (5.9)$$

in which $\partial_\mu^{(l)} \stackrel{\text{def}}{=} \partial/\partial l_\mu$ and $\partial_\mu^{(s)} \stackrel{\text{def}}{=} \partial/\partial s_\mu$ denote partial derivatives w.r.t. l_μ and s_μ , respectively, and \hat{I} is the identity operator. The eigenvalues, e_\pm , and associated orthonormal eigenstates, $|e_\pm\rangle$, are easily derived,

$$e_\pm = \frac{1 \pm \Delta}{2}, \quad |e_\pm\rangle = \frac{1}{\sqrt{2(1 \pm \Delta)}} \left(|\tilde{K}_+\rangle \pm |\tilde{K}_-\rangle \right). \quad (5.10)$$

Since $\hat{\rho} = e_+ |e_+\rangle \langle e_+| + e_- |e_-\rangle \langle e_-|$, we may write

$$\begin{aligned} (\hat{\rho} - e_+ \hat{I}) \partial_\nu |e_+\rangle &= e_+ [|e_+\rangle \langle e_+ | \partial_\nu |e_+\rangle - \partial_\nu |e_+\rangle] \\ &+ e_- |e_-\rangle \langle e_- | \partial_\nu |e_+\rangle, \end{aligned} \quad (5.11)$$

in which ∂_ν denotes a partial derivative w.r.t. any of the six parameters being estimated. Multiplying Eq. (5.11) by its Hermitian adjoint (h.a.) on the left, with ν replaced by μ in the latter, we reach one of the two inner products in the second

sum of Eq. (5.9). Two of the nine terms of which this product is comprised vanish due to the orthogonality relation, $\langle e_+ | e_- \rangle = 0$. Two other terms cancel out exactly, and the remaining five combine neatly into a set of three distinct terms,

$$\begin{aligned} (\partial_\mu \langle e_+ |) (\hat{\rho} - e_+ \hat{I})^2 \partial_\nu | e_+ \rangle &= -(e_-^2 - 2e_+ e_-) \langle e_+ | \partial_\mu | e_- \rangle \\ &\times \langle e_- | \partial_\nu | e_+ \rangle + e_+^2 \langle e_+ | \partial_\mu | e_+ \rangle \langle e_+ | \partial_\nu | e_+ \rangle \\ &+ e_+^2 (\partial_\mu \langle e_+ |) \partial_\nu | e_+ \rangle. \end{aligned} \quad (5.12)$$

Noting that $\hat{\rho}$ is formally invariant under an interchange of the + and - subscripts in relation (5.12), we have

$$\begin{aligned} (\partial_\mu \langle e_- |) (\hat{\rho} - e_- \hat{I})^2 \partial_\nu | e_- \rangle &= -(e_+^2 - 2e_+ e_-) \langle e_- | \partial_\mu | e_+ \rangle \\ &\times \langle e_+ | \partial_\nu | e_- \rangle + e_-^2 \langle e_- | \partial_\mu | e_- \rangle \langle e_- | \partial_\nu | e_- \rangle \\ &+ e_-^2 (\partial_\mu \langle e_- |) \partial_\nu | e_- \rangle. \end{aligned} \quad (5.13)$$

Since Δ does not depend on \mathbf{s} , taking the partial derivative of $|e_+\rangle$, given by expression (5.10), w.r.t. any component of \mathbf{s} , and taking the inner product of the resulting expression with the bra $\langle e_\pm |$, obtained by taking the h.a. of expression (5.10), gives the identities:

$$\begin{aligned} \langle e_+ | \partial_\mu^{(s)} | e_+ \rangle &= \frac{\langle \tilde{K}_+ | \partial_\mu^{(s)} | \tilde{K}_+ \rangle + i \text{Im} \langle \tilde{K}_+ | \partial_\mu^{(s)} | \tilde{K}_- \rangle}{(1 + \Delta)}; \\ \langle e_- | \partial_\mu^{(s)} | e_+ \rangle &= \frac{\text{Re} \langle \tilde{K}_+ | \partial_\mu^{(s)} | \tilde{K}_- \rangle}{\sqrt{1 - \Delta^2}}. \end{aligned} \quad (5.14)$$

To arrive at these identities, we utilized the relations, $\langle \tilde{K}_+ | \partial_\mu^{(s)} | \tilde{K}_+ \rangle = \langle \tilde{K}_- | \partial_\mu^{(s)} | \tilde{K}_- \rangle$ and $\langle \tilde{K}_+ | \partial_\mu^{(s)} | \tilde{K}_- \rangle = -\langle \tilde{K}_- | \partial_\mu^{(s)} | \tilde{K}_+ \rangle^*$, that follow from form (5.2) of the states $|\tilde{K}_\pm\rangle$.

The identities,

$$\langle e_+ | \partial_\mu^{(l)} | e_+ \rangle = 0, \quad \langle e_- | \partial_\mu^{(l)} | e_+ \rangle = \frac{1}{\sqrt{1 - \Delta^2}} \langle \tilde{K}_+ | \partial_\mu | \tilde{K}_+ \rangle, \quad (5.15)$$

proved similarly in the previous chapter, and four more obtained by the interchange of $|e_+\rangle$ and $|e_-\rangle$ in Eqs. (5.14) and (5.15), which entails the substitutions $|\tilde{K}_\pm\rangle \rightarrow \pm|\tilde{K}_\pm\rangle$

and $\Delta \rightarrow -\Delta$ according to expressions (5.10) for $|e_{\pm}\rangle$, namely

$$\begin{aligned}\langle e_-|\partial_{\mu}^{(s)}|e_- \rangle &= \frac{\langle \tilde{K}_+|\partial_{\mu}^{(s)}|\tilde{K}_+ \rangle - i\text{Im}\langle \tilde{K}_+|\partial_{\mu}^{(s)}|\tilde{K}_- \rangle}{(1 - \Delta)}; \\ \langle e_+|\partial_{\mu}^{(s)}|e_- \rangle &= -\frac{\text{Re}\langle \tilde{K}_+|\partial_{\mu}^{(s)}|\tilde{K}_- \rangle}{\sqrt{1 - \Delta^2}},\end{aligned}\quad (5.16)$$

and

$$\langle e_-|\partial_{\mu}^{(l)}|e_- \rangle = 0, \quad \langle e_+|\partial_{\mu}^{(l)}|e_- \rangle = \frac{1}{\sqrt{1 - \Delta^2}}\langle \tilde{K}_+|\partial_{\mu}|\tilde{K}_+ \rangle, \quad (5.17)$$

comprise the full set of identities that can simplify expression (5.9) for the elements of the blocks $\mathbf{H}^{(sl)}$ and $\mathbf{H}^{(ss)}$.

5.2.1 Vanishing of the Off-diagonal QFI Block, $\mathbf{H}^{(sl)}$

Since e_{\pm} are independent of \mathbf{s} , it follows that the first sum on the right hand side in expression (5.9) vanishes identically, while the other two sums may be combined into one in view of expressions (5.12) and (5.13) for the two terms of the second sum. Using the identities, $e_{\mp}^2 - 2e_+e_- = \Delta^2 - e_{\pm}^2$, we may thus obtain the following expression for the matrix elements of the off-diagonal block $\mathbf{H}^{(sl)}$:

$$H_{\mu\nu}^{(sl)} = 4(1 - \Delta^2)\text{Re} \sum_{i \neq j} e_i \langle e_i|\partial_{\mu}^{(s)}|e_j \rangle \langle e_j|\partial_{\nu}^{(l)}|e_i \rangle + 4\text{Re} \sum_{i=\pm} e_i (\partial_{\mu}^{(s)} \langle e_i|) \partial_{\nu}^{(l)} |e_i \rangle. \quad (5.18)$$

From identities (5.14)-(5.17), we see that $\langle e_{\pm}|\partial_{\mu}^{(s)}|e_{\mp} \rangle$ are real, while $\langle e_{\pm}|\partial_{\nu}^{(l)}|e_{\mp} \rangle$ are purely imaginary, since $\langle \tilde{K}_+|\partial_{\mu}^{(l)}|\tilde{K}_+ \rangle$ is purely imaginary due to the form (5.2) of the wavefunctions. Consequently, the first term in expression (5.18) vanishes identically.

Using form (5.10) of the eigenstates and noting that Δ is independent of the

centroid position vector \mathbf{s} , we have

$$\begin{aligned}\partial_\mu^{(s)}\langle e_\pm| &= \frac{1}{\sqrt{2(1\pm\Delta)}} \left(\partial_\mu^{(s)}\langle \tilde{K}_+| \pm \partial_\mu^{(s)}\langle \tilde{K}_-| \right); \\ \partial_\nu^{(l)}|e_\pm\rangle &= \mp \frac{\partial_\nu^{(l)}\Delta}{2(1\pm\Delta)}|e_\pm\rangle + \frac{1}{\sqrt{2(1\pm\Delta)}} \left(\partial_\nu^{(l)}|\tilde{K}_+\rangle \pm \partial_\nu^{(l)}|\tilde{K}_-\rangle \right).\end{aligned}\quad (5.19)$$

Taking the inner product of the above two states, multiplying the product by $e_\pm = (1\pm\Delta)/2$, and then adding the two terms that result corresponding to the upper and lower signs, we may express the second sum in Eq. (5.18), as

$$\begin{aligned}\sum_{i=\pm} e_i(\partial_\mu^{(s)}\langle e_i|)\partial_\nu^{(l)}|e_i\rangle &= \frac{1}{2} \left[(\partial_\mu^{(s)}\langle \tilde{K}_+|)\partial_\nu^{(l)}|\tilde{K}_+\rangle + (\partial_\mu^{(s)}\langle \tilde{K}_-|)\partial_\nu^{(l)}|\tilde{K}_-\rangle \right] \\ &\quad - \frac{\partial_\nu^{(l)}\Delta}{4} \left[(\partial_\mu^{(s)}\langle e_+|)|e_+\rangle - (\partial_\mu^{(s)}\langle e_-|)|e_-\rangle \right],\end{aligned}\quad (5.20)$$

where the terms inside the second bracket follow from the expression for $\partial_\mu^{(s)}\langle e_\pm|$ given in Eq. (5.19). From the form of the wavefunctions (5.2), it follows that the two terms inside the first bracket on the RHS of Eq. (5.20) are exactly negative of each other, so their sum vanishes, which simplifies Eq. (5.20) to the form

$$\sum_{i=\pm} e_i(\partial_\mu^{(s)}\langle e_i|)\partial_\nu^{(l)}|e_i\rangle = -\frac{\partial_\nu^{(l)}\Delta}{4} \left[(\partial_\mu^{(s)}\langle e_+|)|e_+\rangle - (\partial_\mu^{(s)}\langle e_-|)|e_-\rangle \right].\quad (5.21)$$

Since $\langle e_\pm|e_\pm\rangle = 1$, we have the identity, $\partial_\mu^{(s)}(\langle e_\pm|e_\pm\rangle) = 0$, which from the product rule of differentiation is equivalent to the relation,

$$(\partial_\mu^{(s)}\langle e_\pm|)|e_\pm\rangle = -\langle e_\pm|\partial_\mu^{(s)}|e_\pm\rangle.\quad (5.22)$$

Using the complex-conjugation property of the inner product, we may write the left-hand side of Eq. (5.22) as $\langle e_\pm|\partial_\mu^{(s)}|e_\pm\rangle^*$, which when equated to its RHS implies that $(\partial_\mu^{(s)}\langle e_\pm|)|e_\pm\rangle$ is purely imaginary. Consequently, expression (5.21) is purely imaginary, and thus $H_{\mu\nu}^{(sl)}$, which is the proportional to its real part, vanishes identically,

$$H_{\mu\nu}^{(sl)} = 0.\quad (5.23)$$

There is no increase of the minimum error of unbiased joint estimation of the pair centroid-location and separation vectors over that of unbiased independent estimation of the two vectors.

5.2.2 Pair-centroid-localization QFI

The matrix elements of the centroid-localization QFI, $\mathbf{H}^{(ss)}$, are given by replacing all $\partial^{(l)}$ by $\partial^{(s)}$ in Eq. (5.18) and then adding the sum, $\sum_{i=\pm} e_i \langle e_i | \partial_\mu^{(s)} | e_i \rangle \langle e_i | \partial_\nu^{(s)} | e_i \rangle$, arising from the non-vanishing second terms on the RHS of Eqs. (5.12) and (5.13),

$$H_{\mu\nu}^{(ss)} = 4(1 - \Delta^2) \text{Re} \sum_{i \neq j} e_i \langle e_i | \partial_\mu^{(s)} | e_j \rangle \langle e_j | \partial_\nu^{(s)} | e_i \rangle + 4 \text{Re} \sum_{i=\pm} e_i [\langle e_i | \partial_\mu^{(s)} | e_i \rangle \langle e_i | \partial_\nu^{(s)} | e_i \rangle + (\partial_\mu^{(s)} \langle e_i |) \partial_\nu^{(s)} | e_i \rangle]. \quad (5.24)$$

The matrix elements, $\langle e_+ | \partial_\mu^{(s)} | e_\pm \rangle$ and $\langle e_- | \partial_\mu^{(s)} | e_\pm \rangle$, were already evaluated earlier in Eqs. (5.14) and (5.16). The remaining matrix elements, $(\partial_\mu^{(s)} \langle e_\pm |) \partial_\nu^{(s)} | e_\pm \rangle$, are obtained by taking appropriate derivatives $|e_\pm\rangle$ in terms of the pure emission states and noting that Δ is independent of all centroid-location coordinates. These matrix elements may thus be expressed as

$$(\partial_\mu^{(s)} \langle e_\pm |) \partial_\nu^{(s)} | e_\pm \rangle = \frac{1}{2(1 \pm \Delta)} \left(\partial_\mu^{(s)} \langle \tilde{K}_+ | \pm \partial_\mu^{(s)} \langle \tilde{K}_- | \right) \left(\partial_\nu^{(s)} | \tilde{K}_+ \rangle \pm \partial_\nu^{(s)} | \tilde{K}_- \rangle \right). \quad (5.25)$$

Since $e_\pm = (1/2)(1 \pm \Delta)$, substituting the last of the matrix elements in Eqs. (5.14) and (5.16) into the first sum in Eq. (5.24) reduces it to the form,

$$4(1 - \Delta^2) \text{Re} \sum_{i \neq j} e_i \langle e_i | \partial_\mu^{(s)} | e_j \rangle \langle e_j | \partial_\nu^{(s)} | e_i \rangle = -4 \text{Re} \langle \tilde{K}_+ | \partial_\mu^{(s)} | \tilde{K}_- \rangle \text{Re} \langle \tilde{K}_+ | \partial_\nu^{(s)} | \tilde{K}_- \rangle. \quad (5.26)$$

Substituting the first of the matrix elements in Eqs. (5.14) and (5.16) into the first part of the second sum on the RHS of Eq. (5.24) and then taking its real part

evaluates it to the form,

$$\begin{aligned}
& 4\text{Re} \sum_{i=\pm} e_i \langle e_i | \partial_\mu^{(s)} | e_i \rangle \langle e_i | \partial_\nu^{(s)} | e_i \rangle \\
&= -\frac{2}{1+\Delta} \left(\text{Im} \langle \tilde{K}_+ | \partial_\mu^{(s)} | \tilde{K}_+ \rangle + \text{Im} \langle \tilde{K}_+ | \partial_\mu^{(s)} | \tilde{K}_- \rangle \right) \left(\text{Im} \langle \tilde{K}_+ | \partial_\nu^{(s)} | \tilde{K}_+ \rangle + \text{Im} \langle \tilde{K}_+ | \partial_\nu^{(s)} | \tilde{K}_- \rangle \right) \\
&\quad - \frac{2}{1-\Delta} \left(\text{Im} \langle \tilde{K}_+ | \partial_\mu^{(s)} | \tilde{K}_+ \rangle - \text{Im} \langle \tilde{K}_+ | \partial_\mu^{(s)} | \tilde{K}_- \rangle \right) \left(\text{Im} \langle \tilde{K}_+ | \partial_\nu^{(s)} | \tilde{K}_+ \rangle - \text{Im} \langle \tilde{K}_+ | \partial_\nu^{(s)} | \tilde{K}_- \rangle \right) \\
&= -\frac{4}{1-\Delta^2} \left(\text{Im} \langle \tilde{K}_+ | \partial_\mu^{(s)} | \tilde{K}_+ \rangle \text{Im} \langle \tilde{K}_+ | \partial_\nu^{(s)} | \tilde{K}_+ \rangle + \text{Im} \langle \tilde{K}_+ | \partial_\mu^{(s)} | \tilde{K}_- \rangle \text{Im} \langle \tilde{K}_+ | \partial_\nu^{(s)} | \tilde{K}_- \rangle \right) \\
&\quad + \frac{4\Delta}{1-\Delta^2} \left(\text{Im} \langle \tilde{K}_+ | \partial_\mu^{(s)} | \tilde{K}_+ \rangle \text{Im} \langle \tilde{K}_+ | \partial_\nu^{(s)} | \tilde{K}_- \rangle + \text{Im} \langle \tilde{K}_+ | \partial_\mu^{(s)} | \tilde{K}_- \rangle \text{Im} \langle \tilde{K}_+ | \partial_\nu^{(s)} | \tilde{K}_+ \rangle \right),
\end{aligned} \tag{5.27}$$

in which we used the fact that $\langle \tilde{K}_\pm | \partial_\mu^{(s)} | \tilde{K}_\pm \rangle$ are purely imaginary quantities. Finally, substituting the matrix element (5.25) into the second part of the second sum in Eq. (5.24) also simplifies it,

$$\begin{aligned}
4\text{Re} \sum_{i=\pm} e_i (\partial_\mu^{(s)} \langle e_i |) \partial_\nu^{(s)} | e_i \rangle &= 2 [(\partial_\mu^{(s)} \langle \tilde{K}_+ |) \partial_\nu^{(s)} | \tilde{K}_+ \rangle + (\partial_\mu^{(s)} \langle \tilde{K}_- |) \partial_\nu^{(s)} | \tilde{K}_- \rangle] \\
&= 4(\partial_\mu^{(s)} \langle \tilde{K}_+ |) \partial_\nu^{(s)} | \tilde{K}_+ \rangle,
\end{aligned} \tag{5.28}$$

in which we used the fact that the matrix elements, $(\partial_\mu^{(s)} \langle \tilde{K}_\pm |) \partial_\nu^{(s)} | \tilde{K}_\pm \rangle$, are both real and equal to each other as both wavefunctions $\langle \mathbf{u} | \tilde{K}_\pm \rangle$ are pure exponential phase functions over the aperture, with an identical dependence on the centroid location vector, \mathbf{s} . Substituting expressions (5.26)-(5.28) into Eq. (5.24) generates the final

expression for the centroid-localization QFI, $\mathbf{H}^{(ss)}$,

$$\begin{aligned}
 H_{\mu\nu}^{(ss)} = & 4 \left[(\partial_\mu^{(s)} \langle \tilde{K}_+ |) \partial_\nu^{(s)} | \tilde{K}_+ \rangle \right. \\
 & \left. - \text{Re} \langle \tilde{K}_+ | \partial_\mu^{(s)} | \tilde{K}_- \rangle \text{Re} \langle \tilde{K}_+ | \partial_\nu^{(s)} | \tilde{K}_- \rangle \right] \\
 & - \frac{4}{1 - \Delta^2} \left(\text{Im} \langle \tilde{K}_+ | \partial_\mu^{(s)} | \tilde{K}_+ \rangle \text{Im} \langle \tilde{K}_+ | \partial_\nu^{(s)} | \tilde{K}_+ \rangle \right. \\
 & \left. + \text{Im} \langle \tilde{K}_+ | \partial_\mu^{(s)} | \tilde{K}_- \rangle \text{Im} \langle \tilde{K}_+ | \partial_\nu^{(s)} | \tilde{K}_- \rangle \right) \\
 & + \frac{4\Delta}{1 - \Delta^2} \left(\text{Im} \langle \tilde{K}_+ | \partial_\mu^{(s)} | \tilde{K}_+ \rangle \text{Im} \langle \tilde{K}_+ | \partial_\nu^{(s)} | \tilde{K}_- \rangle \right. \\
 & \left. + \text{Im} \langle \tilde{K}_+ | \partial_\nu^{(s)} | \tilde{K}_+ \rangle \text{Im} \langle \tilde{K}_+ | \partial_\mu^{(s)} | \tilde{K}_- \rangle \right). \tag{5.29}
 \end{aligned}$$

In Eq. (5.29), all matrix elements involving only $|\tilde{K}_+\rangle$ and its derivatives, but not $|\tilde{K}_-\rangle$, are easily evaluated as simple aperture averages of powers of aperture coordinates, while the matrix element $\langle \tilde{K}_+ | \partial_\mu^{(s)} | \tilde{K}_- \rangle$ may be evaluated in the aperture plane using the wavefunctions (5.2) and Δ given by relation (5.5),

$$\begin{aligned}
 \langle \tilde{K}_+ | \partial_\mu^{(s)} | \tilde{K}_- \rangle &= -\frac{\exp(-i2\phi_0)}{2\pi} \int_A d^2u \\
 &\quad \times \partial_\mu^{(l)} [\exp(4i\pi\mathbf{u} \cdot \mathbf{l}_\perp + 2i\pi u^2 l_z)] \\
 &= -\frac{\Delta \int_A d^2u \partial_\mu^{(l)} [\exp(4i\pi\mathbf{u} \cdot \mathbf{l}_\perp + 2i\pi u^2 l_z)]}{2 \int_A d^2u \exp(4i\pi\mathbf{u} \cdot \mathbf{l}_\perp + 2i\pi u^2 l_z)}. \tag{5.30}
 \end{aligned}$$

Eq. (5.29) for the QFI matrix elements for estimating the centroid location coordinates alone is independent of those coordinates. This is fundamentally a consequence of the global translational invariance of a shift-invariant imager, as the centroid location vector, \mathbf{s} , can be changed by an arbitrary additive constant vector by a mere change of the origin of the coordinate system, under which the pair separation vector, $\boldsymbol{\ell}$, is invariant. Physically speaking, an axial refocusing and a transverse alignment of the imager are all that are needed to place the pair centroid at the origin in the source space, an action that cannot affect the fidelity with which the centroid can be estimated. This QFI depends only on $\boldsymbol{\ell}$ through Δ and certain aperture integrals.

The off-diagonal elements of the $\mathbf{H}^{(ss)}$ block do not vanish, which reflects the interdependence of the errors of estimating the three coordinates of the pair centroid location when estimating them simultaneously. This is in sharp contrast to the three components of the pair-separation vector, which can be estimated independently of each other.

Since the overall QFI matrix (5.7) is block diagonal, its inverse is obtained by inverting each diagonal block,

$$\mathbf{H}^{-1} = \left(\begin{array}{c|c} (\mathbf{H}^{(ll)})^{-1} & \mathbf{0} \\ \hline \mathbf{0} & (\mathbf{H}^{(ss)})^{-1} \end{array} \right), \quad (5.31)$$

in which $(\mathbf{H}^{(ll)})^{-1}$ has the value,

$$(\mathbf{H}^{(ll)})^{-1} = \begin{pmatrix} \frac{1}{4\pi^2} & 0 & 0 \\ 0 & \frac{1}{4\pi^2} & 0 \\ 0 & 0 & \frac{3}{\pi^2} \end{pmatrix}. \quad (5.32)$$

5.3 Numerical Evaluation of Pair-Centroid QCRB

For the case of clear circular aperture, we numerically evaluated the elements (5.29) of the QFI matrix $\mathbf{H}^{(ss)}$ and then inverted it to compute the values of QCRB for estimating the centroid location coordinates. In Fig. 5.1, we plot QCRB for estimating s_x vs l_x for a number of different values of the other transverse component of the pair-separation vector, namely l_y . The curves start out close to the source-localization QCRB of $1/(4\pi^2) \approx 0.0253$ when the two sources are close to each other and thus approximate a single source. They also asymptote toward the same QCRB value for large separations, since in this limit sources can be localized individually and their centroid thus determined to the same precision as their individual positions. For intermediate values of l_x , the minimum error variance for estimating s_x

is increased due to the image blur caused by a finite aperture size when the sources are transversely not well separated on the Abbe-Rayleigh scale, $l_{\perp} \lesssim 0.25$. Changing l_z , the axial separation of the pair, from a small value of 0.025 to 0.25 does not improve the s_x estimation error significantly, as seen in the small difference between the curves in the left and right panels. Because of perfect $x \leftrightarrow y$ symmetry for a circular aperture, an identical behavior was confirmed by our numerical evaluation of QCRB for the estimation of s_y vs. l_y .

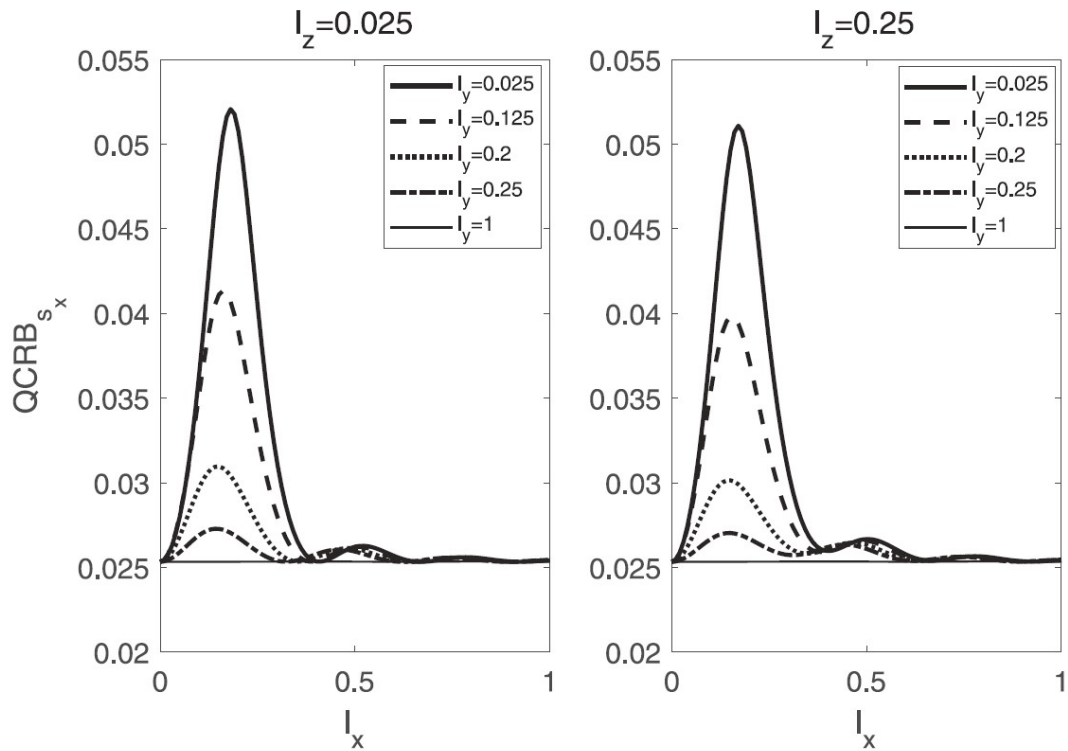


Figure 5.1: Plots of QCRB for s_x vs. l_x for various values of l_y and for two different values of l_z , namely 0.025 (left panel) and 0.25 (right panel). Image taken from Ref. [4].

In Fig. 5.2, we display QCRB for estimating s_x vs. l_y . As expected, with increasing l_y , the minimum error variance for estimating s_x decreases as the sources get farther apart in the orthogonal direction. Once again, as the sources get well

separated, when either l_x or l_y or both become large, the minimum error variance for locating the pair centroid in the transverse plane approaches the localization QCRB, namely 0.0253. The relative vertical positions of the curves for different values of l_x are consistent with the peaks seen in Fig. 5.1.

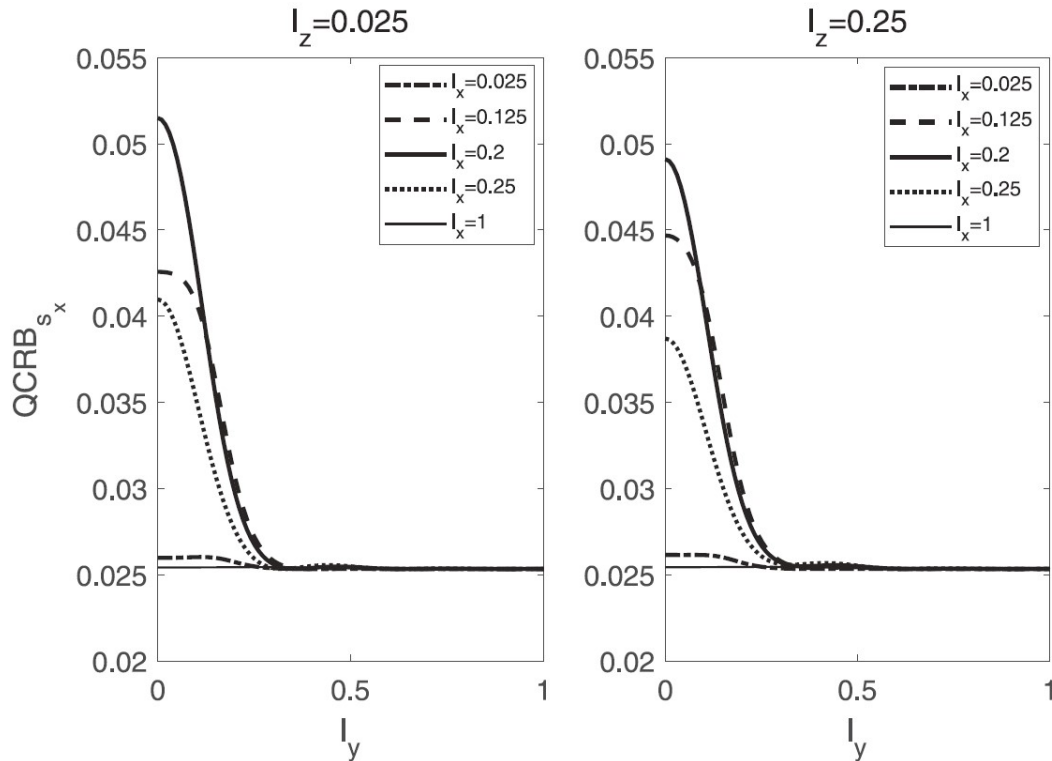


Figure 5.2: Plots of QCRB for s_x vs. l_y for two different values of l_z , namely 0.025 (left panel) and 0.25 (right panel). Image taken from Ref. [4].

In Fig. 5.3, we plot QCRB for estimating s_z , the axial coordinate of the pair centroid, as a function of l_z , the axial component of the pair-separation vector. The intrinsic imprecision of estimating the axial coordinate, as reflected in the larger axial-localization QCRB of $3/\pi^2 \approx 0.304$ than the transverse-localization QCRB of 0.0253, is seen in the larger scatter, at the two ends of small and large axial separations, among plots for different values of l_\perp , the transverse separation. Interestingly, there are multiple values of l_z for which QCRB for estimating s_z has minima at the

localization QCRB of 0.304 with increasing l_z . The larger QCRB for s_z than that for s_x or s_y has to do with the quadratic, rather than linear, dependence of the aperture phase on axial coordinates, which implies a lower overall first-order differential sensitivity of wavefront projections to them. This fact also accounts for why the horizontal scale of the plots for axial-coordinate estimation is larger than that for transverse-coordinate estimation plotted in previous figures.

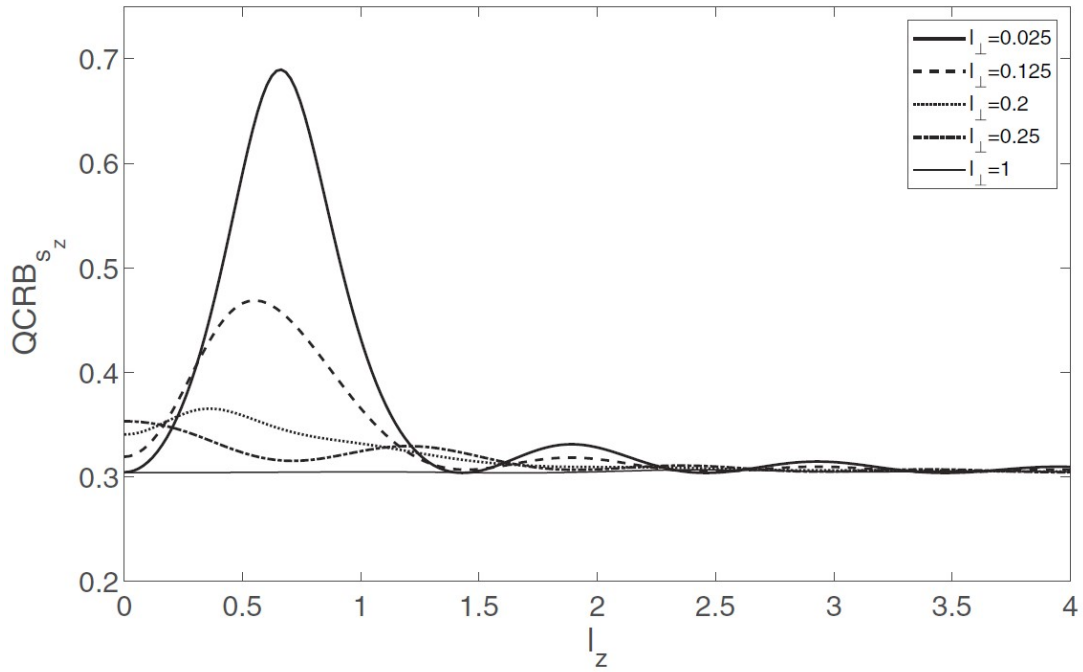


Figure 5.3: Plots of QCRB for s_z vs. l_z for five different values of l_\perp . Image taken from Ref. [4].

5.4 Maximum-Likelihood Estimation of Pair Separation in the Presence of Centroid-Localization Error

For small pair separations, the pair centroid can be localized in full 3D by image based methods to a precision comparable to the corresponding QCRB, but coherent wavefront projections are necessary to attain quantum limited estimation of the pair separation. We envisage a two-arm hybrid experimental approach, similar to that proposed by Tsang *et al.* [5], in which a beam splitter (BS) directs a fraction of photons into one arm in which a 3D localization imager like a rotating-PSF imager [6, 7, 8, 9], an astigmatic imager [10], a multiplane imager [11], or a radial shearing interferometer [12] is placed to simultaneously determine the 3D centroid location of the source pair. The remaining photons pass through a second arm with the same holographic aperture-plane filter as that described in previous Chapter, namely $\sum_n Z_n(\mathbf{u}) \cos \mathbf{q}_n \cdot \mathbf{u}$, in which Z_n denotes the n th Zernike polynomial [13] and \mathbf{q}_n is the transverse offset wavevector of the n th mode.

We show results of a partial simulation of this approach to estimate the pair separation using the maximum-likelihood (ML) estimator described in previous Chapter, subject to a certain centroid localization error achieved in the centroid localization arm and a fixed number, M , of photons in the holographic filter arm. The photons divide into the various pure-Zernike channels according to the probabilities, $\{P_n \stackrel{\text{def}}{=} \langle Z_n | \hat{\rho} | Z_n \rangle \mid n = 1, \dots, N\}$, and into the unmeasured channels with probability, $\bar{P} = 1 - \sum_{n=1}^N P_n$, to yield a multinomial distribution of observed counts from which the ML estimator can extract the separation vector. According to Appendix H, the classical FI matrix elements per photon [14, 15] for estimating the three pair-separation coordinates from the multinomial distribution of counts are given by the

sum,

$$J_{\mu\nu}^{(ll)}/M = \sum_{n=1}^N \frac{(\partial_{\mu}^{(l)} P_n) (\partial_{\nu}^{(l)} P_n)}{P_n} + \frac{(\partial_{\mu}^{(l)} \bar{P}) (\partial_{\nu}^{(l)} \bar{P})}{\bar{P}}, \quad (5.33)$$

which was numerically evaluated for $N = 4$.

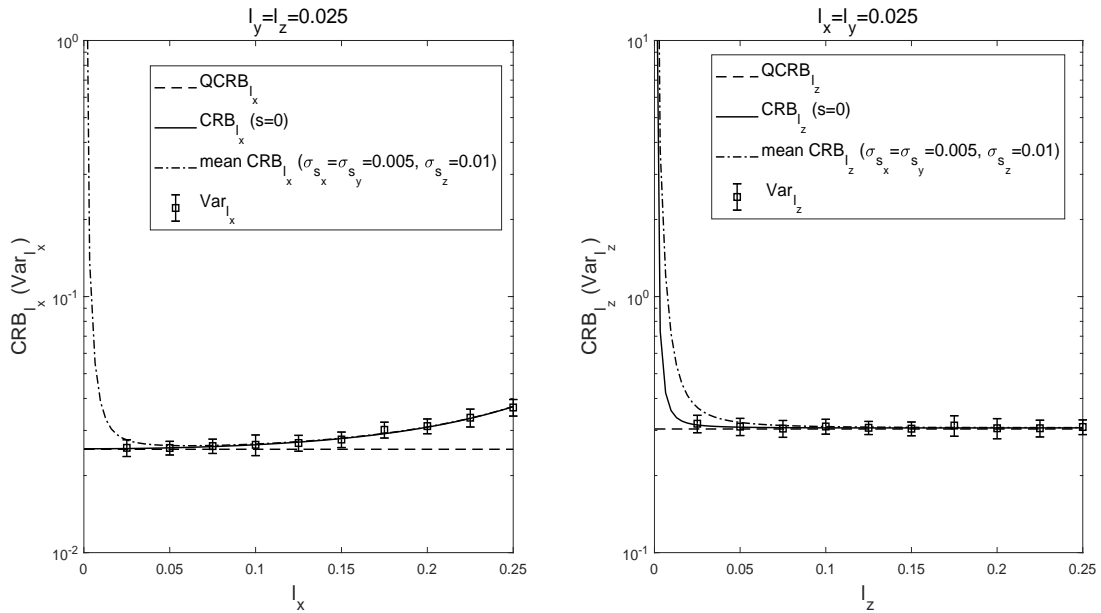


Figure 5.4: (a) Plot of variance of estimation of l_x with changing values of l_x (shown by marker symbols), with the other two l coordinates being equal to 0.025, for $\sigma_{s_x} = \sigma_{s_y} = 0.005$; $\sigma_{s_z} = 0.01$; (b) Same as (a) except $l_x \rightarrow l_z$. Plots of CRBs w.r.t. $l_{x(z)}$ are also shown for comparison. Image taken from Ref. [4].

In Fig. 5.4 (a), we plot the variance of the ML estimation of l_x obtained from a sample of 40 draws of \mathbf{s} from a product-Gaussian statistical distribution with zero means and standard deviations, $\sigma_x^{(s)} = \sigma_y^{(s)} = 0.005$, $\sigma_z^{(s)} = 0.01$, with 400 multinomial data frames for each such \mathbf{s} sample and with 10^6 photons per frame. The mean and standard deviation of these estimation variances over the 40 \mathbf{s} draws are denoted by the square symbols and error bars through them.

The classical CRB, which is the xx diagonal element of the inverse of the FI

matrix (5.33), when averaged over the 40 \mathbf{s} draws, is shown by the dot-dash curve and that for $\mathbf{s} = 0$ by the solid curve in the figure. The results of our ML estimation track well the last curve, since we take $\mathbf{s} = 0$ when extracting the estimates of ℓ from simulated data. The divergence of the dot-dash curve in the limit $l_x \rightarrow 0$ is due to the fact that for $s_x \neq 0$, neither Z_2 nor another pure Zernike mode is an exclusively matched filter [16] for l_x in the limit $l_x \rightarrow 0$. For most of the range of l_x away from 0, however, the four Zernike projections furnish excellent convergence of the variance of the separation estimate based on them to QCRB. Because of the azimuthal symmetry of the optical system and our choice of the Zernikes, the same results as shown in Fig. 5.4 (b) also hold for the estimation of l_y .

In Fig. 5.4 (b), we display analogous curves for estimating the axial separation, l_z . An important difference from the estimation of lateral separation is that all classical CRB curves diverge in the limit $l_z \rightarrow 0$, since no Zernike mode provides an exclusively matched filter for the azimuthally symmetric defocus phase, as we noted in previous Chapter. All CRB curves asymptote toward the QCRB line, however, as l_z grows.

5.5 Conclusions

In this Chapter we have calculated the fundamental quantum bounds represented by QCRB for jointly estimating the centroid location and the separation of a balanced incoherent point source pair in full 3D, extending the analysis of a pure 3D resolution problem with known centroid in previous Chapter.

For a well corrected spatially invariant imaging system, we have shown that the fundamental bounds for estimating the 3D pair-centroid location depend only on pair-separation vector, not the centroid location vector. The quantum bounds for separation estimation remains of the same constant form. By contrast, the quan-

tum bound on the variance for estimating the centroid coordinates is given by a complicated expression that can only numerically be evaluated. These two sets of quantum-estimation bounds - one for the pair centroid coordinates and the other for the pair separation vector - turn out, as we showed, to be statistically independent. This is seen via the block-diagonal form of the QFI for the two sets of coordinates.

We have shown that the classical bounds for estimating the pair separation with wavefront projection, which can saturate the quantum bounds in small separation limits for the case of known centroid, are affected by the uncertainty in the centroid coordinates. We have also presented simulation results for the wavefront-projection approach with Zernike channels for maximum-likelihood estimation of the source separation vector in the presence of finite errors of the pair centroid location. We have seen from these simulations that the quantum-limited minimum error bounds are achievable.

References

- [1] C. Helstrom, *Quantum Detection and Estimation Theory* (Academic Press, 1976), vol. 123.
- [2] S. Braunstein and C. Caves, “Statistical distance and the geometry of quantum states,” *Phys. Rev. Lett.* **72**, 3439-3443 (1994).
- [3] M. Paris, “Quantum estimation for quantum technology,” *Int. J. Quant. Inform.* **7**, 125-137 (2009).
- [4] S. Prasad and Z. Yu, “Quantum-limited superlocalization and superresolution of a source pair in three dimensions,” *Phys. Rev. A* **99**, 022116 (2019).
- [5] M. Tsang, R. Nair, and X.-M. Lu, “Quantum Theory of Superresolution for Two Incoherent Optical Point Sources,” *Phys. Rev. X* **6**, 031033 (2016).
- [6] S. Pavani and R. Piestun, “Three dimensional tracking of fluorescent microparticles using a photon-limited double-helix response system,” *Opt. Express* **16**, 22048-22057 (2008).
- [7] M. Lew, S. Lee, M. Badieirostami, and W. Moerner, “Corkscrew point spread function for far-field three-dimensional nanoscale localization of pointlike objects,” *Opt. Lett.* **36**, 202-204 (2011).
- [8] S. Prasad, “Rotating point spread function via pupil-phase engineering,” *Opt. Lett.* **38**, 585-587 (2013).
- [9] Z. Yu and S. Prasad, “High-numerical-aperture microscopy with a rotating point spread function,” *J. Opt. Soc. Am. A* **33**, B58-B69 (2016).
- [10] B. Huang, W. Wang, M. Bates, and X. Zhuang, “Three-dimensional super-resolution imaging by stochastic optical reconstruction microscopy,” *Science* **319**, 810-813 (2008).

References

- [11] S. Ram, P. Prabhat, J. Chao, E. Ward, and R. Ober, “High accuracy 3D quantum dot tracking with multifocal plane microscopy for the study of fast intracellular dynamics in live cells,” *Biophys. J.* **95**, 6025-6043 (2008).
- [12] M. Backlund, Y. Shechtman, and R. Walsworth, “Fundamental precision bounds for three-dimensional optical localization microscopy with Poisson statistics,” *Phys. Rev. Lett.* **121**, 023904 (2018).
- [13] R. Noll, “Zernike polynomials and atmospheric turbulence,” *J. Opt. Soc. Am.* **66**, 207-211 (1976).
- [14] H. Van Trees, *Detection, Estimation, and Modulation Theory, Part I* (Wiley, 1968), Chap.2.
- [15] S. Kay, *Fundamentals of Statistical Signal Processing: I. Estimation Theory* (Prentice Hall, 1993), Chap.3.
- [16] G. Turin, “An introduction to matched filters,” *IRE Trans. Inform. Th.* **6**, 311-329 (1960).

Chapter 6

Work in Progress, Conclusions and Future Directions

6.1 Work in Progress

6.1.1 Towards More Realistic Quantum Limited 3D Super-localization and Super-resolution: the Unequal Brightness Problem

Our very recent work in progress is to generalize the quantum Fisher information based 3D source-pair super-localization and super-resolution analysis in the last two Chapters to a more realistic scenario that the two incoherent point sources have unequal intensities. The 1D unbalanced source-pair super-localization and super-resolution problem has been discussed by Rehacek *et al.* with real-valued PSF [1, 2]. A careful analysis of this problem is important for any successful attempts to generalize the pair super-resolution problem to super-resolution imaging of extended objects with spatial intensity variations.

Chapter 6. *Work in Progress, Conclusions and Future Directions*

The density operator for a photon emitted by an incoherent pair of unequally bright point sources and passing through an imaging aperture is

$$\hat{\rho} = p_+|\tilde{K}_+\rangle\langle\tilde{K}_+| + p_-|\tilde{K}_-\rangle\langle\tilde{K}_-|, \quad (6.1)$$

where $p_+ + p_- = 1$. The photon wavefunctions are still given by Eq. (5.2) and the phase constant, ϕ_0 , is again chosen to make the inner product, $\Delta \stackrel{\text{def}}{=} \langle\tilde{K}_-|\tilde{K}_+\rangle$, real and positive.

To find the two non-zero eigenvalues e_\pm , and the associated orthonormal eigenstates, $|e_\pm\rangle$, of $\hat{\rho}$, we write $|e_\pm\rangle$ in terms of the nonorthogonal states $|\tilde{K}_\pm\rangle$ as

$$|e_\pm\rangle = \alpha_\pm|\tilde{K}_+\rangle + \beta_\pm|\tilde{K}_-\rangle. \quad (6.2)$$

Since $\hat{\rho}|e_\pm\rangle = e_\pm|e_\pm\rangle$, from (6.1) and (6.2) we have

$$p_+(\alpha_\pm + \beta_\pm\Delta)|\tilde{K}_+\rangle + p_-(\alpha_\pm\Delta + \beta_\pm)|\tilde{K}_-\rangle = e_\pm\alpha_\pm|\tilde{K}_+\rangle + e_\pm\beta_\pm|\tilde{K}_-\rangle, \quad (6.3)$$

$$p_+(\alpha_\pm + \beta_\pm\Delta) = e_\pm\alpha_\pm, \quad p_-(\alpha_\pm\Delta + \beta_\pm) = e_\pm\beta_\pm. \quad (6.4)$$

We look for the eigenvalues e_\pm such that

$$\begin{vmatrix} p_+ - e_\pm & p_+\Delta \\ p_-\Delta & p_- - e_\pm \end{vmatrix} = 0. \quad (6.5)$$

Expanding the determinant and solving for e_\pm we find

$$e_\pm = \frac{1}{2}(1 \pm \delta e), \quad \delta e = \sqrt{1 - 4p_+p_-(1 - \Delta^2)}. \quad (6.6)$$

From the orthonormality relations of the eigenvectors, $\langle e_\pm|e_\pm\rangle = 1$ and $\langle e_\pm|e_\mp\rangle = 0$, we have

$$\alpha_\pm^2 + \beta_\pm^2 + 2\alpha_\pm\beta_\pm\Delta = 1, \quad (6.7)$$

$$\alpha_-\alpha_+ + \beta_-\beta_+ + (\alpha_-\beta_+ + \alpha_+\beta_-)\Delta = 0. \quad (6.8)$$

The coefficients α_{\pm} and β_{\pm} have complicated forms but can be found with (6.4), (6.6) and (6.7).

The 6×6 QFI matrix for estimating the three Cartesian components of the normalized pair-separation and pair-geometrical-centroid position vectors defined in the previous chapter has the general form:

$$\begin{aligned} H_{\mu\nu}^{(ab)} &= \sum_{i=\pm} \frac{1}{e_i} \partial_{\mu}^{(a)} e_i \partial_{\nu}^{(b)} e_i \\ &+ 4\text{Re} \sum_{i=\pm} \frac{1}{e_i} (\partial_{\mu}^{(a)} \langle e_i |) (\hat{\rho} - e_i \hat{I})^2 \partial_{\nu}^{(b)} |e_i\rangle \\ &+ 4\delta e^2 \text{Re} \sum_{i \neq j} \left(\frac{1}{e_i} - e_i \right) \langle e_i | \partial_{\mu}^{(a)} |e_j\rangle \langle e_j | \partial_{\nu}^{(b)} |e_i\rangle, \end{aligned} \quad (6.9)$$

which is simply the formula (5.9) for the equal brightness problem with Δ^2 replaced by δe^2 , since $(e_+ - e_-)^2 = \delta e^2$ here. Noting that the relations (5.12) and (5.13) still hold for $\partial_{\mu} \langle e_{\pm} | (\hat{\rho} - e_{\pm} \hat{I})^2 \partial_{\nu} |e_{\pm}\rangle$ in (6.9) and from relation (6.6) that $\sum_{i=\pm} \partial_{\mu} e_i \partial_{\nu} e_i / e_i = \partial_{\mu}(\delta e) \partial_{\nu}(\delta e) / (1 - \delta e^2)$, yield the following expression for the QFI matrix element

$$\begin{aligned} H_{\mu\nu}^{(ab)} &= \frac{\partial_{\mu}^{(a)}(\delta e) \partial_{\nu}^{(b)}(\delta e)}{1 - \delta e^2} + 4(1 - \delta e^2) \text{Re}(\langle e_+ | \partial_{\mu}^{(a)} |e_- \rangle \langle e_- | \partial_{\nu}^{(b)} |e_+ \rangle) \\ &+ 4e_+ \text{Re}(\langle e_+ | \partial_{\mu}^{(a)} |e_+ \rangle \langle e_+ | \partial_{\nu}^{(b)} |e_+ \rangle) + 4e_- \text{Re}(\langle e_- | \partial_{\mu}^{(a)} |e_- \rangle \langle e_- | \partial_{\nu}^{(b)} |e_- \rangle) \\ &+ 4e_+ \text{Re}[(\partial_{\mu}^{(a)} \langle e_+ |) \partial_{\nu}^{(b)} |e_+ \rangle] + 4e_- \text{Re}[(\partial_{\mu}^{(a)} \langle e_- |) \partial_{\nu}^{(b)} |e_- \rangle], \end{aligned} \quad (6.10)$$

in which the relation $\langle e_- | \partial_{\mu}^{(l)} |e_+ \rangle = -\langle e_+ | \partial_{\mu}^{(l)} |e_- \rangle^*$ was used.

We first consider the first diagonal block $\mathbf{H}^{(l)}$ of the full QFI matrix. Taking the partial derivative of $|e_{\pm}\rangle$, given by expression (6.2), w.r.t. any component of $\boldsymbol{\ell}$, we have

$$\partial_{\mu}^{(l)} |e_{\pm}\rangle = \partial_{\mu}^{(l)} \alpha_{\pm} |\tilde{K}_+\rangle + \partial_{\mu}^{(l)} \beta_{\pm} |\tilde{K}_-\rangle + \alpha_{\pm} \partial_{\mu}^{(l)} |\tilde{K}_+\rangle + \beta_{\pm} \partial_{\mu}^{(l)} |\tilde{K}_-\rangle. \quad (6.11)$$

Taking the inner product of the expression (6.11) with the bra $\langle e_{\pm} |$ generates

$$\langle e_{\pm} | \partial_{\mu}^{(l)} |e_{\pm}\rangle = (\alpha_{\pm}^2 - \beta_{\pm}^2) \langle \tilde{K}_+ | \partial_{\mu}^{(l)} | \tilde{K}_+ \rangle, \quad (6.12)$$

which is purely imaginary. To arrive at Eq. (6.12), we also used Eq. (6.7) and the relation,

$$\langle \tilde{K}_+ | \partial_\mu^{(l)} | \tilde{K}_+ \rangle = -\langle \tilde{K}_- | \partial_\mu^{(l)} | \tilde{K}_- \rangle. \quad (6.13)$$

Taking the inner product of $\partial_\mu^{(l)} | e_+ \rangle$ with the bra $\langle e_- |$, we have

$$\begin{aligned} \langle e_- | \partial_\mu^{(l)} | e_+ \rangle &= \alpha_- \partial_\mu^{(l)} \alpha_+ + \beta_- \partial_\mu^{(l)} \beta_+ + \alpha_- \partial_\mu^{(l)} \beta_+ \Delta + \beta_- \partial_\mu^{(l)} \alpha_+ \Delta \\ &\quad + \frac{1}{2} (\alpha_- \beta_+ + \alpha_+ \beta_-) \partial_\mu^{(l)} \Delta + (\alpha_+ \alpha_- - \beta_+ \beta_-) \langle \tilde{K}_+ | \partial_\mu^{(l)} | \tilde{K}_+ \rangle, \end{aligned} \quad (6.14)$$

in which we used the relation

$$\langle \tilde{K}_\pm | \partial_\mu^{(l)} | \tilde{K}_\mp \rangle = \frac{1}{2} \partial_\mu^{(l)} \Delta. \quad (6.15)$$

Multiplying Eq. (6.11) by its adjoint, with μ in the former replaced by ν , then taking the real part, and noting the relations (6.13) and (6.15), we obtain the following expression:

$$\begin{aligned} \text{Re}[(\partial_\mu^{(l)} \langle e_\pm |) (\partial_\nu^{(l)} | e_\pm \rangle)] &= \frac{1}{2} [\partial_\mu^{(l)} (\alpha_\pm \beta_\pm) \partial_\nu^{(l)} \Delta + \partial_\mu^{(l)} \Delta \partial_\nu^{(l)} (\alpha_\pm \beta_\pm)] \\ &\quad + \partial_\mu^{(l)} \alpha_\pm \partial_\nu^{(l)} \alpha_\pm + \partial_\mu^{(l)} \beta_\pm \partial_\nu^{(l)} \beta_\pm \\ &\quad + (\partial_\mu^{(l)} \alpha_\pm \partial_\nu^{(l)} \beta_\pm + \partial_\mu^{(l)} \beta_\pm \partial_\nu^{(l)} \alpha_\pm) \Delta \\ &\quad + (\alpha_\pm^2 + \beta_\pm^2) (\partial_\mu^{(l)} \langle \tilde{K}_+ |) \partial_\nu^{(l)} | \tilde{K}_+ \rangle \\ &\quad + 2\alpha_\pm \beta_\pm \text{Re}[(\partial_\mu^{(l)} \langle \tilde{K}_+ |) \partial_\nu^{(l)} | \tilde{K}_- \rangle], \end{aligned} \quad (6.16)$$

in which we used the relations that $(\partial_\mu^{(l)} \langle \tilde{K}_+ |) \partial_\nu^{(l)} | \tilde{K}_+ \rangle = (\partial_\mu^{(l)} \langle \tilde{K}_- |) \partial_\nu^{(l)} | \tilde{K}_- \rangle$, which is already real, and $(\partial_\mu^{(l)} \langle \tilde{K}_+ |) \partial_\nu^{(l)} | \tilde{K}_- \rangle = (\partial_\mu^{(l)} \langle \tilde{K}_- |) \partial_\nu^{(l)} | \tilde{K}_+ \rangle^*$. With expressions (6.12), (6.14) and (6.16) we can numerically evaluate the first diagonal block $\mathbf{H}^{(ll)}$.

The other blocks of the QFI matrix should be less cumbersome to calculate, since Δ does not depend on \mathbf{s} . We are currently in the process of calculating these other blocks in order to complete the evaluation of the full 6×6 QFI matrix for the estimation of the 3D separation and centroid coordinates of an unbalanced source pair.

6.2 Conclusions and Future Directions

In the first part of this dissertation we have advanced two different approaches to perform joint polarimetry and 3D localization of point dipole emitters, one that utilizes the high NA of a high-resolution microscope whose imaging aperture is outfitted with a generalized spiral phase structure, and the other that utilizes the process of SAM-OAM conversion in conjunction with the spiral phase structure. Unlike more conventional polarimetric imagers [3, 4], neither of these two approaches to rotating-PSF-based polarimetric imaging requires specialized sensing elements to sense both the 3D locations and emitted polarization states of point sources.

In the second part of this dissertation we have treated the fundamental error in estimating the full 3D separation and centroid location vectors for an incoherent pair of equally bright point sources by calculating the corresponding QCRB and proposing specific projection bases for which the separation QCRB is attainable. Simulations using the Zernike basis confirm our theoretical assertions. The achievability of such quantum error bounds on estimating the separation of closely spaced point sources in all three dimensions bodes well for the optical super-resolution of point sources at dramatically reduced power levels than possible with the more conventional image-based techniques.

The generalization of the second part of this dissertation to a more realistic scenario that the two incoherent point sources have unequal intensities is currently underway. In future work, we plan to extend our current study of 3D super-resolution and super-localization with QCRB and wavefront projections to multi-color and extended sources.

References

- [1] J. Rehacek, Z. Hradil, B. Stoklasa, M. Paur, J. Grover, A. Krzic, and L. L. Sanchez-Soto, “Multiparameter quantum metrology of incoherent point sources: Towards realistic superresolution,” *Phys. Rev. A* **96**, 062107 (2017).
- [2] J. Rehacek, Z. Hradil, D. Koutny, J. Grover, A. Krzic, and L. L. Sanchez-Soto, “Optimal measurements for quantum spatial superresolution,” *Phys. Rev. A* **98**, 012013 (2018).
- [3] V. Gruev, R. Perkins, and T. York, “CCD polarization imaging sensor with aluminum nanowire optical filters,” *Opt. Express* **18**, 19087-19094 (2010).
- [4] K. Sasagawa, S. Shishido, K. Ando, H. Matsuoka, T. Noda, T. Tokuda, K. Kakiuchi, and J. Ohta, “Image sensor pixel with on-chip high extinction ratio polarizer based on 65-nm standard CMOS technology aluminum nanowire optical filters,” *Opt. Express* **21**, 11132-11140 (2013).

Appendix A

Vector Diffraction Formula for Large Apertures and Propagation Distances

We may express the monochromatic field in the image plane in terms of its angular spectrum of plane waves,

$$\vec{E}(\vec{r}) = \int \vec{a}(\vec{s}_\perp) \exp[ik(\vec{s}_\perp \cdot \vec{\rho} + s_z z)] d^2 s_\perp, \quad (\text{A.1})$$

where $\hat{s} = (\vec{s}_\perp, s_z)$ is the unit vector along the propagation vector of the corresponding plane wave. By assuming $s_\perp \leq 1$, we ignore any evanescent waves, as they are attenuated over distances comparable to the wavelength and thus do not affect the field far away from the aperture boundaries. Further, we only include plane waves propagating in the forward half solid angle, *i.e.*, $s_z = +(1 - s_\perp^2)^{1/2}$. The angular spectrum vector, $\vec{a}(\vec{s}_\perp)$, will be taken to be oriented transverse to the propagation vector, $\vec{a}(\vec{s}_\perp) \cdot \hat{s} = 0$.

The field in the plane of the diffracting aperture, here the exit pupil located, say, at $z = 0$, is given by setting $z = 0$ in (A.1). The resulting relation is a two-

Appendix A. Vector Diffraction Formula for Large Apertures and Propagation Distances ■

dimensional Fourier transform, which may be inverted to yield the angular spectrum as

$$\vec{a}(\vec{s}_\perp) = \left(\frac{k}{2\pi}\right)^2 \int d^2\rho' \vec{E}(\vec{\rho}', 0) \exp(-ik\vec{s}_\perp \cdot \vec{\rho}'), \quad (\text{A.2})$$

where $\vec{\rho}'$ is just the 2D position vector in the plane of the aperture. Substituting this relation into (A.1) gives the vector field at the downstream plane a distance z away from the aperture. By interchanging the order of the $\vec{\rho}'$ and \vec{s}_\perp integrations in the result allows us to express the electric field at plane z in terms of that in the plane of the aperture as

$$\vec{E}(\vec{r}) = \left(\frac{k}{2\pi}\right)^2 \int d^2\rho' \vec{E}(\vec{\rho}', 0) G(\vec{\rho} - \vec{\rho}', z), \quad (\text{A.3})$$

where the propagator G is given by the double integral

$$G(X, Y, z) = \int \int ds_x ds_y \exp \left[-ik(s_x X + s_y Y - \sqrt{1 - s_x^2 - s_y^2} z) \right], \quad (\text{A.4})$$

where the 2D integral is written out explicitly over the Cartesian components of \vec{s}_\perp and extended to the full (s_x, s_y) plane from the interior of the unit disk, $s_x^2 + s_y^2 \leq 1$, the latter corresponding to propagating plane waves. In the limit of large apertures and propagation distances, as we noted earlier, this extension to include evanescent waves does not entail much error, as can be shown by a stationary-phase approximation to the integral (A.4), performed originally by Wolf [1].

With the extension of the integral (A.4) over the full s_x, s_y plane, it may be evaluated exactly by means of Weyl's angular-spectrum representation of the diverging spherical wave, namely [2]

$$\frac{\exp(ikr)}{r} = \frac{ik}{2\pi} \int \int ds_x ds_y \frac{\exp[-ik(s_x X + s_y Y - \sqrt{1 - s_x^2 - s_y^2} |z|)]}{\sqrt{1 - s_x^2 - s_y^2}}, \quad (\text{A.5})$$

in which the square root is to be interpreted as being positive imaginary outside the unit disk in the s_x, s_y plane and r is defined as $(X^2 + Y^2 + z^2)^{1/2}$. A partial derivative

of this identity w.r.t. z , for $z > 0$, evaluates the propagator (A.4) as

$$G(X, Y, z) = -\frac{2\pi}{k^2} \frac{\partial}{\partial z} \frac{\exp\left(ik\sqrt{X^2 + Y^2 + z^2}\right)}{\sqrt{X^2 + Y^2 + z^2}}. \quad (\text{A.6})$$

Under conditions of large propagation distance, $k\sqrt{X^2 + Y^2 + z^2} \gg 1$, which we assume here, the derivative on the RHS is well approximated by the formula

$$G(X, Y, z) = -\frac{2i\pi}{k} \frac{\exp\left[ik\sqrt{X^2 + Y^2 + z^2}\right]}{\sqrt{X^2 + Y^2 + z^2}} \cos\theta', \quad (\text{A.7})$$

where θ' is the angle the ray from the aperture point $\vec{\rho}'$ to the observation point \vec{r} makes with the z axis, as given by

$$\cos\theta' = z/\sqrt{X^2 + Y^2 + z^2}.$$

Substitution of this result in (A.3), followed by a simple relabeling of the integration variable over the exit-pupil plane, yields the needed diffraction formula for observation points \vec{r}_I in the image plane,

$$\vec{E}(\vec{r}_I) = \frac{k}{2i\pi} \int d^2\rho \vec{E}(\vec{\rho}, 0) \frac{\exp(ik|\vec{r}_I - \vec{r}|)}{|\vec{r}_I - \vec{r}|} \cos\theta', \quad (\text{A.8})$$

where $\vec{r} = (\vec{\rho}, 0)$ is the position vector in the aperture plane and the obliquity factor, $\cos\theta'$, is equal to $z_I/|\vec{r}_I - \vec{r}|$.

The specific obliquity factor, $\cos\theta'$, present in the diffraction formula (A.4), also occurs in the Rayleigh-Sommerfeld formulation of the Fresnel-Kirchhoff scalar-diffraction theory based on the Dirichlet boundary condition for a planar aperture [3]. This formulation thus seems to extend more rigorously [4] than other scalar diffraction formulas to the vector diffraction theory, at least in the limit of large apertures and long propagation distances for which the diffraction formula (A.8) is accurate. It is also worth noting that the approximate expression (A.7) for the propagator may also be derived, as shown by Wolf, by means of a stationary-phase approximation of the integral (A.4).

The work in this Appendix was published in Ref. [5].

References

- [1] E. Wolf, “Electromagnetic diffraction in optical systems I. An integral representation of the image field,” *Proc. Royal Soc. London A* **253**, 349-357 (1959).
- [2] L. Mandel and E. Wolf, *Optical Coherence and Quantum Optics* (Cambridge, 1995), Sec. 3.2.4.
- [3] J. Goodman, *Introduction to Fourier Optics*, 3rd edition (Roberts, 2005), Chap. 3.
- [4] G. Sherman, “Application of the convolution theorem to Rayleigh’s integral formulas,” *J. Opt. Soc. Am.* **57**, 546-547 (1967).
- [5] Z. Yu and S. Prasad, “High-numerical-aperture microscopy with a rotating point spread function,” *J. Opt. Soc. Am. A* **33**, B58-B69 (2016).

Appendix B

Flux Conservation

Substituting Eq. (2.24) for $\Phi(\vec{r}, \vec{r}_I)$ into (2.22) yields the following explicit form of the image-plane electric field in terms of the source dipole moment:

$$\vec{E}_I(\vec{r}_I) = C\sqrt{z_O z_I} \int d^2\rho P(\rho) \frac{\exp[i\Omega + ik\hat{k}_I \cdot (\vec{r}_I - \vec{r}_{I0})]}{(r|\vec{r}_I - \vec{r}|)^{3/2}} \times \mathbf{JM}_L \mathbf{M}_{Op}, \quad (\text{B.1})$$

where Ω is the sum of the engineered and source-location-dependent phases in the pupil, namely

$$\Omega(\vec{r}) = \Psi(u, \phi) - kn_O \hat{r} \cdot \vec{r}_0, \quad (\text{B.2})$$

use was also made of the relations, $\cos \theta = z_O/r$ and $\cos \theta' = z_I/|\vec{r}_I - \vec{r}|$. The complex constant C is given by

$$C = \frac{k^3 n_O^{5/2}}{8i\pi^2 \epsilon_0} \exp[ik(n_O z_O + z_I)].$$

Since for each image-space ray the associated magnetic field vector is related, by Faraday's law, to the corresponding electric field vector in the radiation zone as

$$\vec{H}(\vec{r}_I) = \frac{k}{\mu_0 \omega} \hat{k}_I \times \vec{E}(\vec{r}_I), \quad (\text{B.3})$$

Appendix B. Flux Conservation

where \hat{k}_I is given by Eq. (2.25), we may write for the total magnetic field vector the integral

$$\vec{H}_I(\vec{r}_I) = \frac{Ck\sqrt{z_O z_I}}{\mu_0\omega} \int d^2\rho' P(\rho') \frac{\exp[i\Omega' + ik\hat{k}'_I \cdot (\vec{r}_I - \vec{r}_{I0})]}{(r'|\vec{r}_I - \vec{r}'|)^{3/2}} \times (\hat{k}'_I \times \mathbf{J}\mathbf{M}'_L \mathbf{M}'_O \underline{p}), \quad (\text{B.4})$$

where the use of the prime superscript on the various quantities is a short-hand notation for their dependence on the primed pupil coordinates over which the integral is to be performed.

The projection of the Poynting vector along the optical axis, when integrated over the image plane, yields the total optical flux, W_I , incident on the image plane,

$$W_I = \frac{1}{2} \text{Re} \int (\vec{E}_I \times \vec{H}_I^*) \cdot \hat{z} d^2r_I. \quad (\text{B.5})$$

Substituting (B.1) and the complex conjugate of (B.4) into this equation and integrating over the image plane yields, among other quantities, the 2D δ -function

$$\int d^2r_I \exp[ik(\hat{k}_I - \hat{k}'_I) \cdot (\vec{r}_I - \vec{r}_{I0})] = \left(\frac{2\pi}{k}\right)^2 \delta^{(2)}(\vec{k}_{I\perp} - \vec{k}'_{I\perp}), \quad (\text{B.6})$$

where $\vec{k}_{I\perp}$ and $\vec{k}'_{I\perp}$ are the projections of the unit vectors \hat{k}_I and \hat{k}'_I on the 2D image plane,

$$\vec{k}_{I\perp} = -\frac{\vec{\rho}}{\sqrt{\rho^2 + z_I^2}}, \quad \vec{k}'_{I\perp} = -\frac{\vec{\rho}'}{\sqrt{\rho'^2 + z_I^2}}. \quad (\text{B.7})$$

Noting that the equality of these two vectors imposed by the δ function in (B.6) requires $\vec{\rho} = \vec{\rho}'$, we may also express the δ function as

$$\delta^{(2)}(\vec{k}_{I\perp} - \vec{k}'_{I\perp}) = \frac{\delta^{(2)}(\vec{\rho} - \vec{\rho}')}{|\mathbf{J}|}, \quad (\text{B.8})$$

where $|\mathbf{K}|$ is the determinant of the Jacobian matrix for the 2D transformation between $\vec{k}_{I\perp}$ and $\vec{\rho}$ in the pupil plane, namely

$$|\mathbf{K}| = \det \begin{pmatrix} \frac{\partial}{\partial x} \frac{x}{\sqrt{x^2 + y^2 + z_I^2}} & \frac{\partial}{\partial y} \frac{x}{\sqrt{x^2 + y^2 + z_I^2}} \\ \frac{\partial}{\partial x} \frac{y}{\sqrt{x^2 + y^2 + z_I^2}} & \frac{\partial}{\partial y} \frac{y}{\sqrt{x^2 + y^2 + z_I^2}} \end{pmatrix}. \quad (\text{B.9})$$

Appendix B. Flux Conservation

The elements of this matrix are easily evaluated, with the diagonal elements being equal to

$$\frac{y^2 + z_I^2}{(x^2 + y^2 + z_I^2)^{3/2}}, \quad \frac{x^2 + z_I^2}{(x^2 + y^2 + z_I^2)^{3/2}}, \quad (\text{B.10})$$

and both the off-diagonal elements being equal to

$$\frac{-xy}{(x^2 + y^2 + z_I^2)^{3/2}}. \quad (\text{B.11})$$

The determinant $|\mathbf{K}|$ is thus easily verified to be $z_I^2/|\vec{r}_I - \vec{r}'|^4$, so from (B.8) it follows that

$$\delta^{(2)}(\vec{k}_{I\perp} - \vec{k}'_{I\perp}) = \frac{|\vec{r}_I - \vec{r}'|^4}{z_I^2} \delta^{(2)}(\vec{\rho} - \vec{\rho}') \quad (\text{B.12})$$

The presence of the δ -function (B.12) allows us to perform one of the two pupil-plane integrations, say that over the primed vector $\vec{\rho}'$, in the expression obtained on the RHS of (B.5) after the image-plane integration that produced the δ -function. Such integration replaces all primed variables by their unprimed counterparts, and the following expression for W_I may be obtained after such tedious but straightforward algebra:

$$W_I = |C|^2 \frac{2\pi^2 z_O}{\mu_0 \omega k z_I} \int [(\mathbf{J}\mathbf{M}_L \mathbf{M}_O \underline{p}) \times (\hat{k}_I \times \mathbf{J}^* \mathbf{M}_L^* \mathbf{M}_O^* \underline{p}^*)] \cdot \hat{z} \times \frac{|\vec{r}_I - \vec{r}'|}{r^3} d^2 \rho \quad (\text{B.13})$$

Since \hat{k}_I is orthogonal to the ray polarization vector, $\hat{k}_I \cdot \mathbf{M}_L \mathbf{M}_O \underline{p}$, and since $\hat{k}_I \cdot \hat{z} = \cos \theta_I = z_I/|\vec{r}_I - \vec{r}'|$, the following simpler expression is obtained for W_I :

$$W_I = |C|^2 \frac{2\pi^2 z_O}{\mu_0 \omega k} \int d^2 \rho \frac{(\mathbf{J}\mathbf{M}_L \mathbf{M}_O \underline{p}) \cdot (\mathbf{J}^* \mathbf{M}_L^* \mathbf{M}_O^* \underline{p}^*)}{r^3}, \quad (\text{B.14})$$

which, by recognizing that the scalar product of a column vector, \underline{u} , and its complex conjugate is the row-column matrix product, $\underline{u}^\dagger \underline{u}$, simplifies to the form

$$W_I = |C|^2 \frac{2\pi^2 z_O}{\mu_0 \omega k} \int d^2 \rho \frac{\underline{p}^\dagger \mathbf{M}_O^\dagger \mathbf{M}_L^\dagger \mathbf{J}^\dagger \mathbf{J} \mathbf{M}_L \mathbf{M}_O \underline{p}}{r^3}, \quad (\text{B.15})$$

Appendix B. Flux Conservation

This expression can be reduced further by noting the hermiticity and idempotence of the polarization matrix, \mathbf{J} , and from (2.12) and (2.14) that $\mathbf{M}_L\mathbf{M}_O = \mathbf{M}_L$, as \hat{r} is orthogonal to $\hat{\phi}$ and $\hat{\theta}$,

$$W_I = |C|^2 \frac{2\pi^2 z_O}{\mu_0 \omega k} \int d^2\rho \frac{p^\dagger \mathbf{M}_L^\dagger \mathbf{J} \mathbf{M}_L p}{r^3}. \quad (\text{B.16})$$

When the beam polarization is not analyzed, \mathbf{J} is simply the identity matrix, in which case the product, $\mathbf{M}_L^\dagger \mathbf{M}_L$, simplifies, since $\hat{\phi}$ and $\hat{\theta}$ are mutually orthogonal and have unit magnitude. From (2.14) thus

$$\begin{aligned} \mathbf{M}_L^\dagger \mathbf{M}_L &= \underline{\hat{\phi}} \underline{\hat{\phi}}^T + |\hat{\phi} \times \hat{k}_I|^2 \underline{\hat{\theta}} \underline{\hat{\theta}}^T \\ &= \underline{\hat{\phi}} \underline{\hat{\phi}}^T + \underline{\hat{\theta}} \underline{\hat{\theta}}^T \\ &= \mathbf{I} - \underline{\hat{r}} \underline{\hat{r}}^T, \end{aligned} \quad (\text{B.17})$$

where the fact that $\hat{\phi} \times \hat{k}_I = \hat{\pi}_I$ has unit magnitude was used to arrive at the second equality and the completeness of the three orthonormal basis vectors of the spherical coordinate system to arrive at the last equality. In view of these simplifications, the optical flux incident on the image plane, given by (B.15), reduces to

$$W_I = |C|^2 \frac{2\pi^2}{\mu_0 \omega k} \int d^2\rho \frac{|\vec{p}|^2 - |\vec{p} \cdot \hat{r}|^2}{r^2} \cos \theta, \quad (\text{B.18})$$

which is exactly the optical flux, W_O , incident on the pupil.

The work in this Appendix was published in Ref. [1].

References

- [1] Z. Yu and S. Prasad, “High-numerical-aperture microscopy with a rotating point spread function,” *J. Opt. Soc. Am. A* **33**, B58-B69 (2016).

Appendix C

Detailed Expression for $\hat{z} \times \vec{E}_I(\vec{r}_I)$

We now evaluate the product $\mathbf{J}\mathbf{M}_L(\vec{r})\mathbf{M}_O(\hat{r})\underline{p}$ by substituting the definitions (2.12), (2.14), and (2.17) into it. Since \hat{x} and \hat{y} , being the angular basis vectors, $\hat{\theta}$ and $\hat{\phi}$, of the spherical coordinate system are both orthogonal to its radial basis vector, \hat{r} , it follows that

$$\mathbf{M}_L(\vec{r})\mathbf{M}_O(\hat{r}) = \mathbf{M}_L(\vec{r}) \quad (\text{C.1})$$

and

$$\begin{aligned} \hat{x}^T \hat{\theta} &= -\sin \phi; \\ \hat{y}^T \hat{\theta} &= \cos \phi; \\ \hat{x}^T \hat{\phi}' &= \cos \phi [\sin \theta \sin(\theta + \theta') + \cos \theta \cos(\theta + \theta')] \\ &= \cos \phi \cos \theta'; \text{ and} \\ \hat{y}^T \hat{\phi}' &= \sin \phi [\sin \theta \sin(\theta + \theta') + \cos \theta \cos(\theta + \theta')] \\ &= \sin \phi \cos \theta', \end{aligned} \quad (\text{C.2})$$

in which relation (2.15) was employed to express $\hat{\phi}'$ in terms of the spherical basis vectors to arrive at the last two equalities. In view of relations (C.1) and (C.2), we

Appendix C. Detailed Expression for $\hat{z} \times \vec{E}_I(\vec{r}_I)$

may thus write $\mathbf{JM}_L(\vec{r})\mathbf{M}_O(\hat{r})\underline{p}$ more explicitly as

$$\mathbf{JM}_L(\vec{r})\mathbf{M}_O(\hat{r})\underline{p} = [-\alpha \sin \phi \underline{\hat{x}} \underline{\hat{\phi}}^T + \beta \cos \phi \underline{\hat{y}} \underline{\hat{\phi}}^T + \alpha \cos \phi \cos \theta' \underline{\hat{x}} \underline{\hat{\theta}}^T + \beta \sin \phi \cos \theta' \underline{\hat{y}} \underline{\hat{\theta}}^T] \underline{p}. \quad (\text{C.3})$$

Using the relation between the Cartesian and spherical basis vectors, we may express the scalar products involving $\underline{p} = (p_x, p_y, p_z)^T$ on the RHS of (C.3) as

$$\begin{aligned} \underline{\hat{\phi}}^T \underline{p} &= -p_x \sin \phi + p_y \cos \phi \text{ and} \\ \underline{\hat{\theta}}^T \underline{p} &= \cos \theta (p_x \cos \phi + p_y \sin \phi) - p_z \sin \theta. \end{aligned} \quad (\text{C.4})$$

It then follows from (C.3) that

$$\begin{aligned} \mathbf{JM}_L(\vec{r})\mathbf{M}_O(\hat{r})\underline{p} &= \alpha \{ \sin \phi (-p_x \sin \phi + p_y \cos \phi) + \cos \phi \cos \theta' \\ &\quad \times [\cos \theta (p_x \cos \phi + p_y \sin \phi) - p_z \sin \theta] \} \hat{x} \\ &+ \beta \{ \cos \phi (-p_x \sin \phi + p_y \cos \phi) + \sin \phi \cos \theta' \\ &\quad \times [\cos \theta (p_x \cos \phi + p_y \sin \phi) - p_z \sin \theta] \} \hat{y}, \end{aligned} \quad (\text{C.5})$$

where the underbars from the Cartesian basis vectors are omitted. Since we assume that the image-side NA is vanishingly small, we may set $\cos \theta'$ equal to 1 in (C.5). Then using the identities, $2 \sin \phi \cos \phi = \sin 2\phi$, $2 \sin^2 \phi = 1 - \cos 2\phi$, and $2 \cos^2 \phi = 1 + \cos 2\phi$ for (C.5), taking the cross product of (C.5) with \hat{z} , and regrouping terms, we arrive at expression (2.30) for $\hat{z} \times \vec{E}_I$, with the explicit form (2.31) for the vector field $\vec{F}(\theta, \phi)$.

The work in this Appendix was published in Ref. [1].

References

- [1] Z. Yu and S. Prasad, “High-numerical-aperture microscopy with a rotating point spread function,” *J. Opt. Soc. Am. A* **33**, B58-B69 (2016).

Appendix D

Derivation of QFI

The Cramér-Rao inequality

$$\text{Var}(\hat{\theta}) \geq \frac{1}{MF(\theta)}, \quad (\text{D.1})$$

provides a lower bound on the variance of an unbiased estimator of the parameter θ . In Eq. (D.1) M is the number of measurements and $F(\theta)$ is the classical Fisher Information (CFI) given by

$$F(\theta) = \int dx p(x|\theta) \left[\frac{\partial \ln p(x|\theta)}{\partial \theta} \right]^2 = \int dx \frac{1}{p(x|\theta)} \left[\frac{\partial p(x|\theta)}{\partial \theta} \right]^2, \quad (\text{D.2})$$

where $p(x|\theta)$ denotes the conditional probability of obtaining the value x when the parameter has the value θ .

According to the Born rule in quantum mechanics, we have $p(x|\theta) = \text{Tr} [\hat{O}_x \hat{\rho}_\theta]$, where $\{\hat{O}_x\}$ are the elements of a positive operator-value measure (POVM), and $\hat{\rho}_\theta$ is the density operator parametrized by the parameter we want to estimate. Let us introduce the Symmetric Logarithmic Derivative (SLD) \hat{L}_θ as the Hermitian operator ($\hat{L}_\theta^\dagger = \hat{L}_\theta$) implicitly defined by the relation

$$\frac{\partial \hat{\rho}_\theta}{\partial \theta} = \frac{1}{2} (\hat{L}_\theta \hat{\rho}_\theta + \hat{\rho}_\theta \hat{L}_\theta). \quad (\text{D.3})$$

Appendix D. Derivation of QFI

Note that

$$\begin{aligned}
\partial_\theta p(x|\theta) &= \partial_\theta \text{Tr} \{ \hat{O}_x \hat{\rho}_\theta \} = \text{Tr} [\hat{O}_x \partial_\theta \hat{\rho}_\theta] \\
&= \text{Tr} \left\{ \hat{O}_x \left(\frac{\hat{L}_\theta \hat{\rho}_\theta + \hat{\rho}_\theta \hat{L}_\theta}{2} \right) \right\} \\
&= \frac{1}{2} \text{Tr} \{ \hat{O}_x \hat{L}_\theta \hat{\rho}_\theta \} + \frac{1}{2} \text{Tr} \{ \hat{O}_x \hat{\rho}_\theta \hat{L}_\theta \} \\
&= \frac{1}{2} \text{Tr} \{ \hat{O}_x \hat{L}_\theta \hat{\rho}_\theta \} + \frac{1}{2} \text{Tr} \{ (\hat{O}_x \hat{\rho}_\theta \hat{L}_\theta)^\dagger \}^* \\
&= \frac{1}{2} \text{Tr} \{ \hat{O}_x \hat{L}_\theta \hat{\rho}_\theta \} + \frac{1}{2} \text{Tr} \{ \hat{L}_\theta \hat{\rho}_\theta \hat{O}_x \}^*.
\end{aligned} \tag{D.4}$$

By using the cyclic property of the trace, we have

$$\partial_\theta p(x|\theta) = \text{Re}(\text{Tr} \{ \hat{\rho}_\theta \hat{O}_x \hat{L}_\theta \}). \tag{D.5}$$

The classical Fisher information can then be written as

$$F(\theta) = \int dx \frac{\text{Re}(\text{Tr} \{ \hat{\rho}_\theta \hat{O}_x \hat{L}_\theta \})^2}{\text{Tr} \{ \hat{\rho}_\theta \hat{O}_x \}} \tag{D.6}$$

For a given quantum measurement, i.e. a POVM $\{ \hat{O}_x \}$, Eqs. (D.2) and (D.6) establish the classical bound on precision, which may be achieved by a proper processing.

In order to evaluate the ultimate bounds to precision we have to maximize the Fisher information over the quantum measurements. Following Refs. [1,2,3] we have

$$\begin{aligned}
F(\theta) &= \int dx \frac{\text{Re}(\text{Tr} \{ \hat{\rho}_\theta \hat{O}_x \hat{L}_\theta \})^2}{\text{Tr} \{ \hat{\rho}_\theta \hat{O}_x \}} \\
&\leq \int dx \frac{|\text{Tr} \{ \hat{\rho}_\theta \hat{O}_x \hat{L}_\theta \}|^2}{\text{Tr} \{ \hat{\rho}_\theta \hat{O}_x \}} \\
&= \int dx \frac{|\text{Tr} \{ (\sqrt{\hat{\rho}_\theta} \sqrt{\hat{O}_x}) (\sqrt{\hat{O}_x} \hat{L}_\theta \sqrt{\hat{\rho}_\theta}) \}|^2}{\text{Tr} \{ \hat{\rho}_\theta \hat{O}_x \}}.
\end{aligned} \tag{D.7}$$

By using the Schwartz inequality,

$$|\text{Tr} (A^\dagger B)|^2 \leq \text{Tr} (A^\dagger A) \text{Tr} (B^\dagger B), \tag{D.8}$$

Appendix D. Derivation of QFI

we have

$$\begin{aligned}
|\text{Tr} \{(\sqrt{\hat{O}_x} \sqrt{\hat{\rho}_\theta})^\dagger (\sqrt{\hat{O}_x} \hat{L}_\theta \sqrt{\hat{\rho}_\theta})\}|^2 &\leq \text{Tr} \{(\sqrt{\hat{O}_x} \sqrt{\hat{\rho}_\theta})^\dagger (\sqrt{\hat{O}_x} \sqrt{\hat{\rho}_\theta})\} \\
&\times \text{Tr} \{(\sqrt{\hat{O}_x} \hat{L}_\theta \sqrt{\hat{\rho}_\theta})^\dagger (\sqrt{\hat{O}_x} \hat{L}_\theta \sqrt{\hat{\rho}_\theta})\} \\
&= \text{Tr} \{\hat{\rho}_\theta \hat{O}_x\} \text{Tr} \{\hat{L}_\theta \hat{O}_x \hat{L}_\theta \hat{\rho}_\theta\}. \tag{D.9}
\end{aligned}$$

By using Eq. (D.9) in Eq. (D.7), we have

$$F(\theta) \leq \int dx \text{Tr} \{\hat{L}_\theta \hat{O}_x \hat{L}_\theta \hat{\rho}_\theta\} = \text{Tr} \left\{ \left(\int dx \hat{O}_x \right) \hat{L}_\theta \hat{\rho}_\theta \hat{L}_\theta \right\}. \tag{D.10}$$

Since $\int dx \hat{O}_x = \hat{I}$, where \hat{I} is the identity operator, we have

$$F(\theta) \leq \text{Tr} \{\hat{\rho}_\theta \hat{L}_\theta^2\}. \tag{D.11}$$

We see that the CFI of any quantum measurement is ultimately bounded by the so-called quantum Fisher information (QFI) $H(\theta)$,

$$F(\theta) \leq H(\theta) \equiv \text{Tr} \{\hat{\rho}_\theta \hat{L}_\theta^2\}. \tag{D.12}$$

For multi-parameter problem, the density operator ρ_θ depends on a set of parameters $\theta = \{\theta_\mu\}$, $\mu = 1, \dots, N$, the relevant object in the estimation problem is given by the QFI matrix, whose elements are defined as

$$H_{\mu\nu} \stackrel{\text{def}}{=} \text{Tr} \left(\hat{\rho} \frac{\hat{L}_\mu \hat{L}_\nu + \hat{L}_\nu \hat{L}_\mu}{2} \right) = \text{ReTr} (\hat{\rho} \hat{L}_\mu \hat{L}_\nu). \tag{D.13}$$

References

- [1] C. Helstrom, *Quantum Detection and Estimation Theory* (Academic Press, 1976), vol. 123.
- [2] S. Braunstein and C. Caves, “Statistical distance and the geometry of quantum states,” *Phys. Rev. Lett.* **72**, 3439-3443 (1994).
- [3] M. Paris, “Quantum estimation for quantum technology,” *Int. J. Quant. Inform.* **7**, 125-137 (2009).

Appendix E

Some Properties of Sine and Cosine States

E.0.1 Orthonormality and Completeness

These states were defined as

$$\begin{aligned} CC_{mn}(\mathbf{u}) &= \sqrt{\frac{c_m c_n}{\pi}} \cos(2\pi m u^2) \cos n\phi, & m, n = 0, 1, \dots; \\ CS_{mn}(\mathbf{u}) &= \sqrt{\frac{c_m c_n}{\pi}} \cos(2\pi m u^2) \sin n\phi, & m = 0, 1, \dots, n = 1, 2, \dots; \\ SC_{mn}(\mathbf{u}) &= \sqrt{\frac{c_m c_n}{\pi}} \sin(2\pi m u^2) \cos n\phi, & m = 1, 2, \dots, n = 0, 1, \dots; \\ SS_{mn}(\mathbf{u}) &= \sqrt{\frac{c_m c_n}{\pi}} \sin(2\pi m u^2) \sin n\phi, & m, n = 1, 2, \dots; \end{aligned} \tag{E.1}$$

in which the normalization constant, c_n , has the value, $c_n = 2 - \delta_{n0}$. Denoting the most general of these basis functions simply as $A_{mn}(\mathbf{u}) = \langle \mathbf{u} | A_{mn} \rangle$, we can, by standard trigonometric integrations, easily prove their orthonormality over the unit disk,

$$\int_0^1 du u \int_0^{2\pi} d\phi A_{mn}^*(\mathbf{u}) A_{m'n'}(\mathbf{u}) = \delta_{mm'} \delta_{nn'}. \tag{E.2}$$

Appendix E. Some Properties of Sine and Cosine States

Their completeness,

$$\sum_{m,n=0}^{\infty} \sum_{\substack{A=CC, \\ CS,SC,SS}} A_{mn}^*(\mathbf{u}) A_{mn}(\mathbf{w}) = \delta^{(2)}(\mathbf{u} - \mathbf{w}), \quad (\text{E.3})$$

follows from the Poisson summation formulas involving sums over non-negative integer values of m, n ,

$$\sum_m c_m \cos 2\pi m(v - w) = \delta(v - w); \quad \sum_n c_n \cos n(\phi - \psi) = 2\pi\delta(\phi - \psi); \quad (\text{E.4})$$

valid over the unit disk, $0 \leq v, w \leq 1$; $0 \leq \phi, \psi < 2\pi$.

E.0.2 The Overlap Integrals $\langle A_{mn}|K_{\pm}\rangle$, $A = \text{CC}, \text{CS}, \text{SC}, \text{SS}$

The overlap integrals, $\langle A_{mn}|K_{\pm}\rangle$, for a transversely separated source pair, $\mathbf{l}_{\perp} \neq 0$, $l_z = 0$, are given by

$$\langle A_{mn}|K_{\pm}\rangle = \frac{1}{\sqrt{\pi}} \int_0^1 du u \oint d\phi \exp(\mp i 2\pi \mathbf{u} \cdot \mathbf{l}_{\perp}) A_{mn}(\mathbf{u}). \quad (\text{E.5})$$

Since $\mathbf{u} \cdot \mathbf{l}_{\perp} = u l_{\perp} \cos(\phi - \phi_l)$, in which ϕ_l is the polar angle of \mathbf{l}_{\perp} , the following integral identities are easily proved using the Bessel-function generating function formula:

$$\begin{aligned} \oint d\phi \exp[\mp iz \cos(\phi - \phi_l)] \cos n\phi &= (\mp i)^n 2\pi \cos n\phi_l J_n(z), \\ \oint d\phi \exp[\mp iz \cos(\phi - \phi_l)] \sin n\phi &= (\mp i)^n 2\pi \sin n\phi_l J_n(z), \end{aligned} \quad (\text{E.6})$$

in which $J_n(z)$ denotes the ordinary Bessel function of order n . Use of these identities allows us to perform the ϕ integral in Eq. (E.5). We thus reduce all of the probabilities

Appendix E. *Some Properties of Sine and Cosine States*

to simple integrals over a single convenient radial variable, $v = u^2$,

$$\begin{aligned}
 \langle \text{CC}_{mn} | K_{\pm} \rangle &= (\mp i)^n \sqrt{c_m c_n} \cos n\phi_l \int_0^1 dv \cos(2\pi m v) J_n(2\pi l_{\perp} \sqrt{v}); \\
 \langle \text{CS}_{mn} | K_{\pm} \rangle &= (\mp i)^n \sqrt{c_m c_n} \sin n\phi_l \int_0^1 dv \cos(2\pi m v) J_n(2\pi l_{\perp} \sqrt{v}); \\
 \langle \text{SC}_{mn} | K_{\pm} \rangle &= (\mp i)^n \sqrt{c_m c_n} \cos n\phi_l \int_0^1 dv \sin(2\pi m v) J_n(2\pi l_{\perp} \sqrt{v}); \\
 \langle \text{SS}_{mn} | K_{\pm} \rangle &= (\mp i)^n \sqrt{c_m c_n} \sin n\phi_l \int_0^1 dv \sin(2\pi m v) J_n(2\pi l_{\perp} \sqrt{v}); \tag{E.7}
 \end{aligned}$$

which are all real integrals whose phases are either 0 or $\pi \pmod{2\pi}$, which are constants independent of \mathbf{l}_{\perp} , and whose magnitudes satisfy the relation, $|\langle A_{mn} | K_{+} \rangle| = |\langle A_{mn} | K_{-} \rangle|$, $A = \text{CC}, \text{CS}, \text{SC}, \text{SS}$. Because of these two properties, this complete basis achieves QFI for a transversely separated source pair.

The work in this Appendix was published in Ref. [1].

References

- [1] Z. Yu and S. Prasad, “Quantum Limited Superresolution of an Incoherent Source Pair in Three Dimensions,” *Phys. Rev. Lett.* **121**, 180504 (2018).

Appendix F

Likelihood Function for Photon Division into N Channels

Let us consider the problem of dividing M photons into N channels, with P_k being the probability of a photon going into the k th channel. If n_k is the number of photons transmitted into the k th channel in a statistical realization of this process, then the probability of this process is given by the multinomial (MN) distribution,

$$\text{Prob}(\{n_k\}|M) = M! \prod_{k=1}^N \frac{P_k^{n_k}}{n_k!}, \quad (\text{F.1})$$

in which all photon numbers, n_1, \dots, n_N and \bar{n} are non-negative and thus each bounded above by M . Let η be the quantum efficiency (QE) of detection of the transmitted photons in each channel, then the probability of detection of m_k photons in the k th channel, $k = 1, \dots, N$, conditioned on the knowledge that $\{n_k, k = 1, \dots, N\}$ photons were transmitted into the various channels, is given by a product of binomial distributions,

$$\text{Prob}(\{m_k\}|\{n_k\}, M) = \prod_{k=1}^N \frac{n_k!}{m_k!(n_k - m_k)!} \eta^{m_k} (1 - \eta)^{n_k - m_k}. \quad (\text{F.2})$$

Appendix F. Likelihood Function for Photon Division into N Channels

The probability of jointly detecting m_k photons in the k th channel, with $k = 1, 2, \dots, N$, is then given by the composition rule,

$$\begin{aligned}
 \text{Prob}(\{m_k\}|M) &= \sum_{\substack{\{n_k \in (m_k, \dots, M)\} \\ \sum_k n_k = M}} \text{Prob}(\{m_k\}|\{n_k\}, M) \text{Prob}(\{n_k\}|M) \\
 &= M! \sum_{\substack{\{n_k \in (m_k, \dots, M)\} \\ \sum_k n_k = M}} \prod_{k=1}^N \left[\frac{P_k^{n_k} (1-\eta)^{n_k} \eta^{m_k} (1-\eta)^{-m_k}}{(n_k - m_k)! m_k!} \right] \\
 &= M! \left[\prod_{k=1}^N \frac{(\eta P_k)^{m_k}}{m_k!} \right] \prod_{\substack{k=1 \\ \sum_k \delta_k = M - \sum_k m_k}}^N \left[\sum_{\delta_k=0}^{M-m_k} \frac{[P_k (1-\eta)]^{\delta_k}}{\delta_k!} \right],
 \end{aligned} \tag{F.3}$$

in which the transformation, $\delta_k = n_k - m_k$, was used to replace the sum over n_k to that over δ_k . The latter product of the sums, with the restriction that the sum of the values of the indices δ_k be constrained to be a fixed number, can be performed by using the following identity involving the product of exponentials:

$$\begin{aligned}
 \exp \left[(1-\eta) \sum_{k=1}^N P_k \right] &= \prod_{k=1}^N \exp[(1-\eta) P_k] \\
 &= \prod_{k=1}^N \sum_{\delta_k=0}^{\infty} \frac{[P_k (1-\eta)]^{\delta_k}}{\delta_k!},
 \end{aligned} \tag{F.4}$$

and noting that its left-hand side may be expanded in powers of $(1-\eta)$. Comparing the $(1-\eta)^\delta$ term on both sides of the resulting identity then yields the needed relation,

$$\begin{aligned}
 \prod_{\substack{k=1 \\ \sum_k \delta_k = \delta}}^N \left[\sum_{\delta_k=0}^{M-m_k} \frac{[P_k (1-\eta)]^{\delta_k}}{\delta_k!} \right] &= \frac{[\sum_{k=1}^N P_k (1-\eta)^\delta]}{\delta!} \\
 &= \frac{(1-\eta)^\delta}{\delta!},
 \end{aligned} \tag{F.5}$$

since the probabilities P_k sum to 1 over all N channels. When relation (F.5), with δ replaced by $M - \sum_k m_k$, is substituted into expression (F.3), we can simplify the

Appendix F. Likelihood Function for Photon Division into N Channels

latter to the form,

$$\text{Prob}(\{m_k\}|M) = M! \frac{(1 - \eta)^{M - \sum_k m_k}}{(M - \sum_k m_k)!} \left[\prod_{k=1}^N \frac{(\eta P_k)^{m_k}}{m_k!} \right], \quad (\text{F.6})$$

which has a very compelling interpretation that non-unit QE provides yet another channel, the $(N + 1)$ th channel, which ‘‘captures’’ the undetected counts, while the other channels capture photons at the compounded probabilities, ηP_k , per photon for the k th channel, with $k = 1, \dots, M$.

Note that for a given set of detected counts, $\{m_1, \dots, m_N\}$, the probability (F.6) reduces to a product of a fixed η dependent factor and another that depends on the per-photon channel probabilities P_k , $k = 1, \dots, N$. This implies that the maximum-likelihood estimation of the latter probabilities from the likelihood function (F.6) is independent of η . For this reason, there is no loss of generality in choosing $\eta = 1$.

We must also interpret the N modes in expression (F.6) as including the 4 Zernikes modes into which the wavefront is projected as well as the remaining modes into which the wavefront is not projected, with the latter to be regarded as a single undetected mode, which we denote by an overhead bar. In other words, for $\eta = 1$, one must modify that expression to the form,

$$\text{Prob}(\{m_k\}|M) = M! \frac{\bar{P}^{\bar{m}}}{\bar{m}!} \left[\prod_{k=1}^N \frac{(\eta P_k)^{m_k}}{m_k!} \right], \quad (\text{F.7})$$

with $\bar{P} = 1 - \sum_{k=1}^N P_k$ and $\bar{m} = M - \sum_{k=1}^N m_k$.

The work in this Appendix was published in Ref. [1].

References

- [1] Z. Yu and S. Prasad, “Quantum Limited Superresolution of an Incoherent Source Pair in Three Dimensions,” *Phys. Rev. Lett.* **121**, 180504 (2018).

Appendix G

Photon wavefunction in the pupil plane

Consider a thin-lens imager of aperture radius R for which the reference source plane is the xy coordinate plane, and the pupil and image planes are, respectively, distances z_O and $z_O + z_I$ away from that coordinate plane. Then under paraxial optical propagation in the Fresnel-diffraction approximation, the complex amplitude of the imaging wavefront is given by the following integral over the pupil plane:

$$\begin{aligned} \langle \mathbf{r}_I | K_{\pm} \rangle = & \int d^2\rho \tilde{P}(\boldsymbol{\rho}) \exp \left[-i \frac{2\pi}{\lambda} \boldsymbol{\rho} \cdot \left(\frac{\mathbf{r}_I}{z_I} \right. \right. \\ & \left. \left. + \frac{\mathbf{r}_O \pm \delta \mathbf{r}_O}{z_O + \zeta_O \pm \delta \zeta_O} \right) + i \frac{\pi}{\lambda} \left(\frac{1}{z_O + \zeta_O \pm \delta \zeta_O} - \frac{1}{z_O} \right) \rho^2 \right], \end{aligned} \quad (\text{G.1})$$

where $(\mathbf{r}_O \pm \delta \mathbf{r}_O, \zeta_O \pm \delta \zeta_O)$, $(\boldsymbol{\rho}, z_O)$, and $(\mathbf{r}_I, z_O + z_I)$ label the point-source, pupil-plane, and image-plane position vectors, respectively. The pupil function, $\tilde{P}(\boldsymbol{\rho})$, is restricted only by the normalization condition,

$$\int d^2\rho |\tilde{P}(\boldsymbol{\rho})|^2 = 1, \quad (\text{G.2})$$

Appendix G. Photon wavefunction in the pupil plane

and a complex quadratic phase factor dependent on object and image coordinates alone has been suppressed on the RHS of Eq. (G.1).

If we assume that the axial source coordinates, $\zeta_O \pm \delta\zeta_O$, are small in magnitude compared to the pupil and image plane distances, z_O and z_I , and their 2D position vectors, $\mathbf{r}_O \pm \delta\mathbf{r}_O$, are also comparably small in magnitude, conditions that surely hold for high-numerical-aperture microscopy, then correct to the linear order in these small quantities we may express Eq. (G.1) as

$$\langle \mathbf{r}_I | K_{\pm} \rangle = \int d^2u P(\mathbf{u}) \exp[-i2\pi \mathbf{s}_{\perp} \cdot \mathbf{u} - i\pi s_z u^2 \mp i\Psi(\boldsymbol{\ell}, \mathbf{u}) - i2\pi \mathbf{u} \cdot \mathbf{v}], \quad (\text{G.3})$$

in which we have used normalized source, pupil, and image plane coordinates defined as

$$\begin{aligned} \mathbf{u} &= \frac{\boldsymbol{\rho}}{R}, \quad \mathbf{v} = \frac{\mathbf{r}_I}{\lambda z_I/R}, \quad (\mathbf{s}_{\perp}, \mathbf{l}_{\perp}) = \frac{(\mathbf{r}_O, \delta\mathbf{r}_O)}{\lambda z_O/R}, \\ (s_z, l_z) &= \frac{(\zeta_O, \delta\zeta_O)}{\lambda z_O^2/R^2} \end{aligned} \quad (\text{G.4})$$

in which $M = -z_I/z_O$ is the image magnification, and the pupil phase function, $\Psi(\boldsymbol{\ell}, \mathbf{u})$, which depends only on the pair-separation and pupil coordinates, has the form,

$$\Psi(\boldsymbol{\ell}, \mathbf{u}) = 2\pi \mathbf{u} \cdot \mathbf{l}_{\perp} + \pi u^2 l_z. \quad (\text{G.5})$$

The pupil function in normalized coordinates is defined by the relation, $P(\mathbf{u}) = R^2 \tilde{P}(\boldsymbol{\rho})$.

Since $\exp(-i2\pi \mathbf{u} \cdot \mathbf{v})$ is the complex Fourier exponential connecting the pupil and image planes, we may regard the rest of the integrand as the pupil-plane wavefunction of a single imaging photon emitted by the incoherent point source at position $(\mathbf{r}_O \pm \delta\mathbf{r}_O, \zeta_O \pm \delta\zeta_O)$ and transmitted through the imager. In other words, apart from an

Appendix G. Photon wavefunction in the pupil plane

arbitrary overall phase factor, we may write

$$\langle \mathbf{u} | K_{\pm} \rangle = P(\mathbf{u}) \exp[-i2\pi \mathbf{s}_{\perp} \cdot \mathbf{u} - i\pi s_z u^2 \mp i\Psi(\boldsymbol{\ell}, \mathbf{u})]. \quad (\text{G.6})$$

The work in this Appendix was published in Ref. [1].

References

- [1] S. Prasad and Z. Yu, “Quantum-limited superlocalization and superresolution of a source pair in three dimensions,” *Phys. Rev. A* **99**, 022116 (2019).

Appendix H

CFI for Multinomial Distribution

For $(N + 1)$ projection channels, with per-photon probabilities being P_1, \dots, P_{N+1} , in which $P_{N+1} \stackrel{\text{def}}{=} \bar{P} = 1 - \sum_{n=1}^N P_n$, the probability, $P(m_1, \dots, m_{N+1})$, of detecting m_1, \dots, m_{N+1} photons in those channels when a total of M photons are incident on the projection system is given by the multinomial distribution (MND),

$$P(m_1, \dots, m_{N+1}) = M! \prod_{n=1}^{N+1} \frac{P_n^{m_n}}{m_n!} \Theta(m_1, \dots, m_{N+1}), \quad (\text{H.1})$$

with Θ denoting the indicator function for the discrete space of constraints defined as

$$\sum_{n=1}^{N+1} m_n = M, \quad m_1, \dots, m_n = 0, 1, \dots, M. \quad (\text{H.2})$$

The channel probabilities, P_1, \dots, P_N , depend on the parameters being estimated.

Taking the logarithm of expression (H.1) and the partial derivatives of the resulting expression with respect to the μ th and ν th parameters successively, then multiplying the resulting expressions with each other, and finally taking the expectation of their product over MND yields the following form for the $\mu\nu$ matrix element

Appendix H. CFI for Multinomial Distribution

of the associated CFI:

$$\begin{aligned}
J_{\mu\nu} &= \sum_{n=1}^{N+1} \sum_{l=1}^{N+1} \langle m_n m_l \rangle (\partial_\mu \ln P_n) (\partial_\nu \ln P_l) \\
&= M(M-1) \sum_{n=1}^{N+1} \sum_{l=1}^{N+1} P_n P_l (\partial_\mu \ln P_n) (\partial_\nu \ln P_l) + M \sum_{n=1}^{N+1} P_n (\partial_\mu \ln P_n) (\partial_\nu \ln P_n) \\
&= M(M-1) \left[\sum_{n=1}^{N+1} P_n (\partial_\mu \ln P_n) \right] \left[\sum_{l=1}^{N+1} P_l (\partial_\nu \ln P_l) \right] \\
&\quad + M \sum_{n=1}^{N+1} P_n (\partial_\mu \ln P_n) (\partial_\nu \ln P_n) \\
&= M \sum_{n=1}^{N+1} \frac{(\partial_\mu P_n) (\partial_\nu P_n)}{P_n}, \tag{H.3}
\end{aligned}$$

in which we used the well known formula for the second moment of MND,

$$\langle m_n m_l \rangle = M(M-1)P_n P_l + M P_n \delta_{nl}, \tag{H.4}$$

to reach the second line and the fact that since $\sum_{n=1}^{N+1} P_n = 1$, any partial derivative of it vanishes,

$$\sum_{n=1}^{N+1} P_n (\partial_\mu \ln P_n) = 0, \tag{H.5}$$

to arrive at the final expression.

The work in this Appendix was published in Ref. [1].

References

- [1] S. Prasad and Z. Yu, “Quantum-limited superlocalization and superresolution of a source pair in three dimensions,” *Phys. Rev. A* **99**, 022116 (2019).